

Resonant Enhancement of Light Induced Superconductivity in K_3C_{60}

Dissertation

zur Erlangung des Doktorgrades an der Fakultät für Mathematik,
Informatik und Naturwissenschaften

Fachbereich Physik
der Universität Hamburg

Vorgelegt von
Edward Rowe

Hamburg
2024

Gutachter/innen der Dissertation:

Prof. Dr. Andrea Cavalleri
Prof. Dr. Henning Moritz
Prof. Dr. Edoardo Baldini

Zusammensetzung der Prüfungskommission:

Prof. Dr. Andrea Cavalleri
Prof. Dr. Henning Moritz
Prof. Dr. Ludwig Mathey PD
Dr. Guido Meier
Prof. Dr. Nils Huse

Vorsitzende/r der Prüfungskommission:

Prof. Dr. Ludwig Mathey

Datum der Disputation:

27.09.2024

Vorsitzender des Fach-Promotionsausschusses PHYSIK:

Prof. Dr. Markus Drescher

Leiter des Fachbereichs PHYSIK:

Prof. Dr. Wolfgang J. Parak

Dekan der Fakultät MIN:

Prof. Dr.-Ing. Norbert Ritter

Eidesstattliche Versicherung / Declaration on oath

Hiermit versichere ich an Eides statt, die vorliegende Dissertationsschrift selbst verfasst und keine anderen als die angegebenen Hilfsmittel und Quellen benutzt zu haben.

Sofern im Zuge der Erstellung der vorliegenden Dissertationsschrift generative Künstliche Intelligenz (gKI) basierte elektronische Hilfsmittel verwendet wurden, versichere ich, dass meine eigene Leistung im Vordergrund stand und dass eine vollständige Dokumentation aller verwendeten Hilfsmittel gemäß der Guten wissenschaftlichen Praxis vorliegt. Ich trage die Verantwortung für eventuell durch die gKI generierte fehlerhafte oder verzerrte Inhalte, fehlerhafte Referenzen, Verstöße gegen das Datenschutz- und Urheberrecht oder Plagiate.

Hamburg, den 04-03-2024



Unterschrift der Doktorandin / des Doktoranden

Abstract

Materials which exhibit the most exotic and potentially useful phenomena, such as magnetism and high temperature superconductivity, also happen to be some of the most poorly understood. These properties arise from the manifestation of quantum mechanical effects on macroscopic length scales, and therefore provide a playground in which some of the most fundamental physics can be explored. Classes of these so-called ‘quantum materials’ host rich phase diagrams, in which external tuning parameters such as temperature, pressure and chemical doping can be used to switch between phases with different properties. The functionalization of these phenomena is currently limited by these traditional tuning parameters, which are often not reversible and can generally only be applied on very slow time scales. Furthermore, many of these properties emerge exclusively at extremely low temperatures accessible only via expensive and unwieldy liquid helium cooling, prohibiting them from daily usage outside of research laboratories.

For these reasons, physicists have begun to use intense pulses of light as an alternative approach to manipulating the properties of quantum materials, a field of research which has been enabled by dramatic advances in the neighboring field of ultrafast optics over the last few decades. Although one would naively expect the

deposition of large amounts of energy into the sample via such a pulse to melt exotic orders, the application of this technique to a rich variety of compounds has often confounded this expectation, resulting in a vast and ever-expanding library of exotic phenomena, including ferroelectricity, ferromagnetism, charge density waves and non-trivial topology.

Arguably the most striking examples of the manipulation of matter with light have come in the realm of high temperature superconductivity. Historically, light-based enhancement of superconductivity was first demonstrated in the 1960s through the illumination of tin and aluminium films with microwaves, but interest in the field was re-awakened with the discovery in 2011 that photoexcitation of the single layer non-superconducting cuprate $\text{La}_{1.675}\text{Eu}_{0.2}\text{Sr}_{0.125}\text{CuO}_4$ with an intense mid-infrared laser pulse could induce a state with superconducting-like optical properties on a few-ps timescale. A similar effect was subsequently observed in the $\text{YBa}_2\text{Cu}_3\text{O}_{6+x}$ family of compounds, in which optical signatures of superconductivity were induced transiently far above the equilibrium transition temperature, and even above room temperature for a doping level of $x = 0.45$.

Superficially similar light-induced superconductivity has also been demonstrated in iron-based superconductors, and two classes of molecular superconductors - firstly K_3C_{60} from the alkali-doped fulleride family and subsequently the charge-transfer salt $\kappa\text{-(BEDT-TTF)}_2\text{Cu}[\text{N}(\text{CN})_2]\text{Br}$. In all cases, questions remain about the microscopic processes which lead to the formation of the superconducting-like properties after photo-excitation.

The most promising candidate for the ultimate goal of stabilizing a superconducting-

like state at room temperature is arguably K_3C_{60} , which is unique amongst light-induced superconductors in that the lifetime of the photoexcited state is comparatively very long, on the order of nanoseconds. However, such a long-lived superconducting-like state has so far only been observed up to a temperature of 100 K - bringing this effect to room temperature remains a key objective.

In this thesis new results which utilize state-of-the-art optical techniques to study the effect of photoexcitation of K_3C_{60} at lower frequencies than were previously accessible are presented. These results include the discovery of a resonance near 10 THz driving frequency which enabled the first demonstration of the long-lived light-induced superconducting-like state at room temperature. The identification of a dominant energy scale for this effect should direct future theoretical investigation into light-induced superconductivity in K_3C_{60} , and the low excitation fluences combined with long lifetime potentially trace a path towards steady-state operation at room temperature in the future.

Zusammenfassung

Materialien, die die exotischsten und potenziell interessantesten Phänomene aufweisen, wie Magnetismus und Hochtemperatursupraleitung, gehören zufällig auch zu den am schlechtesten verstandenen. Diese Eigenschaften entstehen durch die Manifestation quantenmechanischer Effekte auf makroskopischen Längenskalen und bieten daher eine Spielwiese, auf der einige der grundlegendsten physikalischen Phänomene erforscht werden können. Klassen dieser so genannten “Quantenmaterialien” weisen reichhaltige Phasendiagramme auf, in denen durch externe Einstellparameter wie Temperatur, Druck und chemische Dotierung zwischen Phasen mit unterschiedlichen Eigenschaften gewechselt werden kann. Die Funktionalisierung dieser Phänomene ist derzeit durch diese traditionellen Abstimmungsparameter begrenzt, die häufig nicht reversibel sind und im Allgemeinen nur auf sehr langsamen Zeitskalen angewendet werden können. Darüber hinaus treten viele dieser Eigenschaften ausschließlich bei extrem niedrigen Temperaturen auf, die nur über eine teure und unhandliche Kühlung mit flüssigem Helium zugänglich sind, so dass sie im Alltag außerhalb von Forschungslabors nicht genutzt werden können.

Aus diesen Gründen haben Physiker begonnen, intensive Lichtimpulse als alternativen Ansatz zur Beeinflussung der Eigenschaften von Quantenmaterialien zu ver-

wenden, ein Forschungsgebiet, das durch dramatische Fortschritte im benachbarten Bereich der ultraschnellen Optik in den letzten Jahrzehnten ermöglicht wurde. Obwohl man naiverweise erwarten würde, dass die Einbringung großer Energiemengen in die Probe mittels eines solchen optischen Pulses exotische Ordnungen zum Schmelzen bringt, hat die Anwendung dieser Technik auf eine Vielzahl von Verbindungen diese Erwartung oft widerlegt, was zu einer umfangreichen und ständig wachsenden Bibliothek exotischer Phänomene geführt hat, darunter Ferroelektrizität, Ferromagnetismus, Ladungsdichtewellen und nichttriviale Topologie.

Die wohl eindrucksvollsten Beispiele für die Manipulation von Materie mit Licht stammen aus dem Bereich der Hochtemperatursupraleitung. Historisch gesehen wurde die Verstärkung der Supraleitung durch Licht erstmals in den 1960er Jahren durch die Beleuchtung von Zinn- und Aluminiumfilmen mit Mikrowellen demonstriert. Das Interesse an diesem Gebiet wurde jedoch durch die Entdeckung im Jahr 2011 wieder geweckt, dass die Lichtanregung des einschichtigen, nicht-supraleitenden Cuprats $\text{La}_{1.675}\text{Eu}_{0.2}\text{Sr}_{0.125}\text{CuO}_4$ mit einem intensiven Laserpuls im mittleren Infrarot einen Zustand mit supraleitungsähnlichen optischen Eigenschaften auf einer Zeitskala von wenigen ps herbeiführen konnte. Ein ähnlicher Effekt wurde anschließend in der $\text{YBa}_2\text{Cu}_3\text{O}_{6+x}$ -Familie von Verbindungen beobachtet, in denen optische Signaturen der Supraleitung vorübergehend weit oberhalb der Gleichgewichts-Übergangstemperatur und sogar oberhalb der Raumtemperatur für ein Dotierungsniveau von $x = 0,45$ induziert wurden.

Eine oberflächlich ähnliche lichtinduzierte Supraleitung wurde auch in eisenbasierten Supraleitern und zwei Klassen von molekularen Supraleitern nachgewiesen - zunächst K_3C_{60} aus der Familie der alkalidotierten Fulleride und anschließend das Ladungstrans-

fersalz κ -(BEDT-TTF)₂Cu[N(CN)₂]Br. In allen Fällen bleiben Fragen zu den mikroskopischen Prozessen offen, die zur Ausbildung der supraleitungsähnlichen Eigenschaften nach der Lichtanregung führen.

Der vielversprechendste Kandidat für das ultimative Ziel, einen supraleitungsähnlichen Zustand bei Raumtemperatur zu stabilisieren, ist wohl K₃C₆₀, der unter den lichtinduzierten Supraleitern insofern einzigartig ist, als die Lebensdauer des lichtangeregten Zustands vergleichsweise sehr lang ist, in der Größenordnung von Nanosekunden. Allerdings wurde ein derart langlebiger supraleiterähnlicher Zustand bisher nur bis zu einer Temperatur von etwa 100 K beobachtet - die Übertragung dieses Effekts auf Raumtemperatur bleibt ein wichtiges Ziel.

In dieser Arbeit werden neue Ergebnisse vorgestellt, die modernste optische Techniken nutzen, um den Effekt der Lichtanregung von K₃C₆₀ bei niedrigeren Frequenzen zu untersuchen, als bisher zugänglich waren. Zu diesen Ergebnissen gehört die Entdeckung einer Resonanz um 10 THz, die den ersten Nachweis des langlebigen lichtinduzierten supraleitenden Zustands bei Raumtemperatur ermöglichte. Die Identifizierung einer dominanten Energieskala für diesen Effekt sollte die künftige theoretische Untersuchung der lichtinduzierten Supraleitung in K₃C₆₀ leiten, und die niedrigen Anregungsfluenzen in Verbindung mit der langen Lebensdauer könnten einen Weg zu einem zukünftigen stationären Betrieb bei Raumtemperatur aufzeigen.

Contents

1	Introduction	1
2	Light-Based Enhancement of Superconductivity	8
2.1	Introduction to Superconductivity	9
2.1.1	BCS Theory	10
2.1.2	Ginzburg-Landau Theory	12
2.1.3	The Superconducting Transition	15
2.1.4	Optical Properties of Metals and Superconductors	16
2.2	High Temperature Superconductivity	22
2.2.1	Light Induced Superconductivity in Single-Layer Cuprates	26
2.2.2	Light Induced Superconductivity in $\text{YBa}_2\text{Cu}_3\text{O}_{6+x}$	29
2.3	Light-Based Control of Molecular Superconductivity	36
3	Superconductivity in Alkali-doped Fullerenes	41
3.1	Equilibrium Properties	42
3.2	Light Induced Metastable Superconductivity in K_3C_{60}	53
4	Resonant Enhancement of Light Induced Superconductivity in K_3C_{60}	67
4.1	High-Field Far to Mid-IR Pulse Generation	67

4.2	Preparing K_3C_{60} for Optical Measurements	77
4.3	Data Acquisition	77
4.4	Reconstructing the Optical Properties	80
4.4.1	Exponential Models	82
4.4.2	Saturating Model	84
4.5	Resonantly Enhanced Photosusceptibility	85
4.6	Theoretical Discussion	95
	Summary and Outlook	102
	List of Publications	106
	Bibliography	107

Chapter 1

Introduction

Phase transitions in solids occur when symmetry is broken upon cooling, with a disordered high temperature phase giving way to a more ordered low temperature phase. For example, as a paramagnet transitions into a ferromagnet the spins become ordered, arranging themselves such that their magnetic dipoles align. In general, the breaking of symmetry and emergence of order occurs as the system is cooled to lower temperature, with disorder being associated with higher entropy.

When light is incident on a solid, energy is deposited into the material, causing it to heat up. Ordinarily, one would expect this heating (if sufficiently strong) to melt ordered phases and increase the symmetry of the system. However, recently it has been demonstrated that under certain circumstances, in which a well-chosen material is combined with light consisting of the appropriate frequency and polarization content, the application of light can instead result in the emergence or enhancement of order.

These orders, which include for example superconductivity [1–8], charge density waves [9, 10], ferroics [11–13] and non-trivial topologies [14, 15], often have exotic and functionally-desirable properties - such as the dissipation-less transport exhibited by superconductors. The prospect of being able to control these properties on ultra-fast (meaning femtosecond to picosecond) timescales has motivated a new field of research devoted to uncovering and understanding new examples of these ‘light-induced’ non-equilibrium phenomena [16, 17].

One particularly fruitful pathway for the manipulation of crystals with light has been through both linear and nonlinear ‘phononics’. All crystals exhibit collective vibrational modes which consist of oscillations of the constituent atoms about their equilibrium positions, known as phonons. Some of these phonons (which are designated as being ‘infrared-active’) result in the emergence of an electric dipole moment when they are displaced, meaning that they are linearly coupled to electric fields and so can be driven directly by the oscillating electric field associated with a pulse of laser light. When the frequency of the light is tuned to be in resonance with the mode the effect is massively enhanced, resulting in large amplitude periodic modulations of the crystal structure. The resonance frequencies of these phonon modes are determined by the atomic masses and inter-atomic forces, and are typically within the range 1-50 THz. The lower end of this frequency range is commonly referred to as ‘far-infrared’, whereas the upper end is usually called ‘mid-infrared’.

As well as oscillating with large amplitude, the directly driven infrared-active mode can exert a force on other modes via phonon-phonon coupling in a process known as ‘ionic Raman scattering’, with the nature of the force depending on which couplings are symmetry-allowed by the crystal [18–20]. For the case of a centro-symmetric

crystal, the dynamics of two modes with only the lowest possible order of allowed coupling are described by the Hamiltonian in equation 1.1.

$$H = -z_{\text{IR}}^* Q_{\text{IR}} E + \frac{1}{2} m_{\text{IR}} \omega_{\text{IR}}^2 Q_{\text{IR}}^2 + \frac{1}{2} m_{\text{R}} \omega_{\text{R}}^2 Q_{\text{R}}^2 + V_{\text{IR,R}} Q_{\text{IR}}^2 Q_{\text{R}} \quad (1.1)$$

Here, Q_{IR} and Q_{R} are the coordinates of the two modes, which have natural frequencies ω_{IR} and ω_{R} with reduced masses m_{IR} and m_{R} , respectively. The subscript IR refers to an infrared-active mode which has a linear coupling to the electric field (E) through its born effective charge (z_{IR}^*), and the subscript R refers to a Raman-active mode which necessarily does not couple linearly to the electric field (as it carries no dipole moment when displaced). The lowest-order allowed coupling is given by the final term in equation 1.1. The coupled equations of motion can be obtained by taking the partial derivatives of the Hamiltonian with respect to each mode coordinate to obtain the force, resulting in equations 1.2a and 1.2b, where phenomenological damping terms have also been added with damping rates γ_{IR} and γ_{R} .

$$m_{\text{IR}} \frac{d^2 Q_{\text{IR}}}{dt^2} + m_{\text{IR}} \gamma_{\text{IR}} \frac{dQ_{\text{IR}}}{dt} = z_{\text{IR}}^* E - (m_{\text{IR}} \omega_{\text{IR}}^2 + 2V_{\text{IR,R}} Q_{\text{R}}) Q_{\text{IR}} \quad (1.2a)$$

$$m_{\text{R}} \frac{d^2 Q_{\text{R}}}{dt^2} + m_{\text{R}} \gamma_{\text{R}} \frac{dQ_{\text{R}}}{dt} = -m_{\text{R}} \omega_{\text{R}}^2 Q_{\text{R}} - V_{\text{IR,R}} Q_{\text{IR}}^2 \quad (1.2b)$$

Equation 1.2a shows that the electric field drives the IR mode directly, the square of which then drives the R mode according to equation 1.2b. The result of this square is that the force on the R mode consists of one component which oscillates at a frequency of approximately $2\omega_{\text{IR}}$, and a rectified uni-directional component. This uni-directional component results in a quasi-static distortion of the crystal structure, unlike the linear oscillations of the IR mode which give zero time-averaged displacement [21]. Thus, the non-linear phonon driving regime, which can be accessed using

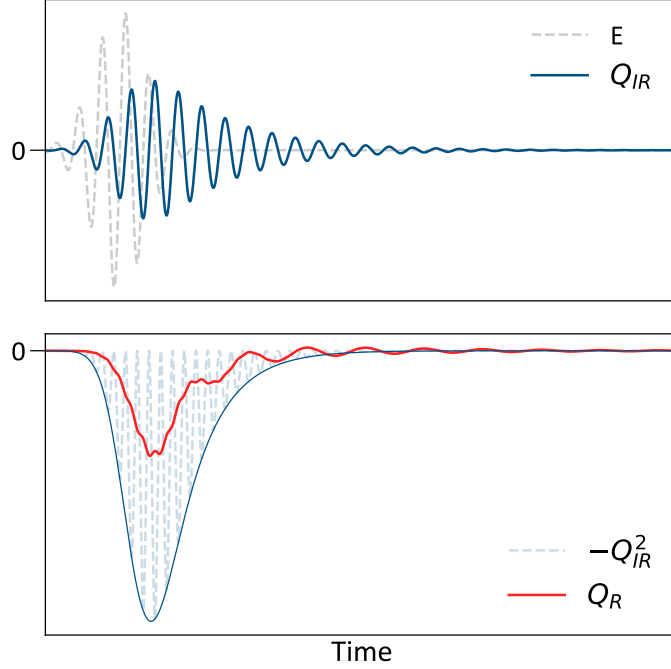


Figure 1.1: Simulation of two coupled phonons, obeying the equations of motion 1.2a and 1.2b. The infrared active mode (Q_{IR}) is driven resonantly by the electric field (E), and in turn transiently displaces the Raman mode (Q_R), resulting in a time-averaged distortion of the crystal structure.

resonant light in the mid-infrared frequency range, presents the possibility of achieving controllable non-thermal distortions of the crystal structure, a promising pathway towards the enhancement or creation of ordered phases. For this reason many of the most successful demonstrations of the control of material properties with light, including most of those discussed in this thesis, have been carried out using light in this frequency range.

A prototypical example is the case of light-induced metastable ferromagnetism in YTiO_3 [22]. The rare-earth titanate family of compounds, of which YTiO_3 is a

member, can host a variety of ordered phases, including both ferroelectricity and ferromagnetism, depending on the choice of rare earth atom and the external applied conditions (such as temperature and strain) [23].

In equilibrium, YTiO_3 becomes ferromagnetic below a Curie temperature (T_c) of 27 K, but even for the highest applied fields at the lowest temperatures the magnetization saturates at about 80% of the ideal maximum value of $1 \mu_B$ per Ti atom [24]. This is due to fluctuations relating to an anti-ferromagnetic state which is very close in energy to the ferromagnetic ground state. These fluctuations are also thought to suppress the Curie temperature, as mean-field theories (which neglect such fluctuations) predict a higher transition temperature of around 50 K [25, 26].

As the energy gap between the ferromagnetic and anti-ferromagnetic states is highly sensitive to the crystal structure, it may be possible to control the magnetic properties of YTiO_3 by fine-tuning this structure. Such fine-tuning can in principle be achieved with mid-infrared light via nonlinear phononics, presenting YTiO_3 as a promising candidate for light-based manipulation.

In the ferromagnetic state below T_c , photo-exciting at a frequency of 9 THz, resonant with a phonon which displaces the oxygen atoms relative to the yttrium and titanium, resulted in an enhancement of the magnetism. When the same photo-excitation protocol was applied with the system above T_c (in the absence of equilibrium ferromagnetism), a metastable ferromagnetic state emerged with a lifetime of several nanoseconds.

These results provide a clear demonstration of the potential of light to both en-

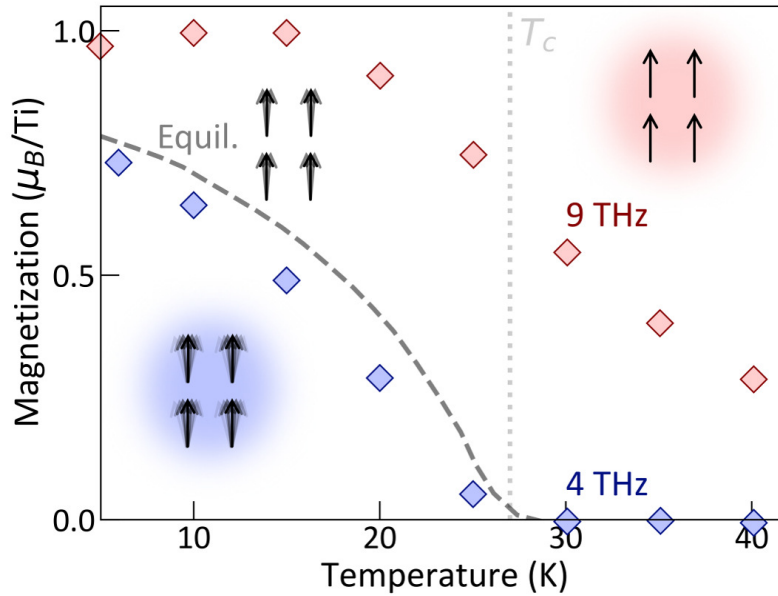


Figure 1.2: Photo-induced ferromagnetism in YTiO_3 . For 4 THz photo-excitation (blue) the magnetization is decreased at all temperatures below T_c , implying that fluctuations are enhanced. For 9 THz photo-excitation (red) the magnetization is enhanced below T_c , implying that fluctuations are instead suppressed. Above T_c magnetization is induced upon 9 THz photo-excitation. The data in this figure is taken from [22].

hance order by suppressing fluctuations, and to create order where there was none in equilibrium. However, in the same experiments the authors showed that when the light is instead tuned to a frequency of 4 THz, resonant with a phonon mode which displaces the yttrium atoms relative to the titanium and oxygen, the effect was reversed. Below T_c the magnetism was suppressed compared to its equilibrium value, and the Curie temperature itself was also lowered. This highlights the principle that order can only be enhanced when the light is resonant with an appropriate excitation, in this case the 9 THz phonon, with the microscopic details of the excitation being key to the result.

In this thesis I will discuss analogous experiments in which the same idea of light-based manipulation has been applied to superconductivity. In recent years light has been used to create exotic non-equilibrium phases with superconducting-like properties far above the equilibrium transition temperature in several superconductors. After a brief and more general introduction to superconductivity I will provide an account of some of these experiments which have been carried out in several members of the cuprate family, as well as the molecular solid κ -(BEDT-TTF)₂Cu[N(CN)₂]Br in chapter 2. Chapters 3 and 4 will then be devoted to the discussion of alkali-doped fullerenes, a third class of superconductor in which a superconducting-like state has been manifested at high temperatures using photo-excitation. Chapter 3 consists of an introduction to the equilibrium properties of the alkali-doped fullerenes, focussing on details relating to the formation of superconductivity in equilibrium, followed by a detailed review of previous experiments relating to so-called ‘photo-induced superconductivity’ in K₃C₆₀. In chapter 4 new results are presented demonstrating a resonant enhancement of this phenomenon close to 10 THz frequency, including the first observation of the photo-induced superconducting-like state on metastable timescales at room temperature. This is accompanied by an overview of recent attempts at developing a theoretical understanding of the formation of the photo-induced superconducting-like state, which should be directly informed by the existence of a dominant excitation at 10 THz.

Chapter 2

Light-Based Enhancement of Superconductivity

The unique properties of superconductors have motivated physicists and chemists in a more than century-long search for a material which is superconducting at room temperature. Alone, the promise of zero-resistance wires enabling super-efficient transport and energy storage would have extreme real-world consequences if manifested [27]. The immense magnetic fields achieved inside superconducting coils thanks to their ability to host very high currents are already seeing widespread use in MRI scanners and research laboratories. More remotely, but perhaps even more significantly, quantum computers which rely on superconducting qubits have the potential to revolutionize the future of computation [28].

Historically the search for higher temperature superconductivity has predominantly consisted of the systematic synthesis and measurement of many promising compounds, an approach which eventually led to the spectacular discovery of high-

temperature superconductivity in cuprates [29]. An alternative and until recently much less well-known approach has been to enhance superconductivity in known compounds using an external stimulus in the form of light, as was originally demonstrated through the illumination of Al films with microwaves [30–33], and much later in some cuprate high-temperature superconductors using much higher frequencies [34–37]. In the last decade, several much more spectacular examples of the enhancement of superconductivity using light have been reported in a variety of compounds.

In this chapter a brief conceptual introduction to superconductivity will be given, followed by an overview of some important recently-discovered examples of light-induced superconductivity in layered superconductors belonging to the cuprate and κ -ET families, which will provide broader context to the discussion of light-induced superconductivity in the molecular solid K_3C_{60} that forms the subject of all later chapters.

2.1 Introduction to Superconductivity

Superconductivity is defined by the presence of two properties: the ability to conduct DC electrical currents without resistance, and the expulsion of static magnetic fields (known as the Meissner effect). Many materials which exhibit metallic behaviour at room temperature undergo a transition into a superconducting state upon cooling below their respective critical temperature (T_c). Such a transition is shown in figure 2.1, where the sudden drop to zero resistance below a temperature of $T_c = 93\text{ K}$ accompanied by the emergence of strong diamagnetic susceptibility signifies the onset

of superconductivity.

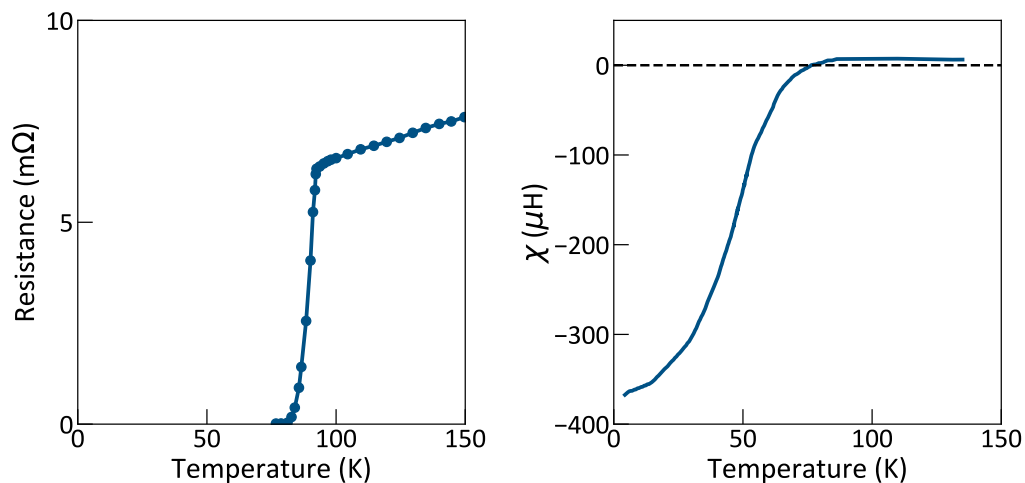


Figure 2.1: The superconducting transition in YBCO, as illustrated by (left panel) a drop to zero resistance, and (right panel) the emergence of diamagnetism signified by a drop in magnetic susceptibility (χ) upon cooling below $T_c = 93$ K. The data in this figure is taken from [38].

2.1.1 BCS Theory

The properties of conventional superconductors can be fairly well-understood in terms of a formalism known as ‘BCS theory’ [39, 40]. BCS theory offers a comprehensive microscopic explanation of the basic properties (Meissner effect and perfect conductivity) of superconductors, starting from a microscopic model of the electron-electron interactions. The basic principle is that the electrons, which always repel each other in free space (due to their mutual electronic interaction with like charges) can instead develop an effective attractive interaction when placed in a crystal en-

vironment. This results in the formation of bound electron pairs, known as ‘Cooper pairs’. In a superconductor, these Cooper pairs, with a charge of $2e$ (where e is the charge of a single electron) are the fundamental carriers of current. The binding energy of a single Cooper pair is known as the ‘energy gap’, conventionally written as 2Δ . Superconductivity arises when these Cooper pairs form a macroscopic quantum condensate.

In the BCS picture, the energy gap 2Δ is the dominant energy scale which determines T_c , as at higher temperatures the Cooper pairs break down thermally and superconductivity is lost. Quantitatively, the relation between the zero-temperature superconducting gap ($\Delta(T = 0)$) and T_c (derived under the assumption of weak coupling) is given by equation 2.1:

$$2\Delta(T = 0) = 3.528k_B T_c \quad (2.1)$$

BCS theory explains that the attractive interaction between electrons arises from coupling to the phonons of the crystal structure. A popular pseudo-classical picture for understanding this is that as one electron moves through the sample, it distorts the positively charged lattice ions towards it, leaving behind a region of more concentrated positive charge, to which the trailing electron is attracted [41]. Based on this picture, BCS theory predicts the following scaling for T_c :

$$k_B T_c = 1.13\omega_0 e^{-1/\lambda} \quad (2.2)$$

where ω_0 is a typical phonon frequency and λ represents the electron-phonon coupling strength [42]. Equation 2.2 implies that materials with stronger electron-phonon

coupling and higher phonon frequencies (corresponding to lighter atoms and stiffer inter-atomic bonds) should have higher critical temperatures. This relation leads to the existence of the so-called isotope effect, which is the scaling of T_c with the isotopic mass (M) of the constituent atoms. As the resonance frequency of a spring (with force constant k and mass m) is given by $\sqrt{k/m}$, we would expect $T_c \propto \omega_0 \propto M^{-\alpha}$, with $\alpha = 0.5$. Experimentally, the presence or absence of an isotope effect in any given superconductor, along with the value of the exponent α , provides clues towards the potential role of phonons in the electron pairing mechanism.

2.1.2 Ginzburg-Landau Theory

For some superconductors, including many of those discussed in this thesis, the quantitative prediction of equation 2.1 is violated. This implies that the microscopic details of the electron-electron interaction in these materials may differ from those described by standard BCS theory, but fortunately the overall picture of some kind of attractive electron-electron interaction resulting in the formation of pairs (with an energy gap) which condense to form a super-fluid is apparently much more universal. For this reason we turn to a thermodynamic treatment of the superconducting phase transition which is agnostic with respect to the details of the microscopic interactions, but can nevertheless capture much of the emergent physics observed in all superconductors. This treatment is known as Ginzburg-Landau theory, and actually preceded the advent of BCS theory by seven years [43].

In Ginzburg-Landau theory, the wave-function of the Cooper pair condensate is represented by a complex number (here denoted by $\psi = |\psi|e^{i\phi}$) which can be used as an order parameter to describe the normal state to superconductor transition. The

free energy density (f) is written as a function of the order parameter:

$$f = f_{n0} + \frac{h^2}{8\pi} + \alpha|\psi|^2 + \frac{\beta}{2}|\psi|^4 + \frac{1}{2m^*}|\left(\frac{\hbar}{i}\nabla - \frac{2e}{c}A\right)\psi|^2 \quad (2.3)$$

Here, f_{n0} is the free energy density of the normal state, and h is the applied magnetic field density. The electromagnetic vector potential is denoted by A and couples to the order parameter via the coefficients e , c and m^* which represent the electron charge, speed of light and effective mass respectively. This formula essentially arises from a Taylor series expansion of the free energy close to the phase transition in powers of ψ , with the assumption that the free energy should not depend on the absolute value of the phase ϕ . The final term of equation 2.3, which accounts for spatial gradients in the order parameter as well as coupling to electromagnetic fields, enters by analogy with the wave function of a charged particle in an electromagnetic field, only here we consider a particle with charge $2e$ and effective mass m^* to represent a Cooper pair from BCS theory.

For a spatially-homogeneous order parameter, in the absence of externally applied fields, equation 2.3 reduces to:

$$f = \alpha|\psi|^2 + \frac{\beta}{2}|\psi|^4 \quad (2.4)$$

The phase transition from the normal state to the superconducting state is captured by the temperature dependence of α , as illustrated in figure 2.2. For $\alpha > 0$ equation 2.4 only has one minimum which occurs at $|\psi| = 0$. For $\alpha < 0$ a ‘Mexican hat’ shaped potential forms with minima at $|\psi|^2 = -\alpha/\beta$. This means that as α crosses from positive to negative, the system (which acts to minimize the free energy) will adopt

a finite value of the order parameter, crossing from the normal to superconducting phase. To do so it must spontaneously break the global gauge symmetry by picking one value of the order parameter phase. This is analogous to how a ferro-magnet spontaneously ‘chooses’ the direction of the magnetic polarization upon cooling below the Curie temperature. Figure 2.2 also illustrates the possibility for oscillations of

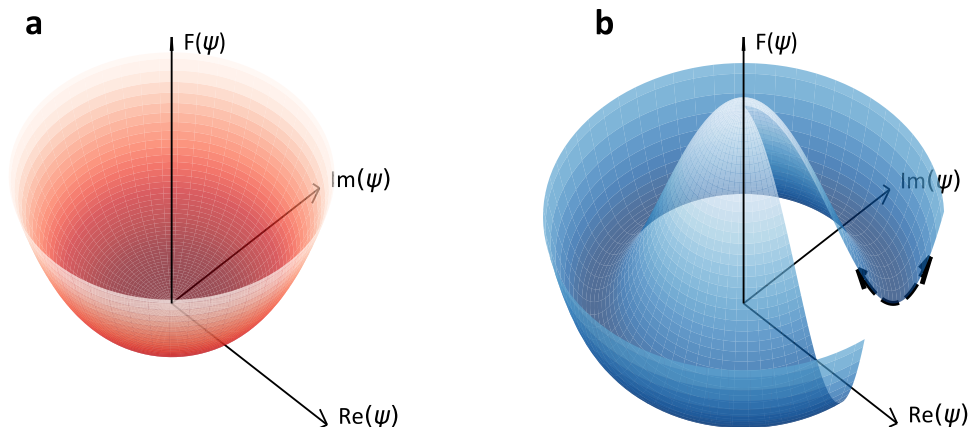


Figure 2.2: The potential energy surface of the complex order parameter ψ based on equation 2.4. **a** The normal phase with $T > T_c$, $\alpha > 0$. **b** The superconducting phase with $T < T_c$, $\alpha < 0$. The double-headed dashed black arrow in **b** represents the oscillations of the order parameter amplitude when the Higgs mode is excited.

the amplitude of the order parameter to arise. These oscillations are known as the Higgs mode, and have recently been observed in several superconductors through their influence on the non-linear optical properties, particularly in the THz frequency regime [44].

2.1.3 The Superconducting Transition

The onset of superconductivity from a normal state occurs when two distinct criteria are met: the formation of Cooper pairs, and the quantum condensation of these Cooper pairs with macroscopic phase coherence. For conventional superconductors it is safe to assume that the energy cost of macroscopic phase fluctuations is much higher than the breakdown of individual pairs such that T_c is determined by the energy gap 2Δ , as given by equation 2.1. However, for many high T_c superconductors (in particular those with a low carrier density) this hierarchy may be reversed, with a breakdown in long-range phase coherence occurring at lower temperatures than the thermal destruction of individual Cooper pairs [45].

Distinguishing between these two scenarios is important for the discussion of light-induced superconductivity which follows, as in the first case the application of light must somehow create Cooper pairs from quasi-particles, presumably by enhancing pairing interactions. However, in the second scenario Cooper pairs may be pre-existing, and in order to resurrect macroscopic superconductivity the role of light is to somehow establish long-range phase-coherence [46].

Table 2.1 (adapted from [45]) lists a selection of superconductors alongside their critical temperatures (T_c) and the ratio T_θ^{\max}/T_c . T_θ^{\max} is defined as an upper bound for T_c , calculated as the temperature above which phase ordering would disappear even if the disordering effects of all other degrees of freedom were ignored. For a conventional superconductor (where here lead is included as a representative example) T_θ^{\max}/T_c is extremely high, indicating that the phase is so stiff that fluctuations are minimal on the temperature scale of T_c and therefore cannot be playing a sig-

nificant role in the breakdown of superconductivity at T_c . On the other hand, for the other less conventional superconductors in table 2.1, T_θ^{\max}/T_c is much closer to 1, indicating that phase fluctuations are likely to be very significant close to T_c , and could be causing the superconductor to normal state transition at this temperature. This presents the possibility that incoherent Cooper pairs survive above T_c in these compounds.

Material	T_c (K)	T_θ^{\max}/T_c
Pb	7	2×10^5
$\text{La}_{2-x}\text{Sr}_x\text{CuO}_{4+\delta}$	28	1
$\text{YBa}_2\text{Cu}_3\text{O}_{7-\delta}$	92	1.4
$(\text{BEDT})_2\text{Cu}(\text{NCS})_2$	8	1.7
K_3C_{60}	19	17

Table 2.1: The superconducting critical temperature (T_c) and theoretically estimated ratio of phase decoherence temperature (T_θ^{\max}) to critical temperature, taken from [45].

2.1.4 Optical Properties of Metals and Superconductors

As the experiments central to this thesis utilize optical techniques to study the properties of superconductors, a brief overview is included here.

The response of a superconductor to light can be derived from BCS theory, resulting in the Mattis-Bardeen equations for $\sigma_1(\omega)$ and $\sigma_2(\omega)$ [47, 48]. This derivation considers both excitations involving the breaking of Cooper pairs when the frequency of the incident light is higher than 2Δ , and the contribution of thermally excited uncondensed quasiparticles which becomes non-zero at finite temperature. At zero temperature in the absence of such thermally excited quasiparticles, σ_1 is zero for all

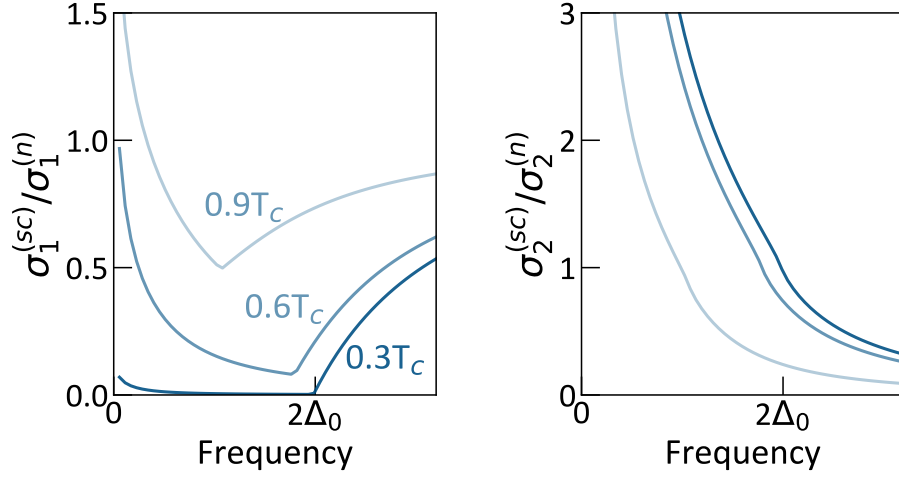


Figure 2.3: Real (σ_1) and imaginary (σ_2) parts of the optical conductivity of a superconductor in the extreme dirty limit, divided by the same quantities in the normal state just above T_c , calculated using the Mattis-Bardeen equations for three different temperatures, as indicated by the text in the figure.

frequencies below 2Δ , as no light can be absorbed at these frequencies. However, as soon as the temperature is increased the thermally excited quasiparticles will contribute a Drude-like response at low frequencies - resulting in finite dissipation even below the gap. The real and imaginary parts of the optical conductivity predicted by the Mattis-Bardeen equations for a superconductor in the extreme dirty limit (meaning that the quasi-particle scattering rate is much larger than the superconducting gap, such that the normal state conductivity can be approximated by a constant) are plotted in figure 2.3.

A much simpler treatment which captures most of the physics relevant to the experiments discussed in this thesis begins with the Drude model, which provides an intuitive understanding of the response of conduction electrons in a metal to an electric field, from which the optical conductivity can be derived. This model is based on

a classical equation of motion for the drift velocity (v) of the electrons (with effective mass m^*), which are assumed to scatter with random momenta at a rate γ :

$$m^* \frac{dv}{dt} = eE - \gamma m^* v \quad (2.5)$$

The response to an oscillating electric field can be calculated by inserting $E = E_0 e^{-i\omega t}$ and solving for v via fourier analysis. This gives the result:

$$v(\omega) = \frac{e}{m^*} \frac{E}{\gamma - i\omega} \quad (2.6)$$

The current density (J) can then be derived by inserting the relation $J = nev$ (where n is the electron number density):

$$J(\omega) = \frac{ne^2}{m^*} \frac{E}{\gamma - i\omega} \quad (2.7)$$

From this expression the complex optical conductivity (σ) can be derived, according to its definition $J = \sigma E$, resulting in:

$$\sigma(\omega) = \frac{ne^2}{m^*} \frac{1}{\gamma - i\omega} \quad (2.8)$$

In order to disentangle the in-phase and out-of-phase response of the current to the applied field we define σ_1 and σ_2 as representing the real and imaginary components, respectively, according to the equation $\sigma = \sigma_1 + i\sigma_2$. For these two quantities equation 2.8 gives:

$$\sigma_1(\omega) = \frac{ne^2}{m^* \gamma} \frac{1}{1 + \omega^2/\gamma^2} \quad (2.9a)$$

$$\sigma_2(\omega) = \frac{ne^2}{m^* \gamma} \frac{\omega/\gamma}{1 + \omega^2/\gamma^2} \quad (2.9b)$$

Calculated plots of $\sigma_1(\omega)$ and $\sigma_2(\omega)$ based on these equations are shown in figure 2.4, where the red curves result from taking $\gamma = 1$ and $ne^2/m^* = 1$. In general, the Drude model predicts a peak in σ_1 centered at zero frequency, with a width given by the scattering rate γ and a peak in σ_2 at frequency γ .

The blue curves in figure 2.4 illustrate the effect on the optical properties of independently adjusting the parameters γ and n . Both reducing the scattering rate by a factor of two (blue curves in the top row) and increasing the carrier density by a factor of two (blue curves in the bottom row) have the effect of increasing the DC (zero frequency) conductivity by a factor of two, but the two cases can be distinguished by studying the relative behaviours of σ_1 and σ_2 at finite frequencies. In the case where the carrier density is increased both σ_1 and σ_2 are enhanced for all frequencies. In contrast, reducing the scattering rate results in a spectral-weight conserving sharpening of the peak in σ_1 such that the enhancement at low frequencies is accompanied by a reduction at higher frequencies. In this case the peak in σ_2 is shifted towards lower frequency, an effect also not seen when the carrier density is increased. This simple example illustrates the principle that measuring the optical properties across a range of frequencies can give insight into changes to the microscopic sample properties such as carrier density and scattering rate.

Returning to the topic of superconductivity, the optical properties of a zero temperature superconductor (in the absence of thermally excited quasiparticles) can be recovered from the Drude model by taking the limit $\gamma \rightarrow 0$, which is to insert the assumption that there is no damping of the motion of the superconducting charge carriers. In this case, the peak in σ_1 becomes infinitely narrow but retains its integrated spectral weight (as required by charge conservation) and σ_2 becomes divergent. The

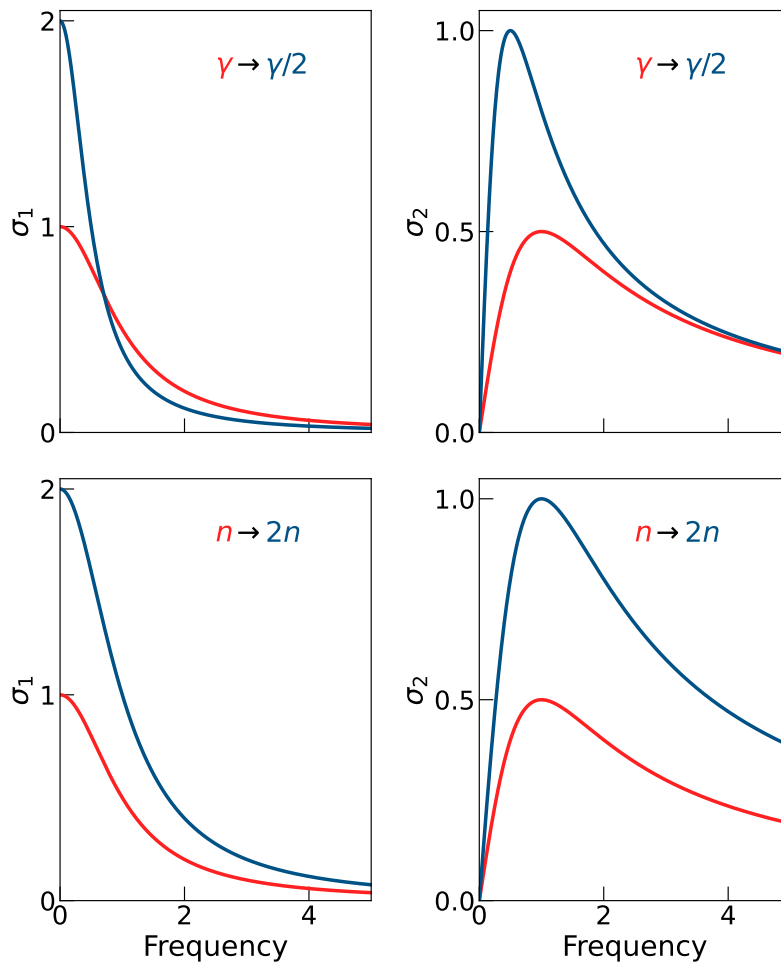


Figure 2.4: Real and imaginary parts of the optical conductivity resulting from different choices of the parameters n and γ . In red: $\gamma = 1$ and $ne^2/m^* = 1$. In blue: $\gamma = 1/2$ and $ne^2/m^* = 1$ (top row), $\gamma = 1$ and $ne^2/m^* = 2$ (bottom row).

equations 2.9a and 2.9b then become:

$$\sigma_1(\omega) = \frac{\pi n e^2}{2 m^*} \delta(\omega = 0) \quad (2.10a)$$

$$\sigma_2(\omega) = \frac{n e^2}{m^*} \frac{1}{\omega} \quad (2.10b)$$

A closer approximation to the Mattis-Bardeen model which enables the modelling of finite-temperature effects is the so-called ‘two-fluid model’, given here by equations 2.11a and 2.11b. This consists of the sum of two contributions, the first arises from a dissipation-less (superconducting) fluid with $\gamma \rightarrow 0$, and the second from another fluid with finite γ which represents the contribution of the thermally excited un-condensed quasiparticles which are present at finite temperature. The superconducting and normal carrier densities are given by n_{sc} and n_n respectively.

$$\sigma_1(\omega) = \frac{\pi n_{sc} e^2}{2 m^*} \delta(\omega = 0) + \frac{n_n e^2}{m^* \gamma} \frac{1}{1 + \omega^2/\gamma^2} \quad (2.11a)$$

$$\sigma_2(\omega) = \frac{n_{sc} e^2}{m^*} \frac{1}{\omega} + \frac{n_n e^2}{m^* \gamma} \frac{\omega/\gamma}{1 + \omega^2/\gamma^2} \quad (2.11b)$$

Comparing the first terms in equations 2.11a and 2.11b shows that the strength of the zero-frequency pole in $\sigma_1(\omega)$ (that arises from the infinite DC conductivity of the superconducting carriers), which is proportional to n_{sc} is equal to the proportionality constant of the divergent component of $\sigma_2(\omega)$. This relationship is actually more general than the two-fluid model described here, as it arises directly from Kramers-Kronig relations [49]. This means that the super-fluid density can be extracted from optical measurements (which are restricted to probing finite frequencies) by fitting the $1/\omega$ -component of $\sigma_2(\omega)$. The Kramers-Kronig argument is valid in both directions, meaning that whenever a divergence is present in $\sigma_2(\omega)$, there must be an

infinite contribution to $\sigma_1(\omega)$ at $\omega = 0$.

Plots of $\sigma_1(\omega)$ and $\sigma_2(\omega)$ calculated from equations 2.11a and 2.11b are shown in figure 2.5 for four different values of the ratio n_{sc}/n_n . As the two-fluid model does

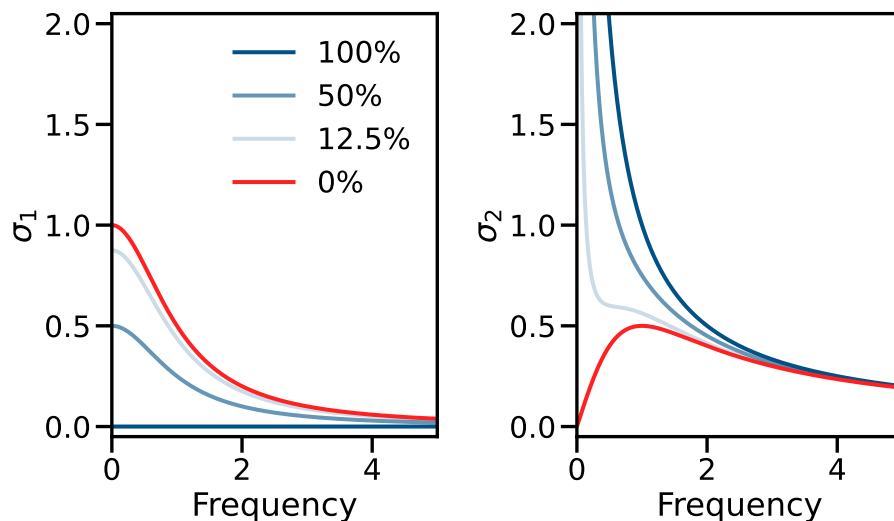


Figure 2.5: Real and imaginary parts of the optical conductivity calculated from the two-fluid model, for different ratios of n_{sc}/n_n . The axes are defined by taking $\gamma = 1$ (for the normal carriers) and $(n_{sc} + n_n)e^2/m = 1$.

not include a ‘pair-breaking’ term, it is only applicable for frequencies below 2Δ where such processes do not contribute. Nevertheless, the essential low-frequency features of the Mattis-Bardeen model, namely a loss in spectral weight in $\sigma_1(\omega)$ at finite frequencies and a $1/\omega$ -like divergent component in σ_2 , are recovered.

2.2 High Temperature Superconductivity

Until 1986 the highest superconducting critical temperature which had been observed was 23.3K in Nb_3Ge [50]. This record was suddenly and dramatically sur-

passed by the discovery of superconductivity in LBCO with a critical temperature of 35 K [29]. This was quickly followed by the discovery of superconductivity in many other so-called ‘cuprate’ compounds, up to a record temperature of 138 K in $\text{Hg}_{0.8}\text{Tl}_{0.2}\text{Ba}_2\text{Ca}_2\text{Cu}_3\text{O}_{8.33}$, which currently holds the record for the highest-known critical temperature of any material in ambient conditions [51].

Structurally, all cuprates consist of a stack of quasi-two dimensional perovskite-like copper-oxygen layers, as illustrated in figure 2.6a. Depending on the specific compound there can be different numbers of unique layers per unit cell.

As well as high temperature superconductivity, cuprate materials also exhibit many other exotic phases. In all cases the undoped parent compound is an anti-ferromagnetic insulator, which gives way to a superconducting dome upon increasing the level of hole doping. A simplified schematic phase diagram illustrating this universal behaviour is shown in figure 2.6b. As well as superconductivity and anti-ferromagnetism, different families of cuprate compounds also play host to many other even more exotic phases including charge density waves, the pseudogap regime and strange metals [52]. The energetic proximity of all these different phases makes cuprate superconductors ideal candidates for manipulation with light, as small perturbations can be expected to lead to profound changes in properties within such a rich landscape. In the sections that follow an overview will be given of experiments which have demonstrated the use of light to enhance superconductivity in several different cuprate compounds.

Due to the high degree of structural anisotropy, the electrodynamic properties of cuprate superconductors (both above and below T_c) show starkly contrasting behaviour in the in-plane and out-of-plane directions. Above T_c , cuprates are typically

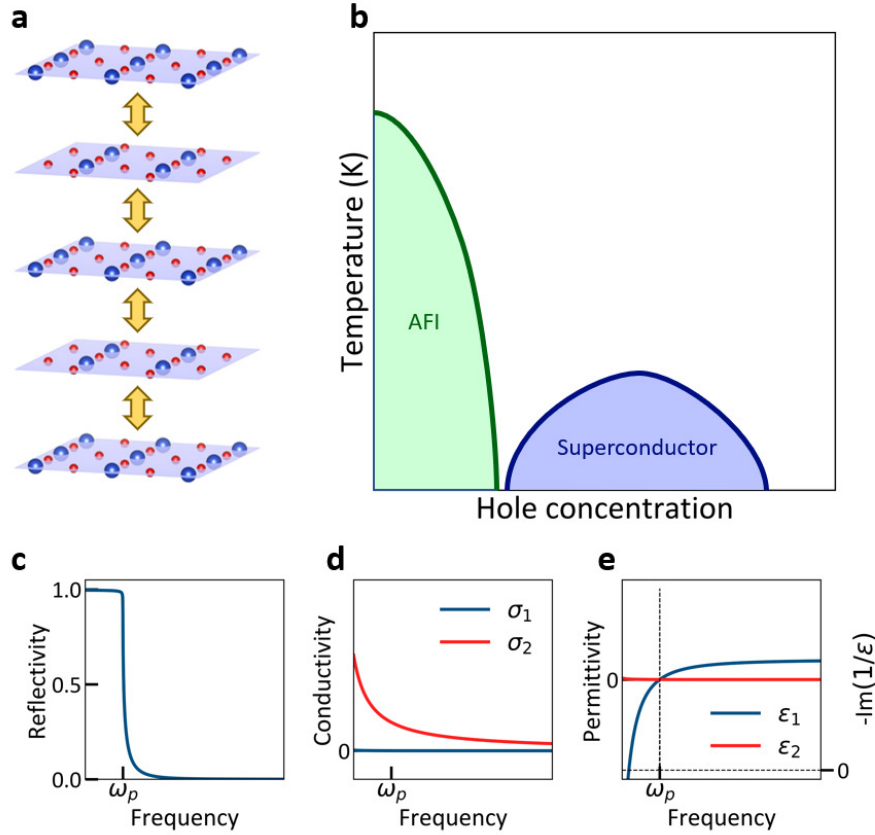


Figure 2.6: Summary of the typical properties of cuprates. **a** Quasi-2D copper (blue)-oxygen (red) layers are stacked along the c -axis and weakly coupled via insulating barriers. In the superconducting state, these insulating barriers form Josephson junctions, through which the super-carriers can tunnel, as represented by the yellow arrows. **b** The universal phase diagram of cuprates, in which an anti-ferromagnetic insulating (AFI) state gives way to a superconducting dome upon increasing the hole doping. **c, d, e** Calculated c -axis THz-frequency optical properties of the stack of Josephson junctions shown in **a**, typical of a single-layer cuprate in the superconducting phase. The divergent σ_2 and zero σ_1 at finite frequencies are typical of a superconductor (see section 2.1.4). Super-carriers are not able to effectively screen fields above the plasma frequency which, due to the Josephson junctions, is found in the THz-range in cuprates, resulting in an edge in the reflectivity at the so-called Josephson plasma frequency (ω_p). A zero crossing in the real part of the dielectric permittivity (ϵ_1) and a peak in the loss function ($-\text{Im}(1/\epsilon)$) also appear at ω_p .

metallic within the planes, but insulating in the perpendicular direction, conventionally labelled as the c axis. The electrodynamic properties of the superconducting phase can be modelled as a stack of quasi-two dimensional superconductors separated by insulating barriers. Such a geometrical arrangement, in which two superconductors are separated by an insulating barrier, is known as a Josephson junction [53, 54]. The insulating barrier in such a junction enables the order parameter to adopt a different phase in each superconducting layer, with the difference in phase between the two layers resulting in a spontaneous tunneling current which flows through the barrier.

The c -axis optical properties of the superconducting phase of cuprates can be modelled as a stack of such Josephson junctions, connected in series [55]. This means that, despite exhibiting insulating behaviour in the normal state above T_c , in the superconducting phase tunneling currents can run along the c -axis. These tunneling currents result in the emergence of a Josephson plasma resonance in the THz-frequency optical properties. The so-called Josephson plasma frequency is determined by the superfluid density, as well as other factors relating to the geometry of the junctions. As with a normal metallic plasmon, the Josephson plasmon appears as an edge in the reflectivity at the Josephson plasma frequency, below which the reflectivity is perfect. Correspondingly, a zero crossing in the real part of the permittivity and a peak in the dielectric loss function emerge at the Josephson plasma frequency. These features are summarized in figure 2.6c, d and e.

2.2.1 Light Induced Superconductivity in Single-Layer Cuprates

The first demonstration of light-induced superconductivity in a cuprate was the case of $\text{La}_{1.675}\text{Eu}_{0.2}\text{Sr}_{0.125}\text{CuO}_4$, reported in 2011 [1]. For this doping superconductivity is completely suppressed in equilibrium, with the system instead adopting a stripe-ordered phase in which there is a static one dimensional modulation of charge and spin density. This stripe-ordered phase is also associated with a structural distortion comprising a tilting of the oxygen octahedra.

In this experiment pulses tuned in resonance with an in-plane phonon mode which stretches a Cu-O bond at a wavelength of $15\ \mu\text{m}$ were used to excite the sample, and the subsequent changes in the THz-frequency optical properties were probed. It was observed that, subsequent to photo-excitation, the optical signatures of superconductivity, namely a divergent σ_2 and plasma-edge (signifying Josephson tunneling) in the c-axis reflectivity emerged. This effect was observed in a subsequent study at least up to the spin ordering temperature [56].

The observed loss of the effect upon tuning the pump wavelength away from the phonon resonance illustrates the importance of coupling between the light and the crystal structure. Furthermore, complementary time-resolved measurements of the reflectivity probed at 800 nm-wavelength after photo-excitation point towards a structural distortion which coincides temporally with the light-induced Josephson plasma edge. This has led to speculation that the pulse melts the stripe order which suppresses superconductivity in equilibrium by transiently weakening the tilting of the oxygen octahedra. Soft x-ray experiments carried out on the closely related compound $\text{La}_{1.875}\text{Ba}_{0.125}\text{CuO}_4$ have demonstrated that, for the mid-infrared excitation

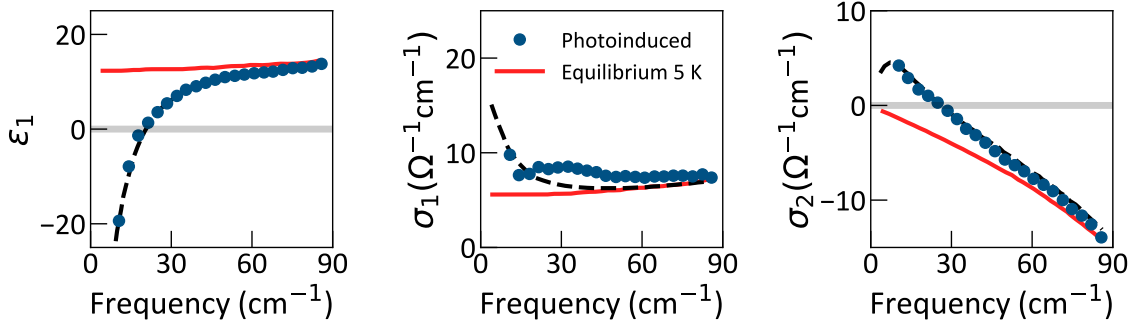


Figure 2.7: Optical properties of $\text{La}_{1.675}\text{Eu}_{0.2}\text{Sr}_{0.125}\text{CuO}_4$ in the equilibrium (non-superconducting) state at 5 K (red), and subsequent to mid-infrared photo-excitation (blue points). The photo-induced plasma edge is indicated by the zero crossing of the real part of the permittivity (ϵ_1). A fit to the photo-induced optical properties using a single plasmon model compatible with the interpretation of transient superconductivity is shown by black dashed lines. The data in this figure is taken from [56].

protocol used here, charge stripe order is indeed melted whilst leaving the lattice largely undisturbed [57].

In this picture, pre-existing superconducting fluctuations in two dimensions are assumed to be present within the planes in equilibrium, with coherent 3D transport being suppressed by the stripe order. Hence, when the stripe order is melted coherent 3D transport is restored. This proposed mechanism is illustrative of the potential of light to activate orders which are pre-existing but hidden in equilibrium.

Later experiments demonstrated a qualitatively similar effect in another single-layer cuprate, this time belonging to the $\text{La}_{2-x}\text{Ba}_x\text{CuO}_4$ family [2, 58]. For the doping of $x = 11.5\%$ studied in this work the superconducting transition temperature ($T_c = 13 \text{ K}$) is also suppressed by stripe order, which onsets below a temperature of $T_{\text{so}} =$

41 K. Photo-excitation with near-infrared pulses (of 800 nm wavelength) were shown to enhance superconductivity, manifested as a blue shift of the Josephson plasma frequency for base temperatures below T_c , and the emergence of a Josephson plasma edge for base temperatures above T_c but below T_{so} (as shown in figure 2.8). This was again interpreted as evidence for pre-existing fluctuating superconductivity above T_c , for which inter-layer coupling is suppressed by the stripe order.

The evidence for pre-existing underlying superconducting order in equilibrium

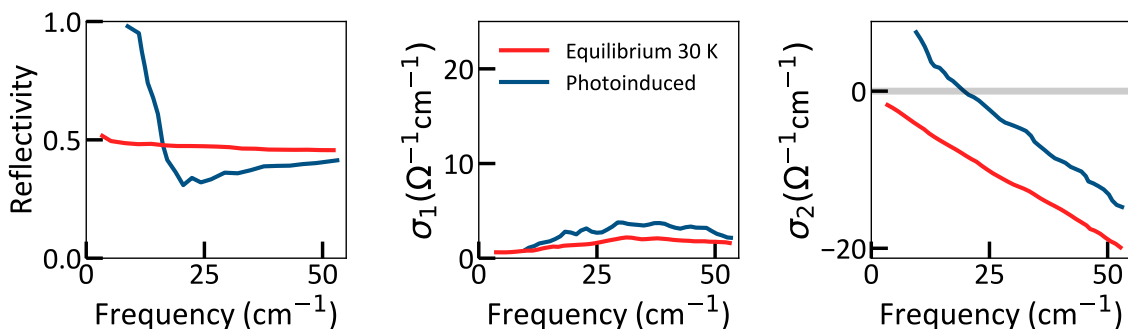


Figure 2.8: Optical properties of $\text{La}_{1.885}\text{Ba}_{0.115}\text{CuO}_4$ in the equilibrium (non-superconducting) state (red), and 1.5 ps after photo-excitation (blue) at a base temperature of 30 K. The data in this figure is taken from [2].

was strengthened by the demonstration of third harmonic generation in the same compound using intense single-cycle THz pulses. The third harmonic signal, which was attributed to nonlinear inter-plane Josephson tunneling, was observed to persist above T_c up to the stripe ordering temperature [59].

2.2.2 Light Induced Superconductivity in $\text{YBa}_2\text{Cu}_3\text{O}_{6+x}$

The first demonstration of light induced superconducting-like properties at room temperature was in $\text{YBa}_2\text{Cu}_3\text{O}_{6+x}$ [3, 4]. The crystal structure (which in this case contains two unique copper-oxygen layers per unit cell) of this family of compounds is shown alongside the phase diagram in figure 2.9 [60]. As is typical for a cuprate phase diagram, a superconducting-dome forms from an anti-ferromagnetic parent phase upon doping. The superconducting critical temperature is notably higher than for the single-layer compounds discussed previously, with $T_c = 94$ K at optimal doping.

In this case mid-infrared photo-excitation at a frequency close to 20 THz was shown to result in the re-emergence of superconducting-like optical properties, namely a Josephson plasma edge in the reflectivity and a divergence towards low frequencies in σ_2 , which decay on a few-ps timescale, as shown in figure 2.10. The temperature dependence of this effect was found to be heavily dependent on the level of hole doping. In this work three doping levels ($x = 0.45, 0.5$ and 0.6) were studied, with superconducting-like optical properties observed transiently after photo-excitation at base temperatures far above room temperature for the most under-doped ($x = 0.45$) sample. The same effect was observed up to maximum temperatures around 300 K and 200 K for $x = 0.5$ and 0.6 respectively.

This scaling of the maximum temperature with doping (also plotted as blue diamonds on top of the phase diagram in figure 2.9b) roughly coincides with the onset temperature T^* of the to-date poorly understood pseudogap phase. Even without speculating about the microscopic nature of the pseudogap phase this presents two

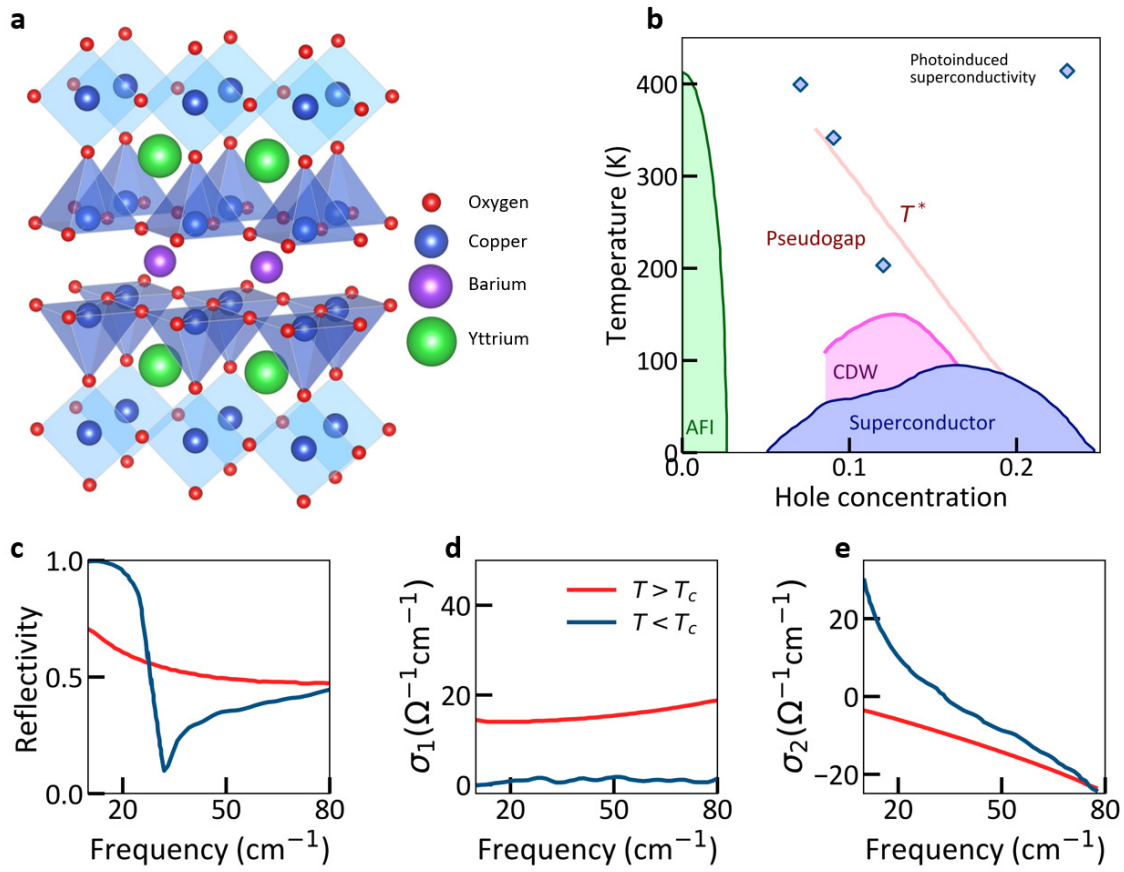


Figure 2.9: Summary of the properties of $\text{YBa}_2\text{Cu}_3\text{O}_{6+x}$. **a** Crystal structure (based on data from [61]) consisting of two copper-oxygen planes per unit cell, resulting in two transverse Josephson plasmons. **b** Phase diagram (constructed using data from references [62–67]) showing antiferromagnetic insulating (AFI), charge density wave (CDW) and superconducting states, as well as the pseudogap regime. Blue diamonds represent the highest base temperatures at which superconducting-like optical properties could be induced using light for several doping levels, from [68]. **c,d,e** THz-frequency optical properties measured along the c -axis, in the normal state above T_c (red) and in the superconducting state below T_c (blue), taken from [69]. Below T_c the lower frequency Josephson plasmon is visible as an edge in the reflectivity.

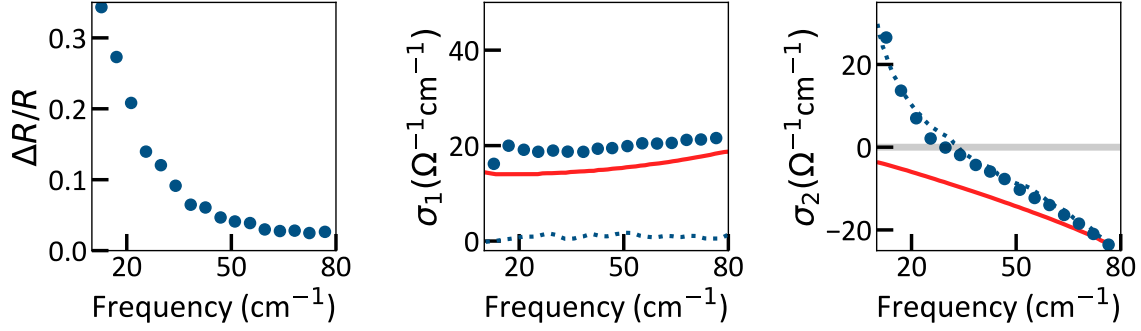


Figure 2.10: Changes to the optical properties of $\text{YBa}_2\text{Cu}_3\text{O}_{6.5}$ after photo-excitation at a frequency of 19.2 THz at a base temperature of 100 K. The photo-excited change in reflectivity, as well as the real and imaginary parts of the optical conductivity are shown as blue symbols. The equilibrium conductivity is shown as solid red lines above T_c , and dotted blue lines below T_c . The data in this figure is taken from [69].

possibilities: either the pseudogap phase competes with superconductivity, suppressing T_c in equilibrium (analogously to the effect of stripe and charge order in LESCO and LBCO), or it contains some crucial ingredients for the formation of light induced superconductivity which are missing for $T > T^*$. Indeed, with reference to table 2.1, the temperature at which long-ranged phase coherence is predicted to be lost coincides roughly with T_c for these compounds, presenting the possibility that Cooper pairs may survive at higher temperatures. These pre-formed Cooper pairs could be exactly the ingredients required for the formation of light-induced superconductivity. Experimental support for this idea comes in the form of Nernst effect measurements, which show direct signatures of Cooper pairs above T_c , although admittedly not for temperatures as high as T^* [62].

The broad excitation spectrum centered at 20 THz is approximately resonant with a pair of apical oxygen phonon modes at 17 THz and 20 THz respectively. The impor-

tance of exciting these modes was underscored by a further study, in which a new optical setup (that which was also later used to study the pump-frequency dependence of light induced superconductivity in K_3C_{60} which forms the subject of chapter 4 in this thesis) provided frequency-tuneable narrow-bandwidth pulses throughout the THz-mid infrared region [70]. Here it was reported that the superconducting-like optical properties could only be observed when the drive was tuned resonant to these specific modes, and that resonantly driving other modes at different frequencies did not give a comparable effect [69].

The natural next step towards understanding how the superconducting-like optical properties arise is to study the microscopic dynamics which follow the all-important excitation of these apical oxygen phonon modes. Several studies have been carried out both using x-rays and ultra-short near-infrared pulses to probe the sample after photo-excitation, providing information about the lattice dynamics [71–74]. Here I will focus on experiments in which the dynamics of odd-symmetry modes (meaning modes which transiently break inversion symmetry when displaced) were measured via second harmonic generation from an ultrafast 800 nm probe pulse which is incident on the sample after the mid-infrared excitation pulse [75, 76].

In the language of non-linear optics, the polarization (P) induced by an electric field (E) inside a material can be expanded as a Taylor series in powers of the electric field, with the coefficient of the n^{th} term denoted by $\chi^{(n)}$:

$$P = \chi E + \chi^{(2)} E^2 + \chi^{(3)} E^3 + \dots \quad (2.12)$$

In this equation the second order term can result in the generation of a field at the second harmonic frequency, but for a centro-symmetric medium $\chi^{(2)} = 0$ by symmetry. This is the case for $\text{YBa}_2\text{Cu}_3\text{O}_{6+x}$, such that in the absence of the excitation pulse or any coherent dynamics there is no second harmonic intensity. However, coherent motion of odd symmetry modes can transiently break inversion symmetry, such that there will be a finite generated intensity at the second harmonic wavelength. This can be seen by expanding $\chi^{(2)}$ as a function of the coordinates of all inversion symmetry-breaking modes in the material:

$$\chi^{(2)} = \sum_i \frac{\partial \chi^{(2)}}{\partial Q_i} \Delta Q_i \quad (2.13)$$

Consequentially, following an excitation which launches coherent motion of one or more odd symmetry modes, $\chi^{(2)}$ becomes effectively non-zero within each cycle of said modes, such that a comparably short probe pulse can generate second harmonic. One further source of light close to the second harmonic frequency comes from a direct mixing of the excitation pulse with the probe pulse via $\chi^{(3)}$, provided the frequency of the excitation pulse is negligible compared to the probe pulse as is the case here [77].

$$P_{\text{SHG}} = \chi^{(3)} E_{\text{pump}} E_{\text{probe}}^2 + \sum_i \frac{\partial \chi^{(2)}}{\partial Q_i} \Delta Q_i E_{\text{probe}}^2 \quad (2.14)$$

In summary, the polarization inside the sample will oscillate (and generate light) with a frequency component close to the second harmonic of the probe, given by equation 2.14. The second term in equation 2.14 shows that the intensity of the generated second harmonic will be modulated by the coherent motion of the odd-symmetry modes. This means that by scanning the relative delay between the excitation and probe pulses this motion can be traced as a function of time.

The data from this experiment is summarized in figure 2.11. After subtracting the signal which arises from the $\chi^{(3)}$ term (which simply follows the envelope of the excitation pulse), then taking the fourier transform, the spectral content of the coherent oscillations is revealed. This includes peaks at the frequencies of the apical oxygen phonon modes which have been resonantly excited by the pump pulse. Surprisingly, the response is dominated by an additional peak centered at 2.5 THz. There is no known odd-symmetry mode present at this frequency, however a clue to the origin of the peak comes from the temperature dependence. Unlike the phonon peaks, which have an approximately constant amplitude throughout the measured range from 5 K to 400 K, the amplitude of the mysterious low-frequency peak drops to zero at approximately 400 K for a doping level of $x = 0.48$. However, for a doping level of $x = 0.65$ the amplitude reaches zero at around 300 K. This doping/temperature dependence is also in rough agreement with the pseudo-gap phase, and is highly reminiscent of that of the light-induced superconducting-like response in the THz-frequency optical properties, drawing a connection between the two phenomena.

In the same work, the authors proposed a theoretical model which assigns the observed 2.5 THz oscillations to a Josephson plasmon mode which is seeded due to fluctuations that persist throughout the pseudo-gap phase, and parametrically amplified by the high-amplitude driving of the apical oxygen phonon modes. Further theoretical study showed that such a scenario, in which a coherently oscillating Josephson plasma mode is present in the sample above T_c would give rise to the previously-observed superconducting-like optical properties [78, 79].

This mechanism again highlights the importance of fluctuating superconductiv-

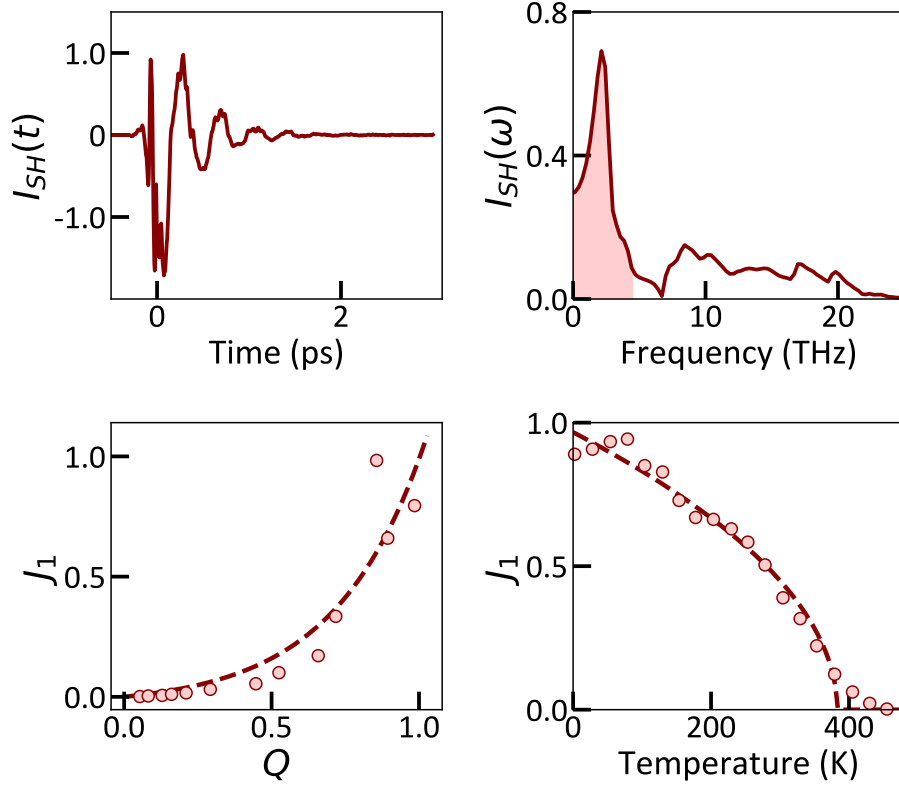


Figure 2.11: Summary of time-resolved second harmonic generation measurements on $\text{YBa}_2\text{Cu}_3\text{O}_{6.48}$. Top row: second harmonic intensity after background subtraction, as a function of pump-probe time delay (left), and its Fourier spectrum (right). The plasmon peak at low frequencies is indicated by red shading. Bottom row: Scaling of the plasmon peak amplitude with the phonon peak amplitude extracted from pump fluence-dependent data (left) and with temperature (right). The dashed red lines indicate an exponential fit to the phonon amplitude-dependence and a mean field fit ($J_1 \propto \sqrt{1 - T/T^*}$) to the temperature dependence. The data in this figure is taken from [75].

ity in equilibrium for the manifestation of light-induced superconductivity, as was also thought to be the case for the previous experiments on the single layer cuprates LBCO and LESCO. However, whereas in those cases the absence of macroscopic superconductivity in equilibrium was attributed to the existence of competing phases, here it is presumed to be a consequence of thermal fluctuations of the phase of the order parameter. Consequentially, whilst in the single-layer cuprates the apparent path towards light-induced superconductivity was paved via melting of the relevant competing order, in the case of YBCO a forced synchronization of the phase degree of freedom is instead considered. The mechanism for this synchronization is parametric amplification of Josephson plasmons, seeded by fluctuating superconductivity which is presumed to be significant throughout the pseudo-gap phase.

These observations presents a recipe for identifying new candidate materials for light-induced superconductivity, as the essential ingredients here seem to be an optically accessible mode of the crystal which provides effective coupling to light (the apical oxygen phonons in this case), accompanied by fluctuating superconductivity above T_c .

2.3 Light-Based Control of Molecular Superconductivity

This recipe has now been extended to the realm of superconductivity in molecular solids, firstly in experiments on K_3C_{60} , which will form the subject of all later chapters, and in the charge transfer salt κ -(BEDT-TTF) $_2$ Cu[N(CN) $_2$]Br, which will be discussed briefly in this section.

In the atomic crystals discussed up to this point, excitation with mid-infrared pulses can couple resonantly to phonon modes of the crystal structure close to zero momentum, enabling transient long-range distortions. Molecular solids, in which entire molecules (as opposed to individual atoms) are arranged in a crystal structure, retain their local degrees of freedom within the crystal environment. Broadly speaking, the phonon modes of such materials can be divided into two categories - local vibrational modes of the individual molecules and lattice modes associated with motion of the centre of mass of each molecule. These two categories are illustrated in figure 2.12 panels a and b, respectively. Ordinarily, these two classes are also separated in energy, with the local vibrational modes involving the modulation of strong intramolecular bonds and light individual atoms having much higher frequencies than the lattice modes which move the heavy molecules against weaker inter-molecular bonds.

Using light to resonantly drive such a local vibrational mode and therefore modulate the local interactions has been successfully demonstrated in the 1D Mott insulator ET-F₂TCNQ, where the Hubbard U (representing the mutual on-site coulomb repulsion of two electrons) was modulated [80, 81]. Because the coupling between U and the driven vibrational mode is quadratic in the mode coordinate, the modulation of U consisted of both a rectified component (meaning a time-averaged change compared to its equilibrium value), and a quickly oscillating component at twice the frequency of the drive.

This principle has been applied to the molecular superconductor κ -(BEDT-TTF)₂Cu[N(CN)₂]Br, in which light was used to resonantly excite a vibrational mode of the BEDT-TTF molecule, predicted by theoretical calculations to couple to the local electronic in-

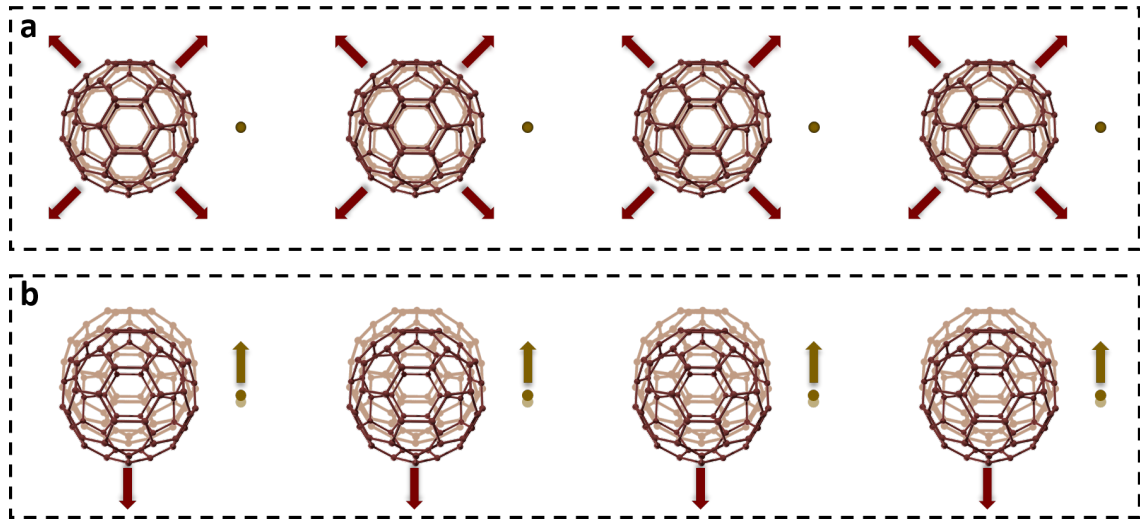


Figure 2.12: Cartoon illustration of the distinction between molecular modes and phonon modes in a fictitious 1D solid consisting of a chain of molecules separated by individual atoms. **a** A molecular mode consisting of stretching of the individual molecules, as indicated by the red arrows, without significant changes in the centre of mass position of each molecule. **b** A phonon mode in which the structure of each molecule is not significantly distorted, but the centre of mass of each molecule moves relative to the position of the neighboring atom, as indicated by the red and orange arrows.

teraction parameters [82]. Crucially, Nernst effect measurements carried out on this compound display signatures of the pre-formation of Cooper pairs at temperatures higher than T_c [83], just like the case of under-doped $\text{YBa}_2\text{Cu}_3\text{O}_{6+x}$ described in the previous section.

Time-resolved measurements of the THz frequency optical properties revealed signatures of superconductivity (a divergent σ_2 and the opening of a gap in σ_1) emerging transiently after photo-excitation, with qualitative resemblance to the results of the previously-discussed earlier experiments on cuprates [6].

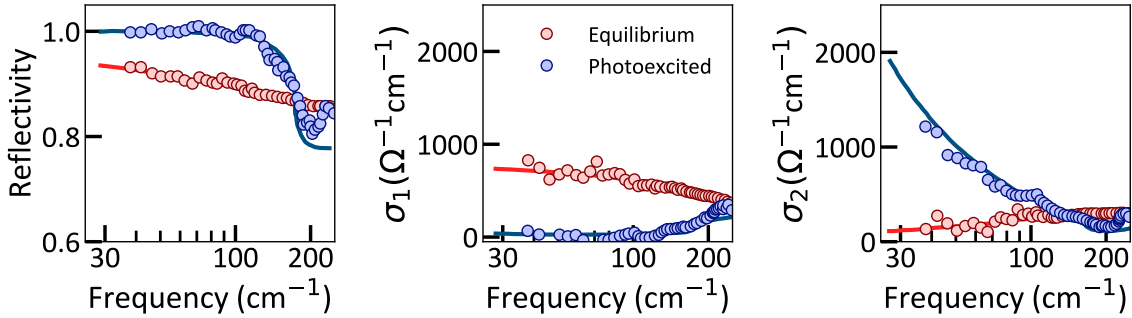


Figure 2.13: Reflectivity, real (σ_1) and imaginary (σ_2) parts of the optical conductivity of κ -(BEDT-TTF) $_2$ Cu[N(CN) $_2$]Br measured 1 ps after photo-excitation at a base temperature of 30 K ($T_c = 12.5$ K). A Mattis-Bardeen fit to the photo-excited data and a Drude fit to the equilibrium data are shown as solid lines. The data in this figure is taken from [6].

In this case the superconducting-like state could only be induced for base temperatures below 50 K (still far above the equilibrium $T_c = 12$ K), a temperature scale which coincides with the onset of coherent transport in equilibrium. Further studies on other compounds from the same family - namely κ -(BEDT-TTF) $_2$ Cu[N(CN) $_2$]Cl and κ -(BEDT-TTF) $_2$ Cu(NCS) $_2$ - revealed that superconducting-like optical proper-

ties could only be activated by light in the original Br-based compound and no comparable effect was observed in either of the other two compounds [84]. As (unlike the original Br-based compound) neither the Cl nor the $\text{Cu}(\text{NCS})_2$ -based compounds exhibit signatures of pre-formed Cooper pairs above T_c in equilibrium, this is consistent with the idea that optical driving can help to synchronize pre-existing pairs.

Chapter 3

Superconductivity in Alkali-doped Fullerides

Superconductivity in K_3C_{60} , a member of the alkali-doped fulleride family of compounds, was first discovered in 1991[85]. To date, the alkali-doped fullerides remain the class of molecular solids with the highest known superconducting critical temperature, with $T_c \approx 40$ K being demonstrated in Cs_3C_{60} under pressure [86, 87].

In K_3C_{60} , which will form the subject of the rest of this thesis, photo-excitation with mid-infrared light pulses has been demonstrated to yield a metastable state with superconducting-like properties, far above the equilibrium superconducting critical temperature of 20 K [5, 88–91]. This chapter will provide a broad overview of the properties of the alkali-doped fullerides, followed by a more detailed review of previous experiments which have investigated the phenomenon of so-called light-induced superconductivity in K_3C_{60} .

3.1 Equilibrium Properties

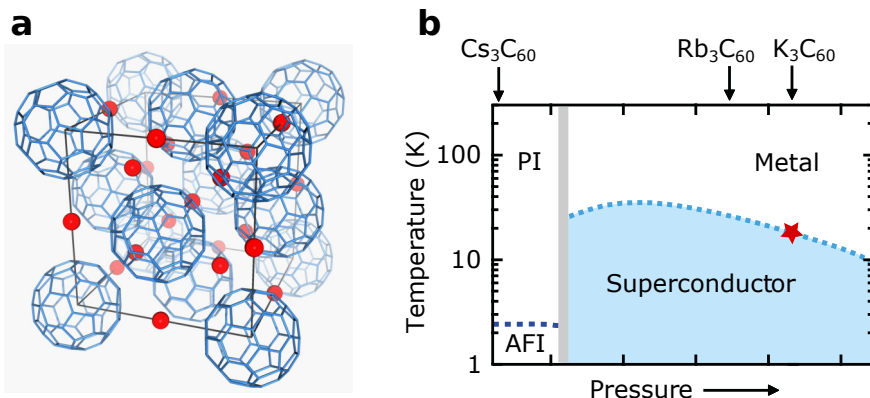


Figure 3.1: Crystal structure and phase diagram of the alkali-doped fullerides. In **a** the C₆₀ fulleride molecules are shown as blue cages arranged in a face-centred-cubic structure, with the alkali atoms as red spheres. **b** shows the phase diagram based on data from [92], with paramagnetic (PI) and anti-ferromagnetic (AFI) insulating phases giving way to metallic behaviour and a superconducting dome as the lattice constant is decreased through either the application of pressure or the substitution of a smaller alkali species. The red star indicates the superconducting transition in K₃C₆₀ with zero applied pressure, with a transition temperature of 20 K. This figure is adapted from [93].

The alkali-doped fullerides share a common structure, which consists of a face-centred-cubic lattice of C₆₀ molecules with three alkali atoms per molecule occupying the spaces between, as illustrated in figure 3.1a [94]. Note that although Cs₃C₆₀ can alternatively be synthesized with an A15 structure in which the C₆₀ molecules occupy the points of a body-centred cubic lattice [95], the discussion in this thesis will be restricted to the face-centred-cubic fullerides.

Undoped C₆₀ forms a band insulator. Upon doping, the highest-energy electron in each alkali atom (which does not belong to a closed shell) give rise to a partially-

occupied conduction band. However, as shown by the phase diagram in figure 3.1b, for the compound with the most expanded lattice (Cs_3C_{60} at ambient pressure) the system is instead a Mott insulator [96, 97].

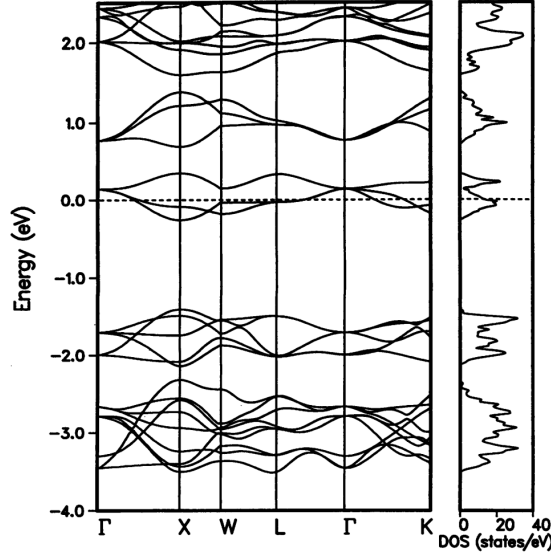


Figure 3.2: Band structure and density of states (DOS) of K_3C_{60} as determined by DFT calculations. The Fermi energy is indicated by a dashed line. This figure is taken from [98]. Reprinted with permission from AAAS.

As well as donating electrons, the alkali atoms also modify the spatial separation of the fullerene molecules. By changing the alkali dopant from caesium to rubidium and then to potassium (i.e progressively moving from larger to smaller atoms) the inter-molecular distance decreases. The inter-molecular distance can alternatively be tuned by the application of pressure. In both cases, the resulting enhancement in electronic hopping between molecules gives rise to a cross-over into a metallic region of the phase diagram at high temperatures. The emergence of metallicity at high temperatures is accompanied by a superconducting dome, superficially similar

to those seen in the phase diagrams of strongly-correlated superconductors including cuprates, with a maximum T_c of 40 K found in Cs_3C_{60} under an applied pressure of 7 kBar [92].

The band structure of K_3C_{60} derived from DFT calculations is shown in figure 3.2 [98]. The Fermi energy crosses three bands which are degenerate at the Γ point, which arise from three degenerate C_{60} orbitals with t_{1u} character. The energy gap to the next set of unoccupied bands is on the order of 1 eV.

As is typical for a molecular solid (see section 2.3), the phonon modes can be roughly divided into two categories - those which resemble the vibrational modes of a C_{60} molecule (for example in the gas phase), and those which predominantly modulate the A- C_{60} distances without much distortion of the individual C_{60} molecules. Because the intra-molecular bonds between carbon atoms are much stiffer than the ionic attraction force between the alkali atoms and the neighboring C_{60} molecules, the molecular vibrational-type modes appear at higher frequencies compared to the crystal phonon-type modes. For the case of K_3C_{60} , where the conduction electrons largely screen the phonon contributions to the optical properties, the phonon modes are clearest in the inelastic neutron scattering spectrum from [99], shown here in figure 3.3.

Figure 3.3 shows a gap in the phonon spectrum around 6 THz, separating the phononic and molecular vibrational modes (see figure 2.12). Roughly speaking, the molecular modes can be further subdivided into two categories according to whether the distortion of the molecule is predominantly tangential or radial. This is somewhat analogous to the distinction between in-plane and out-of-plane modes in graphene,

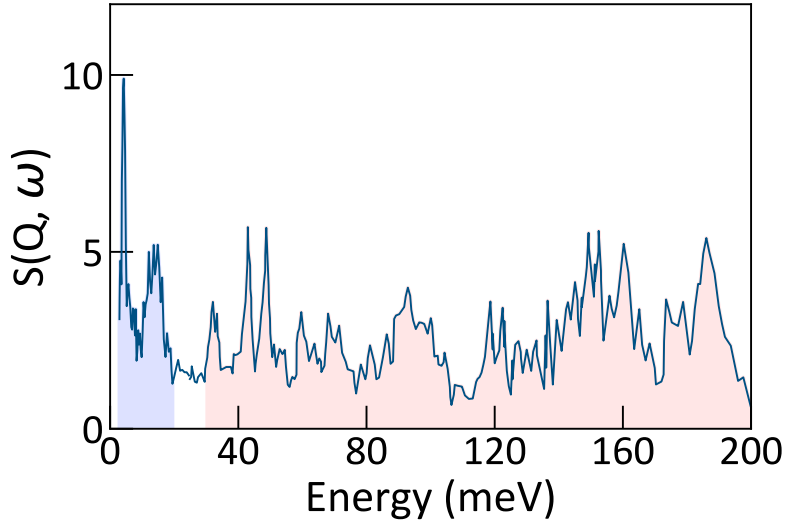


Figure 3.3: Inelastic neutron scattering spectrum of K_3C_{60} measured at 5 K and 30 K and summed. Blue shading indicates phonon modes in which the center of mass of each molecule is modulated relative to the positions of the alkali atoms, whereas pink shading indicates the phonon modes which predominantly modulate the structure of the individual molecules with less centre of mass motion. The data in this figure is taken from [99].

and in most cases the radial modes appear at lower frequencies compared to the tangential modes.

The superconducting transition in K_3C_{60} is evidenced by a drop to zero resistance and the emergence of a Meissner effect, plotted here in figure 3.4. The details of the pairing mechanism are still the subject of debate, with some variance in the ratio $2\Delta/k_B T_c$ being reported in the literature. THz-frequency optical probing [101], photo-emission [102] and NMR measurements [103] have all been reported giving values close to the weak-coupling BCS prediction of 3.53. On the other hand, Raman spectroscopy-based [100] and tunneling-based measurements [104, 105] as well

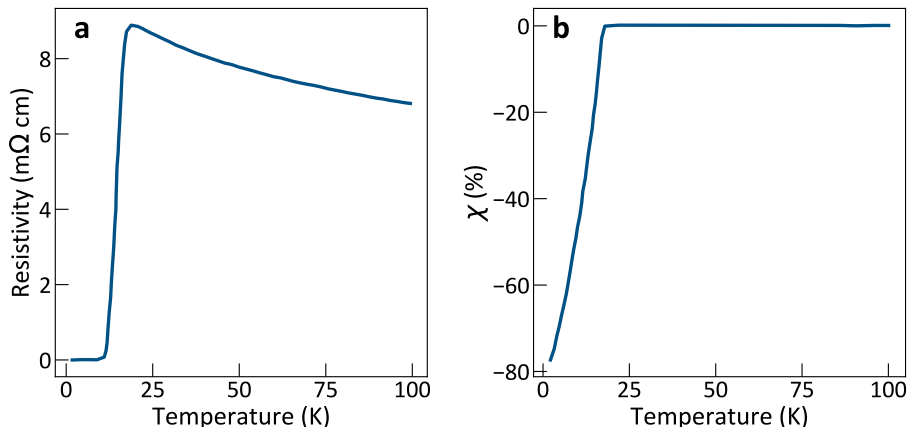


Figure 3.4: The static metal-superconductor transition in K_3C_{60} , as evidenced by **a** vanishing resistivity and **b** changes to the zero-field-cooled magnetic susceptibility (χ) signifying the emergence of a Meissner effect, upon cooling below $T_c = 19.8$ K. The data in this figure is taken from [100].

as other NMR measurements [106] show higher values for the gap to critical temperature ratio, instead pointing towards either strong-coupling or unconventional pairing. In the first (weak coupling) scenario, the relatively high transition temperature can be reconciled as resulting from the very high phonon frequencies which arise due to the stiff intra-molecular bonds [107]. However, the existence of the Mott insulating state for larger lattice constants implies that the coulomb repulsion between electrons occupying the same site should also be a competing energy scale in these compounds. Indeed, $2\Delta(T = 0)/k_B T_c$ actually deviates significantly further from the BCS prediction on the more expanded side of the phase diagram closer to the Mott insulating state [108].

Direct evidence for the role of phonons in the superconducting pairing mechanism has been provided in the form of isotope effect measurements. As explained in section

2.1.1, conventional BCS theory predicts a scaling $T_c \propto M^{-\alpha}$ with $\alpha = 0.5$ (where M is the atomic mass). Several studies have shown the existence of an isotope effect upon substitution of the carbon isotope ($^{12}\text{C} \rightarrow ^{13}\text{C}$), although with significant disagreement over the value of α . The most complete substitution was achieved in [109], where a value $\alpha = 0.3$ was determined. Other studies with less complete substitution gave higher values of α [110–112]. This could be because partial substitution of ^{13}C within each molecule would alter the symmetry of the molecule and hence the vibrational modes, resulting in changes to the electron-phonon coupling strength which is an additional effect alongside the conventional re-normalization of the vibrational frequencies.

In contrast, studies on Rb_3C_{60} have demonstrated that substitution of the Rb isotope has little effect on T_c [113, 114]. This means that phonon modes which involve significant motion of the alkali atoms are not expected to contribute to the pairing interaction. Instead, these observations point strongly towards the crucial role of the molecular modes, those which closely resemble the vibrational modes of an isolated C_{60} molecule, in the pairing mechanism.

Arguments based on the icosahedral symmetry of a single C_{60} molecule suggest that only the A_g and H_g molecular vibrations should couple to the three t_{1u} bands which cross the Fermi energy, although the lower symmetry due to the crystal environment in principle enables coupling to other modes [107, 115]. Nevertheless, the strongest electron-phonon coupling is to the H_g modes, as evidenced experimentally by significant broadening of the H_g peaks observed in Raman spectra when comparing undoped C_{60} (in which the t_{1u} orbitals are unoccupied) to K_3C_{60} [116, 117]. This suggests that the H_g modes may be the most important with regards to the pairing

mechanism for the formation of superconductivity.

One theory which attempts to reconcile the seemingly paradoxical co-existence of phonon-mediated s-wave pairing and very strong electronic coulomb repulsion (as evidenced by the nearby Mott insulating phase) has been proposed by considering the effect of distortions of these H_g modes on the t_{1u} orbitals which cross the Fermi energy [118]. This theoretical work argues that superconductivity can be greatly enhanced by a dynamical Jahn-Teller distortion along the H_g coordinates which lifts the orbital degeneracy, effectively inverting Hund's rules and favouring the formation of a spin singlet on each site - as illustrated in figure 3.5b.

Ab initio theoretical calculations inspired by this idea have successfully reproduced the experimentally-measured alkali-doped fulleride phase diagram [119, 120]. The full model considers a Hamiltonian for the t_{1u} orbital and phonon degrees of freedom, with interaction parameters determined by various Density Functional Theory (DFT) calculations. The resulting Hamiltonian consists of the five terms illustrated in figure 3.5a. The intra-orbital repulsion is given by U_{eff} , with the inter-orbital repulsion for opposite spins given by U'_{eff} . The effective exchange is given by J_{eff} , which determines the energy cost of both pair-hopping and spin-flipping processes, and the intra-orbital repulsion for like spins is given by $U'_{\text{eff}} - J_{\text{eff}}$. These parameters are all denoted as 'effective', because they include contributions from electron-phonon coupling.

Due to the effective negative exchange which arises from the dynamical Jahn-Teller distortion as described above, it was found that $U'_{\text{eff}} > U_{\text{eff}}$, meaning it is energetically favourable for a spin singlet to form on each site. This Hamiltonian was solved

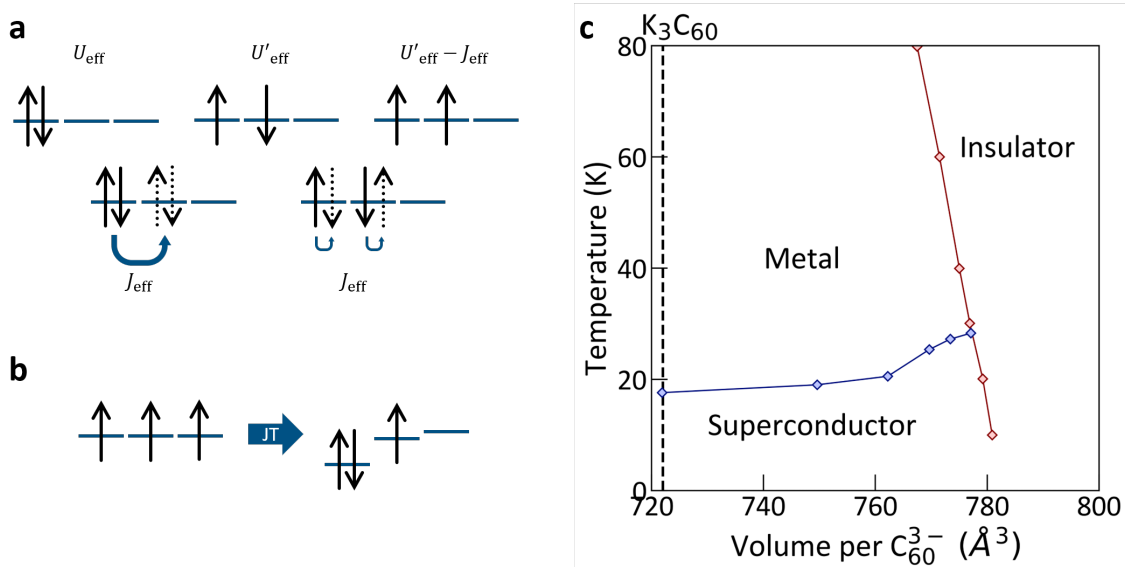


Figure 3.5: Model of phonon-assisted strongly correlated superconductivity in A_3C_{60} . **a** schematic illustration of the electron-electron interaction terms which are considered in the Hamiltonian. Clockwise from the top left these are: intra-orbital coulomb repulsion, inter-orbital (with opposite spin) coulomb repulsion, inter-orbital (with parallel spins) coulomb repulsion, spin-flip and pair-hopping. All parameters are re-normalized to take into account the electron-phonon interactions. **b** A dynamical Jahn-Teller distortion results in the formation of a spin-singlet on each site, which is favourable for superconductivity. **c** The predicted phase diagram which arises from this model, showing fairly good agreement with experiment. Panels **a** and **b** are adapted from [120], and the data in panel **c** is taken from [119].

using dynamical mean field theory, leading to the predicted phase diagram shown in figure 3.5c, which is broadly consistent with the experimental phase diagram in figure 3.1.

The authors were able to gain more insight into the most important factors for superconductivity by artificially tuning individual terms and examining whether the superconducting solution survived. They found that superconductivity was destroyed in the absence of the pair hopping term, and also for the case $U'_{\text{eff}} < U_{\text{eff}}$. This suggests that the two critical ingredients for superconductivity are the formation of on-site spin singlet pairs (which results from $U'_{\text{eff}} > U_{\text{eff}}$), and the ability of these pairs to hop between orbitals.

Returning to experimental observations, the superconducting transition in K_3C_{60}

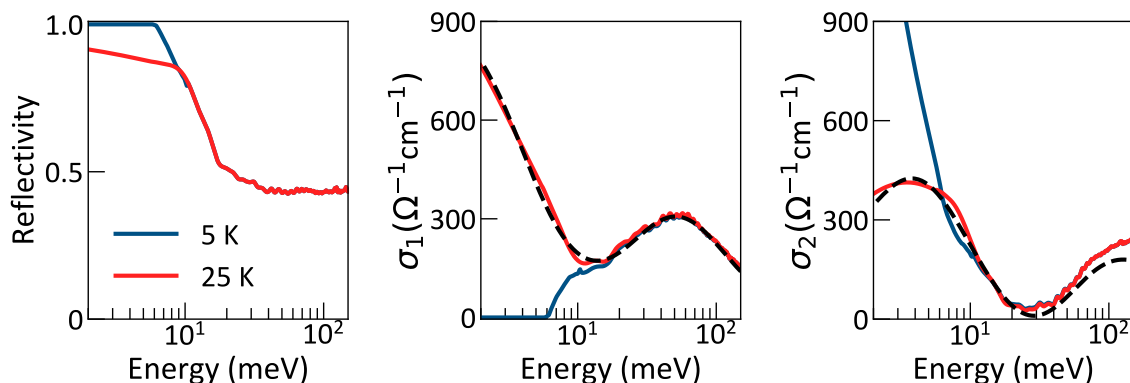


Figure 3.6: Reflectivity (sample-diamond interface) and real (σ_1) and imaginary (σ_2) parts of the optical conductivity measured below (blue) and above (red) T_c , measured via FTIR spectroscopy. The dashed black line is a Drude-Lorentz fit to the 25 K data as detailed in the text. The data in this figure is taken from [5].

can also be observed via dramatic changes in the THz-frequency optical proper-

ties consistent with the general picture for a superconductor described in section 2.1.4. The equilibrium optical properties of the powder samples used in the mid-infrared photo-excitation experiments, measured via Fourier Transform InfraRed spectroscopy (FTIR) are shown in figure 3.6, for temperatures above and below T_c . The normal state properties (above T_c) have been fitted with a Drude-Lorentz model given by equation 3.1:

$$\sigma(\omega) = \frac{\Lambda_D}{\gamma_D - i\omega} + \frac{\Lambda_L\omega}{i(\Omega^2 - \omega^2) + \gamma_L\omega} \quad (3.1)$$

This model consists of a Drude response (as given by equation 2.8) at low frequencies and an additional Lorentz oscillator which is required to capture the broad mid-infrared peak centered at around 50 meV. The parameter values for the fit shown in figure 3.6 are given in table 3.1. Compared to data measured on single crystal samples, both the carrier density and scattering rates are reduced by approximately a factor of 4 [121]. Upon cooling below T_c , all spectral weight in the real part of the

Parameter	Value
Λ_D	3992 $\Omega^{-1}\text{cm}^{-1}\text{meV}/\hbar$
γ_D	4.18 meV/\hbar
Λ_L	36,842 $\Omega^{-1}\text{cm}^{-1}\text{meV}/\hbar$
Ω	52.3 meV/\hbar
γ_L	122.6 meV/\hbar

Table 3.1: Parameters (defined by equation 3.1) extracted from the fit of the normal state optical properties at 25 K plotted in figure 3.6.

optical conductivity (σ_1) is lost below 6 meV, and correspondingly the reflectivity goes to 1 in the same frequency range, in agreement with single-crystal data [101]. This results from the opening of the superconducting gap which has an approximate

value $2\Delta \approx 6$ meV in K_3C_{60} . Correspondingly, σ_2 exhibits the expected $1/\omega$ -like divergence, indicating (through Kramers-Kronig relations) that the lost spectral weight has moved into a pole at zero frequency in σ_1 .

The origin of the 50 meV peak in σ_1 , visible both above and below T_c and here captured by the Lorentz oscillator term, has been debated, with an extensive discussion presented in [121].

In all cases of light-induced superconductivity discussed in chapter 2, there was a strong connection to the pre-existence of some form of superconducting behaviour above T_c in equilibrium. For the case of K_3C_{60} , tantalizing evidence for the existence of pre-formed cooper pairs above T_c has been provided by tunneling measurements in very thin tri-layer samples [105]. To determine if some remnants of superconducting order may also survive above T_c in bulk K_3C_{60} , Nernst effect measurements have been carried out [122]. The results are suggestive of superconducting fluctuations persisting up to a temperature of 80 K, far above T_c . One possible interpretation of this data is that (as is thought to be the case for underdoped YBCO) the state above T_c may involve pre-formed cooper pairs and thus a finite amplitude of the order parameter, with long-ranged superconducting coherence suppressed by thermal fluctuations of the phase.

3.2 Light Induced Metastable Superconductivity in K_3C_{60}

As discussed in chapters 1 and 2, the use of light to resonantly drive collective vibrational modes in solid materials is now well established as a means to achieve functional control of material properties. The first part of this chapter described how K_3C_{60} exhibits high temperature superconductivity, which is mediated by molecular vibrations. This makes K_3C_{60} a promising candidate for using light to drive those molecular vibrations to large amplitudes in an attempt to control superconducting order.

This idea provided the motivation for the experimental work published in [5]. In this work, excitation pulses were tuned to be resonant with high frequency infrared-active vibrational modes at approximately 170 meV photon energy. The reflectivity and complex conductivity of the sample in the THz frequency range were then measured as a function of pump-probe time delay, in order to observe how the electronic properties of the material evolve over time in response to excitation.

Figure 3.7 shows the reflectivity, real and imaginary parts of the THz conductivity of K_3C_{60} measured both in equilibrium and after mid-infrared photo-excitation at various base temperatures above the superconducting critical temperature. The extracted optical properties after photo-excitation at 25 K and 100 K bear a striking resemblance to the equilibrium optical properties in the superconducting phase (see figure 3.6). Namely, there is a complete loss of spectral weight in the real part of the optical conductivity (σ_1) within the measured frequency range, accompanied by

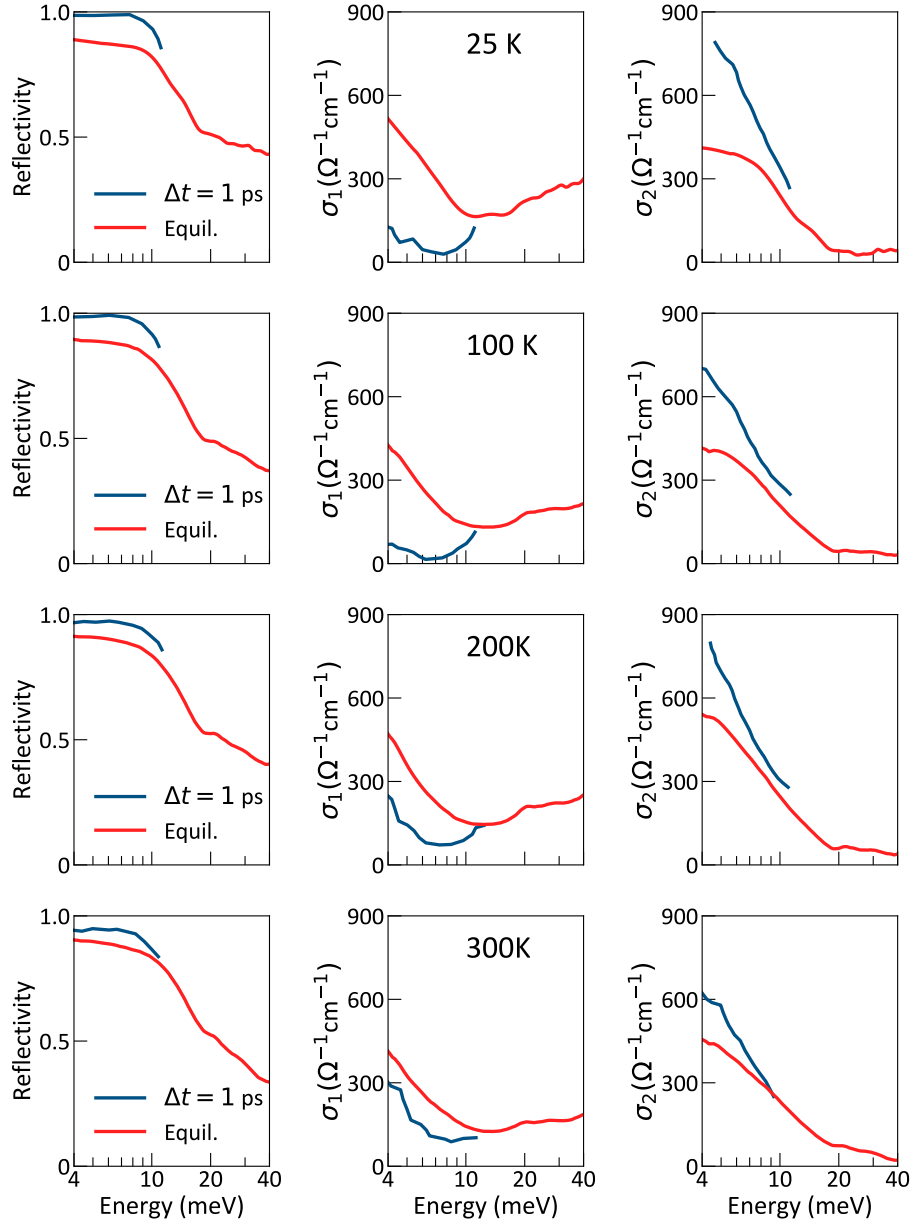


Figure 3.7: Reflectivity, real (σ_1) and imaginary (σ_2) parts of the optical conductivity measured in equilibrium (red) and 1 ps after photo-excitation with a fluence of 1.1 mJcm^{-2} (blue), at four different temperatures. Data taken from [5].

a $\sim 1/\omega$ divergence in the imaginary part (σ_2). This observation is the first piece of evidence for light-induced superconductivity in K_3C_{60} . At higher temperatures (d-e) there is also some loss of spectral weight in σ_1 (reduced compared to the lower temperature data) accompanied by an enhancement in σ_2 , signifying an increase in the carrier mobility.

Figure 3.8 shows that with a fluence of 1.1 mJcm^{-2} at base temperature 25 K

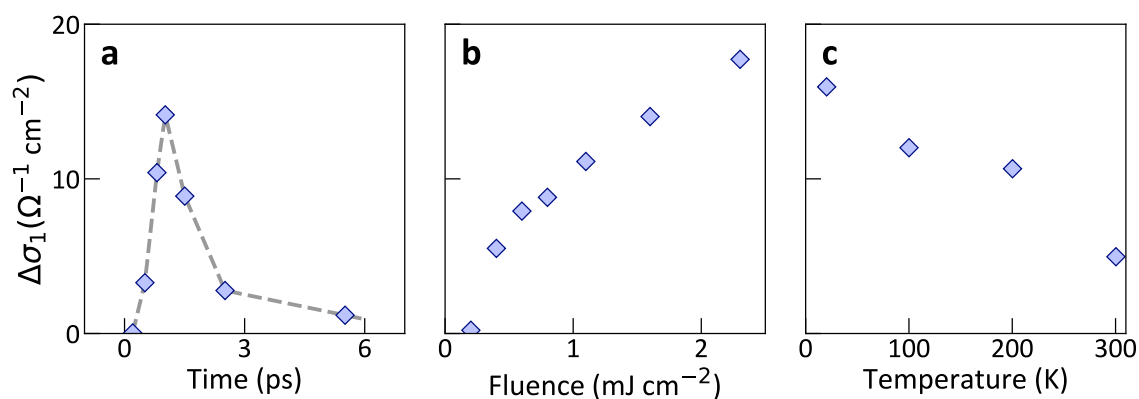


Figure 3.8: Dependence of the photo-induced reduction in spectral weight (integrated from 0.75 to 2.5 THz) of the real part of the optical conductivity ($\Delta\sigma_1$) on (a) pump-probe time delay, (b) excitation fluence and (c) base temperature. Data taken from [5].

superconducting-like optical properties were measured after photo-excitation on a time-scale of roughly 2 ps before relaxing back to their equilibrium values. However, the fluence dependence shows that the photo-induced changes are not saturated in this driving regime, raising the possibility that with either stronger or more efficient driving the observed effect could be enhanced.

The second piece of evidence for light induced superconductivity in K_3C_{60} comes

in the form of the pressure dependence, which was measured in the later work [88]. In this work, the authors repeated the same mid-infrared photo-excitation, THz-TDS probe experiment, whilst simultaneously using a diamond anvil cell to apply pressure to the K_3C_{60} sample. As discussed in section 3.1, applying pressure in the metallic state of K_3C_{60} (for $T > T_c$) increases the DC conductivity, whilst reducing the superconducting critical temperature. For this reason the pressure dependence of the optical properties of the photo-induced superconducting-like state could help to distinguish between a photo-induced high-mobility metallic state and a photo-induced superconducting-like state.

Figure 3.9 shows the pseudo-DC conductivity (σ_0) extrapolated from a Drude-

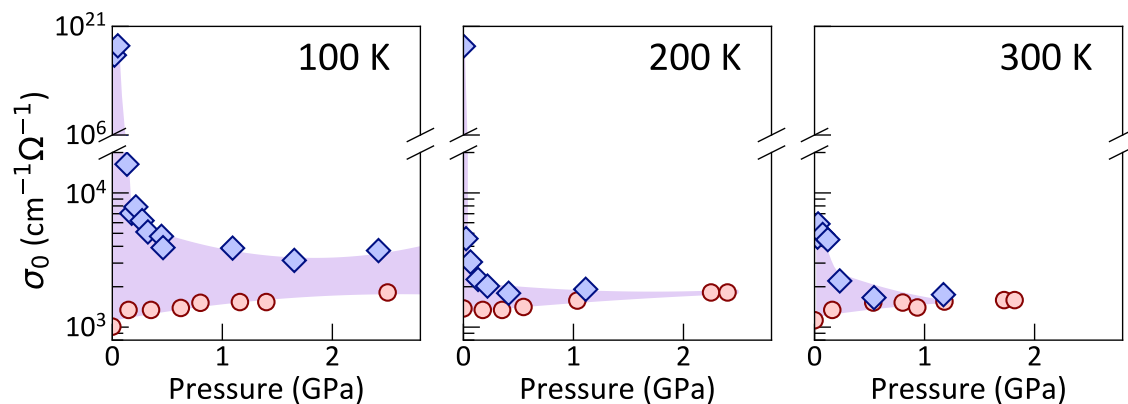


Figure 3.9: Dependence of the DC conductivity (σ_0) on applied hydrostatic pressure measured in equilibrium (red circles) and 1 ps after photo-excitation (blue diamonds), at three base temperatures. Pink shading highlights the photo-induced enhancement in conductivity. σ_0 is determined by extrapolating a Drude-Lorentz fit to the THz-frequency optical properties to zero frequency. An excitation fluence of 3 mJcm^{-2} was used. Data taken from [88].

Lorentz fit to the transient optical properties measured after photo-excitation under different applied pressures at base temperatures of 100 K, 200 K and 300 K in blue

diamonds. Two regimes appear in which different behaviour is observed. For low pressures (up to ~ 0.5 GPa) there is a sharp drop in σ_0 with increasing pressure, whereas for higher pressures σ_0 increases slightly.

The authors also extracted σ_0 from the equilibrium optical properties measured across a similar range of pressures, and this data is plotted as red circles on the same graph. In the low pressure regime, the equilibrium conductivity increases with pressure, in contrast to the photo-excited conductivity. For higher pressures the trend is similar to the photo-excited conductivity, showing a gradual increase up to the maximum measured pressure.

The similar pressure dependence of both the metallic equilibrium carriers and the charge carriers in the photo-excited state at higher pressures ($P > \sim 0.5$ GPa) suggests that in this regime any potential photo-induced superconductivity is completely suppressed.

In the low-pressure regime, the contrast in pressure-dependent behaviour between the charge carriers in the photo-excited state and the metallic charge carriers present in equilibrium provides additional evidence that the photo-excited state at ambient pressure is not simply metallic in nature. Furthermore, the inverse dependence of the photo-excited conductivity on pressure is in agreement with what one would naively expect for a photo-induced superconductor, as equilibrium superconductivity is also suppressed by the application of pressure in this compound.

Perhaps most tantalisingly, the observed decrease in σ_0 for increasing pressure persists up to room temperature, far above the maximum temperature for which photo-

induced superconductivity was reported in the previous work [5]. This suggests that the photo-excited states reported in that work at higher temperatures and shown here in figure 3.7, which were originally interpreted as enhanced-mobility metals, are actually not only metallic in nature, and perhaps would be more appropriately interpreted in terms of a two-fluid picture in which some superfluid is induced, contributing to the enhanced σ_2 and negative pressure dependence of the extrapolated conductivity, but also a portion of the normal metallic carriers remain giving rise to a finite σ_1 and accompanying $R < 1$.

More evidence in favour of this two-fluid interpretation has emerged recently in a new study in which thin films of K_3C_{60} were grown via molecular beam epitaxy into a wave-guide which also incorporated photo-conductive switches arranged in the geometry shown in figure 3.10a [90]. These photo-conductive switches are insulating in equilibrium but briefly become conductive after illumination with a pulse of visible light. By applying a voltage bias to the first switch and then exciting it with a laser pulse (the ‘launching’ pulse, illustrated in blue) a current pulse is launched into the wave-guide and sent towards the sample. The two unbiased switches placed before and after the sample were then used to measure the incident and transmitted current pulses respectively, by exciting them with further laser pulses (also shown in blue) and controlling the time-delay relative to the launching pulse. By taking the ratio between the incident and transmitted current pulses, the impedance of the sample could be determined in the frequency range down from 1 THz to 50 GHz, far below the regime which was previously measured using THz-TDS. The authors could control the strength of the probing current pulses by adjusting the size of the bias voltage applied to the launching switch. This enabled the non-linear dependence of the impedance on the current density to be measured. Finally, a $7\ \mu\text{m}$ -wavelength

mid-infrared pump pulse (shown in red) was used to photo-excite the sample, enabling all properties to be measured in both the equilibrium and photo-excited states.

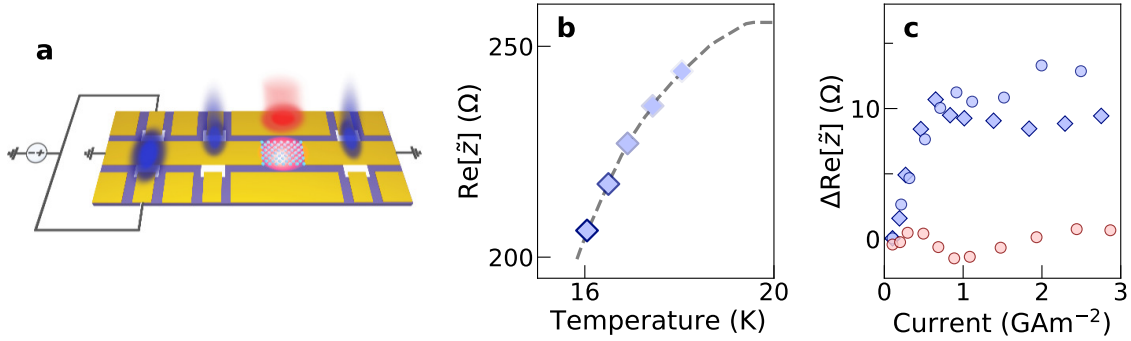


Figure 3.10: **a** Schematic illustration of the on-chip experimental geometry. A thin-film of K_3C_{60} (blue balls) is grown into a wave-guide and illuminated with mid-IR pulses (red). A visible laser pulse (blue) is used to launch a current pulse along the wave-guide by triggering the left-most photo-conductive switch, which is biased. Subsequently the second and third switches are triggered by further pulses in order to measure the current pulse before and after propagation through the sample. **b** The real part of the complex impedance measured 5 ps after photo-excitation at a base temperature of 25 K, shown together with the equilibrium R-T curve (grey dashed line). The data points with sequentially lower impedance were measured with excitation fluences of 0.2, 0.5, 1, 2 and 4 mJcm^{-2} respectively. **c** The change in the real part of the complex impedance relative to the value measured with low probing current, as a function of probing current density for equilibrium at 25 K (red circles) and 16 K (blue circles) and 5 ps after photo-excitation with a fluence of 4 mJcm^{-2} . The current-induced non-linearity in the photo-excited state matches that of the equilibrium state at 16 K. Data and schematic taken from [90].

The authors found that as the mid-infrared excitation fluence increases, the real part of the impedance of the photo-excited state drops, saturating when the pump fluence reaches 4 mJcm^{-2} at the value measured at 16 K in the equilibrium superconducting state.

Analogously to the situation which arose previously in the optical measurements where the THz optical properties provided necessary but not sufficient evidence of superconductivity, the drop in resistance observed here is consistent with the idea of photo-induced superconductivity, but does not conclusively rule out more mundane interpretations related to enhanced-mobility metallic transport. Whereas previously pressure was used to distinguish between the metallic and superconducting scenarios, in this case the authors were able to study the non-linear current dependence of the photo-excited state properties. As superconductors exhibit a critical-current effect whereby large currents result in the destruction of superconductivity, if the photo-excited state hosts superconducting-like carriers then it should be expected that the measured impedance of the photo-excited state increases as the probing current increases. The data shows that this is indeed the case, with the non-linearity also quantitatively matching the non-linearity of the equilibrium 16 K state.

Meanwhile, the development of higher-power mid-infrared light sources [123] has enabled the response of the sample to more intense driving to be studied. These new sources enabled the effect of driving fluences up to 53 mJcm^{-2} to be studied [89], more than 20x higher than the maximum of 2.3 mJcm^{-2} which was reached in the original work [5].

Figure 3.11 shows that upon photo-excitation in this newly-accessible high fluence regime at a base temperature of 100 K, the same superconducting-like optical properties observed previously re-emerge, but now persist for much longer times - up to several nanoseconds after photo-excitation. This long lifetime raises the possibility that driving with MHz repetition rate sources could enable continuous operation

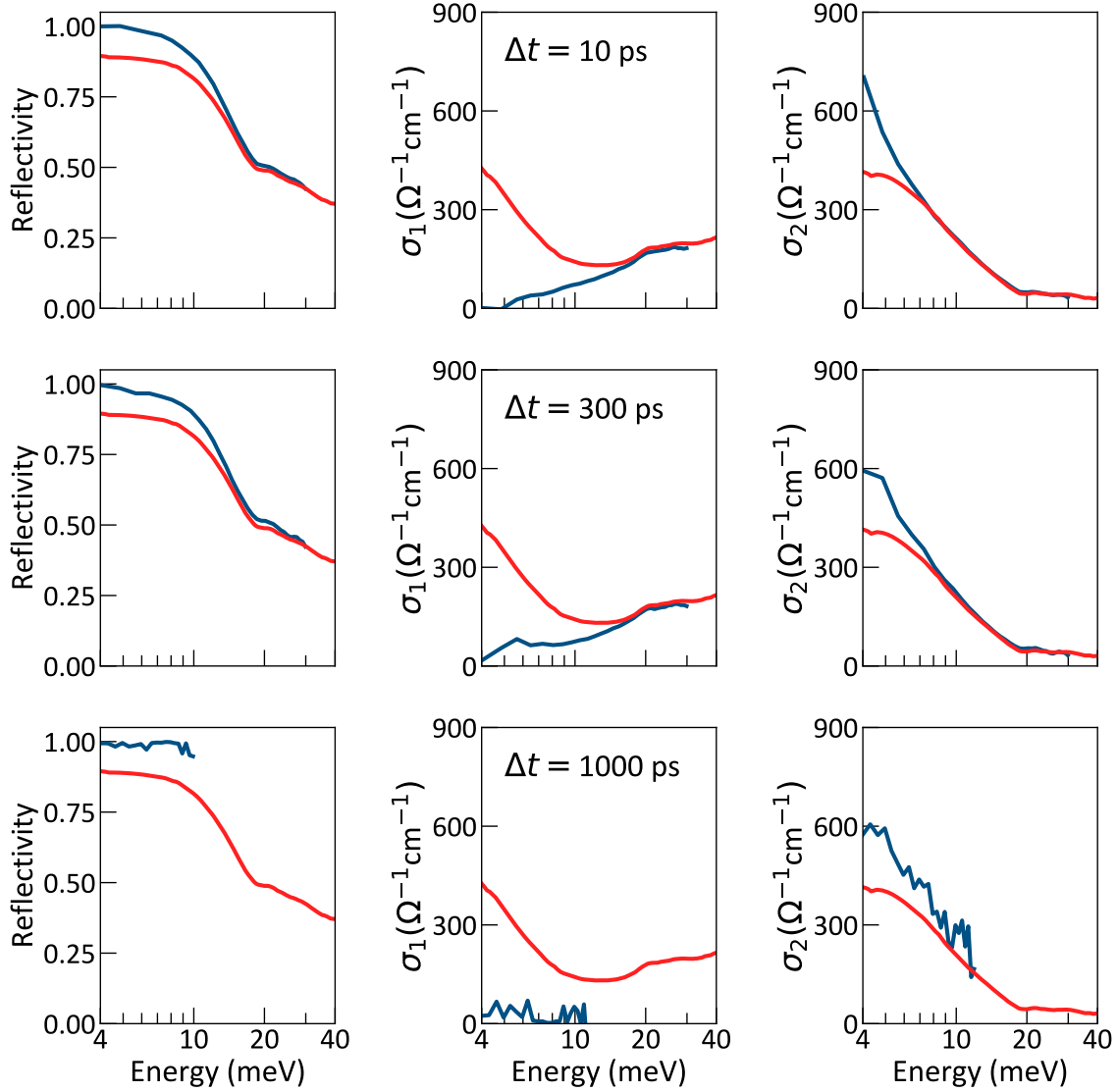


Figure 3.11: Reflectivity, real (σ_1) and imaginary (σ_2) parts of the optical conductivity measured in equilibrium (red) and at time delays Δt after the end of the photo-excitation pulse (blue), with the values indicated in the central panels, at a base temperature of 100 K. The data measured at 10 ps and 300 ps was photo-excited with 1 ps-duration $7.3 \mu\text{m}$ wavelength pulses with a fluence of 18 mJcm^{-2} , whereas the 1000 ps data used a 53 mJcm^{-2} excitation fluence with a pulse duration of 300 ps centered at $10.6 \mu\text{m}$ wavelength. Data taken from [89].

of the superconducting-like state. However, a more efficient excitation protocol is still required as the high average power of such a source with these fluences would damage the sample via heating.

More immediately, the longer lifetime associated with the higher fluence driving regime enabled an attempt to further characterize the photo-excited state using electronic transport techniques which operate at frequencies much lower than the inverse life-time of the previously-studied low fluence ps-timescale effect. In the same paper, the authors embedded a pellet of K_3C_{60} into a microstrip transmission line connected to two gold contacts at opposite ends of the sample. They then used the gold contacts to monitor the change in resistance of the sample after photo-excitation, and whilst their measurement contained a large systematic error associated with the subtraction of the contact resistance, they observed a drop to zero resistance which persisted for several nanoseconds after the sample was illuminated with a 75 ps-duration pulse with a fluence of 25 mJcm^{-2} .

Returning to the THz-TDS probing technique, the short time-scale response of the sample to driving with high-fluence pulses was studied in [91], where amplification of the THz probe light (resulting in a reconstructed surface reflectivity greater than 1) was observed at the peak of the pump-probe response. Furthermore, by varying the duration of the pump pulses whilst maintaining a constant integrated fluence, the authors could demonstrate that the size of the amplification is dependent on the peak (as opposed to time-averaged) intensity of the pump pulse.

The non-equilibrium reflectivity spectra for two pump pulse durations are shown in figure 3.12, where for the shorter pulse duration (0.1 ps) amplification is observed, as

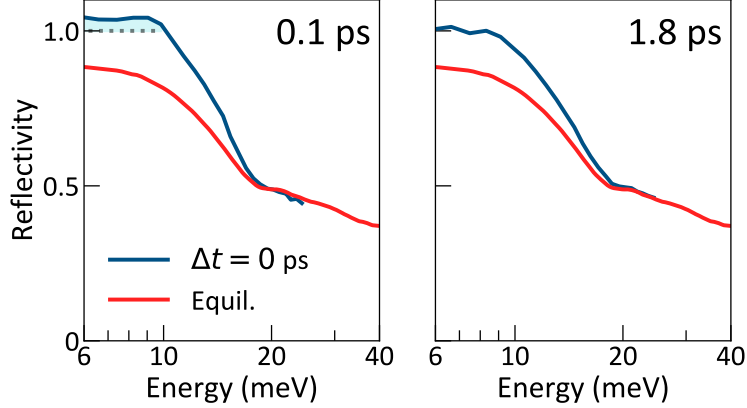


Figure 3.12: Frequency-resolved reflectivity measured at the peak of the pump-probe response in time, following excitation with pulses of duration 0.1 ps (left) and 1.8 ps (right) at a base temperature of 100 K with fluence 4.5 mJcm^{-2} . The region in which the reflectivity is larger than 1, corresponding to amplification of the THz probe light is shaded in light blue. Data taken from [91].

highlighted by the blue shaded area. In contrast, excitation with the same fluence but a stretched pulse duration of 1.8 ps does not result in amplification.

To summarize the experimental observations detailed in this chapter, when excited by high-fluence mid-infrared pulses at temperatures far above T_c , K_3C_{60} exhibits a long-lived (up to nanosecond lifetime) superconducting-like state, as evidenced by its THz-frequency optical properties. These optical properties also exhibit a pressure dependence suggestive of superconducting-like (as opposed to metallic) charge carriers, and experiments on thin-films have shown a non-linear current dependence which is also consistent with superconducting-like carriers for several ps after photo-excitation at 25 K. Finally, the sample can amplify THz light for a brief time after photo-excitation with a sufficiently intense pulse, presumably as a consequence of dynamical effects relating to the formation of the superconducting-like state.

To date, attempts to develop theoretical models which accurately capture the phenomena described here have been based on a wide variety of hypotheses. In the original work [5], it was noted that the excitation frequency is near to resonance with two infra-red active vibrational modes of the C_{60} molecules. Two possible mechanisms for how resonant driving of one of these modes could alter the electronic properties and induce superconductivity were presented.

Firstly, it was argued based on group theory analysis that the T_{1u} modes should be coupled to the H_g raman modes, which are involved in the dynamical Jahn-Teller effect thought to be responsible for the equilibrium superconducting pairing mechanism, via a coupling term proportional to $Q_{T_{1u}}^2 Q_{H_g}$ in the Hamiltonian, exactly the type of coupling which is described in figure 1.1. Here, $Q_{T_{1u}}$ and Q_{H_g} are coordinates representing the displacement of the crystal along the T_{1u} and H_g mode vectors, respectively. This would mean that by exciting the T_{1u} modes directly, the H_g modes may also be displaced [21], possibly creating a transient structure which is more conducive to pairing.

Secondly, the T_{1u} modes themselves are expected to modulate the energy levels of the three t_{1u} molecular orbitals (which are at the fermi energy). A displacement along a T_{1u} coordinate lowers the energies of two orbitals relative to the third, resulting in a configuration which also favours the formation of a spin singlet and possibly therefore also favours superconductivity.

Turning away from phononic excitations, a theory has been proposed which purportedly explains both the existence of the broad mid-infrared peak centered at

55 meV in σ_1 and draws a connection between this peak and the observed light-induced superconducting-like properties [124]. Here it is argued that the Jahn-Teller distortion brings the lowest energy term in the LUMO+1 manifold to within 55 meV of the ground state. Excitations of the quasiparticles into this orbital would result in the formation of localized excitons. If the remaining quasiparticles thermalize on a faster timescale than the relaxation from the excitonic state back to the ground state, then the remaining quasiparticles will thermalize and reach a lower effective temperature, potentially resulting in the emergence of superconductivity provided that the effective cooling is powerful enough to lower the effective temperature below T_c . The cooling mechanism itself is very similar to the concept of evaporative cooling, whilst the idea of sweeping away high-energy quasiparticles to enhance superconductivity is somewhat analogous to the microwave-enhancement of T_c observed in much earlier experiments.

One caveat related to this proposal is that the excitation required to generate the localized excitons of this type is expected to be forbidden by selection rules. However, if the absorption of light is accompanied by either the absorption or emission of a paramagnon (which is feasible due to the proximity of an antiferromagnetic phase), or if inversion symmetry is somehow broken in the crystal (potentially due to orientational ordering of the C_{60} molecules), then the transition would be allowed.

Various other theoretical mechanisms have been proposed [125–131], however the list of experimental observations relating to this phenomenon made to date (and summarized in this chapter) is not sufficient to either confirm or exclude many of these proposals. In particular, the dominant excitation which causes this effect has so far not been conclusively identified. The dependence of the effect on photo-excitation

photon energy was measured in the original work [5], and the data is shown here in figure 3.13. This measurement was restricted to photon energies in the range 80 - 200 meV, and within this range no great variation of the size of the response was discovered.

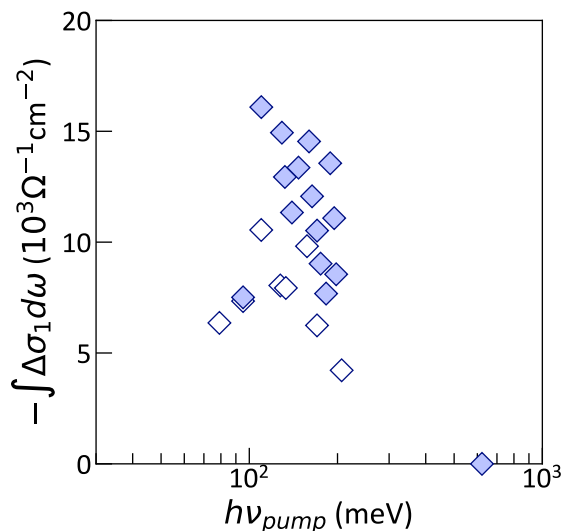


Figure 3.13: Variation of the loss in spectral weight of the real part of the optical conductivity, integrated from 0.75 to 2.5 THz. This data was measured close to the peak of the pump-probe response in time, with a base temperature of 25 K. The filled and open data points were measured with fluences of 1.1 and 0.4 mJcm^{-2} respectively. The data in this figure is taken from [5].

In chapter 4, new data is presented which extends this measurement to lower pump photon energies, and identifies an energy scale of approximately 40 meV for the dominant excitation - providing a key benchmark against which previous theoretical proposals can be tested, and informing all future attempts to model the underlying physics of this phenomenon [132].

Chapter 4

Resonant Enhancement of Light Induced Superconductivity in K_3C_{60}

4.1 High-Field Far to Mid-IR Pulse Generation

Many of the experiments reviewed so far in this thesis have highlighted the efficacy of mid-infrared photo-excitation as a means to controlling the functional properties of quantum materials. The relevance of this energy scale is due mostly to the presence of phonon modes, which enable efficient manipulation of the crystal structure when driven resonantly. However, until recently generation of strong-field pulses at frequencies lower than approximately 16 THz was largely prohibited, excluding many excitations in most candidate materials from being addressed. This situation was changed in 2017 with the development of a new setup based on the principle of chirped-pulse organic crystal difference frequency generation, which for the first

time enabled comprehensive tuning of the excitation frequency from 4 to 18 THz [70].

The generation of intense mid-infrared pulses is typically achieved via the down-conversion (in frequency) of a Ti:Sapphire laser amplifier. The output of the amplifier is split into two arms, one of which is focused into a piece of sapphire which generates (through a highly non-linear process known as super-continuum or white light generation) a broad spectrum. The resulting white light is then combined with the fundamental pulse (commonly referred to as the pump pulse) from the other arm in a BBO crystal. In a process known as optical parametric amplification (OPA), energy is transferred from the pump pulse to the white light, which acts as a seed for amplification. This process is actually a form of difference frequency generation (DFG) between the seed and pump beams, which therefore also results in the generation of a second beam at the output, known as the idler. The frequencies of the pump, signal and idler are related by the following equation:

$$\omega_{\text{signal}} + \omega_{\text{idler}} = \omega_{\text{pump}} \quad (4.1)$$

By adjusting the phase-matching angle of the BBO crystal, the desired frequency for amplification (and thus the frequency of the signal beam) can be selected. As the idler frequency will then be determined by equation 4.1, this effectively allows the difference frequency between the signal and idler beams to be tuned at will. For increased output power, further stages of amplification can be added with further BBO crystals, in which the seed is provided as the signal beam from the previous stage, and the pump is provided by another arm from the laser amplifier output. A schematic illustration of such an arrangement with 3 stages is shown in figure 4.1a.

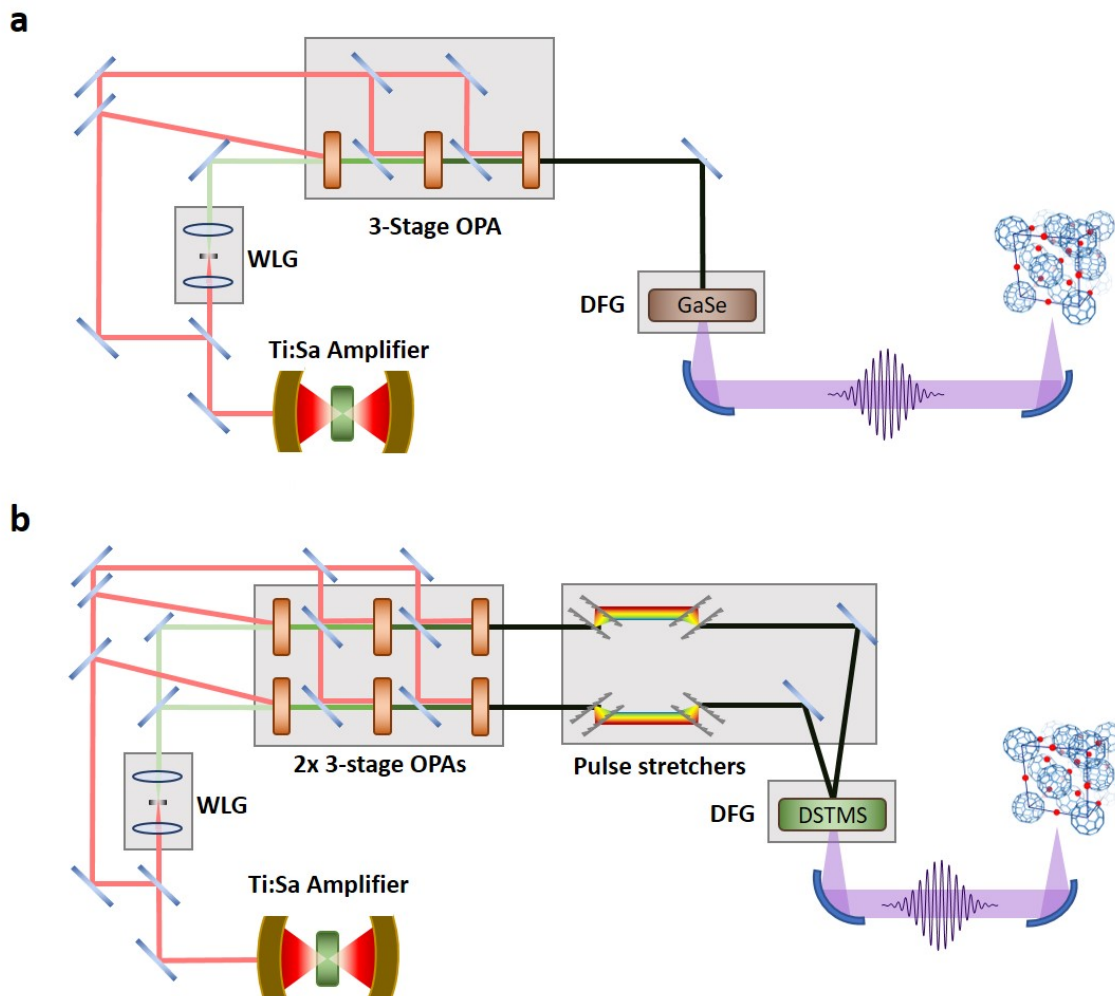


Figure 4.1: Cartoon schematics illustrating the main principles of THz-mid infrared generation via OPA+DFG. **a** A setup based on DFG between the signal and idler outputs of a single OPA in GaSe, typical of earlier studies on K_3C_{60} , capable of generating intense pulses with frequencies above 16 THz. **b** An alternative setup, in which chirped-pulse DFG of the signal beams from two phase-locked OPAs in DSTMS is used to provide intense pulses with frequencies throughout the THz-mid infrared range [70].

Mid infrared pulses can then be generated from the output of a single such OPA via DFG between the signal and idler beams in a further crystal. Alternatively, two OPAs can be used with the signal of each OPA being sent to the DFG crystal for mid-infrared generation, whilst the two idler beams are discarded. Such an arrangement requires more optics, but has the advantage that, provided both OPAs are seeded by the same white light continuum (as illustrated in figure 4.1b), the two signal beams will have the same shot-to-shot variation in carrier envelope phase. These variations then perfectly cancel in the DFG process, resulting in the generation of carrier envelope phase stable mid infrared pulses [133, 134].

Selecting a suitable crystal with which to perform the DFG process is subject to several criteria. Firstly, the selected crystal must be transparent at the wavelengths of the incoming beams and that of the desired THz frequency. Secondly, the damage threshold of the crystal must be high enough to operate with fields which provide sufficient THz output power for the intended experiment. For a given field strength, the output power will scale with the size of the second order optical non-linearity of the crystal, meaning that crystals with higher non-linearity are in general preferred [135]. Finally, the phase velocity of the generated THz field must match the phase velocity of the beat note between the two incoming beams, such that the THz waves generated in each successive layer of the crystal interfere constructively. This final condition is known as phase matching [49], and is expressed mathematically in the following equation:

$$k(\omega_{\text{THz}}) = k(\omega_1) - k(\omega_2) \quad (4.2)$$

Here ω_{THz} , ω_1 and ω_2 are the angular frequencies of the generated THz and the two incoming beams respectively, where $\omega_{\text{THz}} = \omega_1 - \omega_2$, and k refers to the frequency-

dependent wave-vector of light inside the crystal.

The length scale over which phase matching is satisfied is called the coherence length l_c , defined as:

$$l_c = \frac{\pi}{|\Delta k|} \quad (4.3)$$

where $\Delta k = k(\omega_{\text{THz}}) - (k(\omega_1) - k(\omega_2))$. For the case when equation 4.2 is perfectly satisfied, $\Delta k = 0$ and $l_c \rightarrow \infty$. In practice, for optimal DFG, l_c should be maximised and the length of the crystal in the propagation direction should match l_c as closely as possible. The coherence length can be re-written in terms of the optical properties of the DFG crystal, as $k(\omega_1) - k(\omega_2) \approx (n_g/c)\omega_{\text{THz}}$ and $k(\omega_{\text{THz}}) = (n_{\text{THz}}/c)\omega_{\text{THz}}$, where n_g is the group refractive index at frequency ω_2 , and n_{THz} is the phase refractive index at frequency ω_{THz} , giving:

$$l_c = \frac{\pi c}{\omega_{\text{THz}}|n_{\text{THz}} - n_g|} \quad (4.4)$$

Equation 4.4 highlights the important condition that for effective DFG, the group velocity of the incoming beams must match as closely as possible the phase velocity of the desired THz frequency [135].

One crystal which satisfies all of these conditions is GaSe, which has been routinely used to generate mid-infrared pulses with frequencies higher than approximately 16 THz (corresponding to wavelengths shorter than 17 μm) [133]. Indeed, in all of the previous experiments on light-induced superconductivity in K_3C_{60} which were described in section 3.2, mid-infrared pulses were generated via DFG in a GaSe crystal between the signal and idler beams of a single OPA. The only exception was

the case of [89], where a CO₂ laser-amplifier was used to supply pulses with a fixed wavelength of 10.6 μm [123].

Unfortunately the transmission of GaSe notably drops for wavelengths longer than approximately 18 μm [136]. This means that DFG in GaSe is not a viable option for generating longer wavelengths, and hence the previous studies on light-induced superconductivity in K₃C₆₀ were restricted in the range of excitation frequencies which could be tested.

To overcome this limitation and study the effect of exciting at lower frequencies, the same setup which is described in [70] was used. Here, DSTMS is used as the DFG crystal in place of GaSe. This crystal, which is composed of large organic molecules, has a very high second order optical non-linearity and can also provide phase matching between near-infrared wavelengths (as generated by a Ti:Sapphire-pumped OPA) and THz frequencies [135]. This is illustrated in figure 4.2, which shows the group refractive index in the near-infrared region alongside the phase refractive index at THz frequencies.

Apparent from figure 4.2 is the significant dispersion of both the refractive index throughout the THz frequency range, and the group refractive index in the near-infrared. This means that in order to perform phase-matched DFG, one must be able to independently tune the frequencies of the two incoming pulses. For this, a second OPA is required, with the signal outputs of each OPA being combined in the DSTMS crystal for DFG, and the idler beams being discarded.

A further complication is the existence of a forest of narrow absorption lines cor-

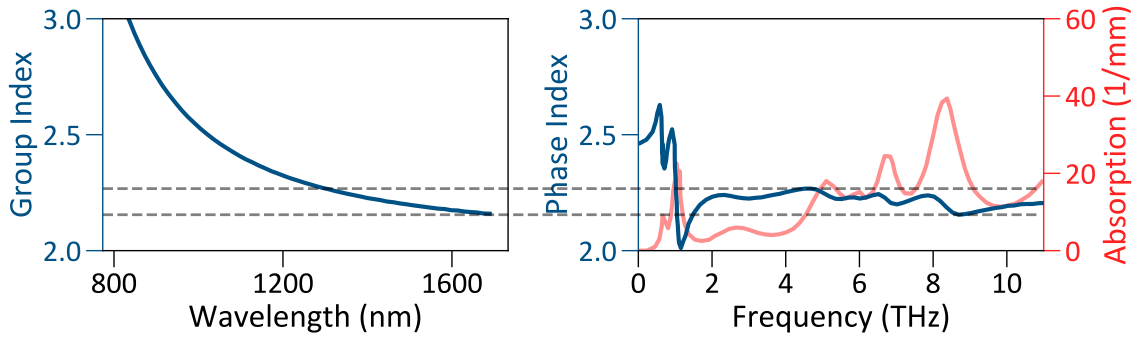


Figure 4.2: Group refractive index at NIR walevngths accessible with an OPA (left) compared to the phase refractive index at THz frequencies (right) in DSTMS. Also shown is the absorption at THz frequencies, with many narrow resonances visible. Adapted from [135].

responding to phonon resonances throughout the THz frequency range, shown in red in figure 4.2. Efficient DFG requires that the generated spectrum does not overlap significantly with any of these absorption lines, and hence independent control over the generated bandwidth is required. This bandwidth control is achieved by chirping the two signal beams prior to DFG [134]. By separating the different frequency components in time, the bandwidth of the generated pulse is suppressed, as illustrated schematically in figure 4.3. For the same reason, parasitic THz generation via unwanted optical rectification of the individual signal beams is also suppressed for bandwidths higher than the inverse pulse duration, further enhancing the efficiency of the DFG process.

With these general considerations in mind, a schematic of the optical setup is shown in figure 4.4. A Ti:Sapphire amplifier supplies 70 fs-duration 800 nm-wavelength pulses with 7 mJ of pulse energy at a 1 kHz repetition rate. After splitting off 10% of the total energy for the probe path, the remaining 90% is sent to two identical 3-stage

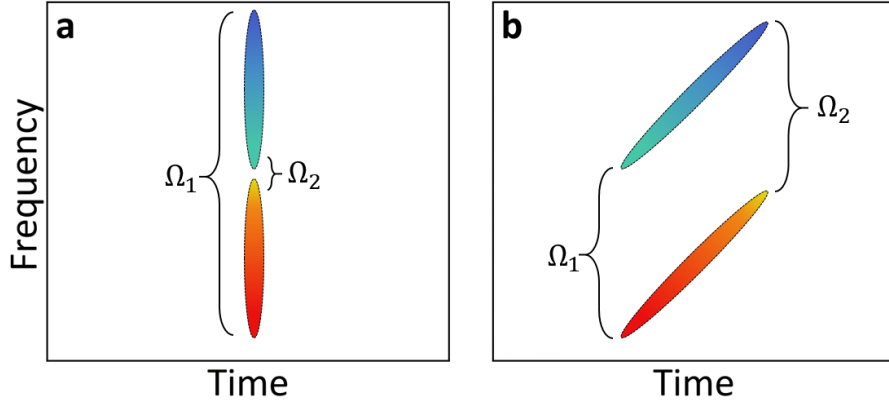


Figure 4.3: Schematic illustration of the effect of using chirped pulses on the bandwidth of the generated DFG output. **a** The case of DFG between two transform-limited pulses. **b** The case of DFG between two pulses with equal chirp. In both cases, Ω_1 and Ω_2 represent the lowest and highest frequency components of the DFG output, such that the bandwidth of the generated pulse is given by $\Omega_1 - \Omega_2$. In case **b**, $\Omega_1 \approx \Omega_2$, hence the generated pulse will have a very narrow bandwidth. This figure is adapted from [134].

OPAs, which are seeded by the same white light continuum. The signal output of each OPA is then sent through a pulse stretcher which consists of four transmission gratings. In each pulse stretcher, the spacing between transmission gratings in each pair can be controlled with a mechanical stage, providing the ability to continuously adjust the pulse duration of each individual signal beam. This provides fairly comprehensive control over the bandwidth of the generated THz pulse. An SHG-FROG device is used to measure the pulse duration of each signal beam during the alignment procedure, and for this experiment a pulse duration of 600 fs was used in every measurement.

After stretching, the two signal beams of the OPAs were sent to the DFG crystal, for which DSTMS and DAST (which have very similar properties) were used inter-

changeably according to their availability. For optimal DFG, type 0 phase matching was used, meaning that both signal beams and the generated pump beam had the same polarization. The two signal beams were combined in a non-collinear geometry with a very small angle (less than 1 degree), which was fine-tuned in order to optimize the power output for each desired pump frequency.

Large changes to the pump frequency were made by tuning the signal frequencies of the two OPAs, but smaller adjustments were also possible in situ by slightly modifying the relative delay between the two signal beams.

After generation, the pump pulses are collimated by one parabola, before being focussed onto the sample at normal incidence by a second parabola.

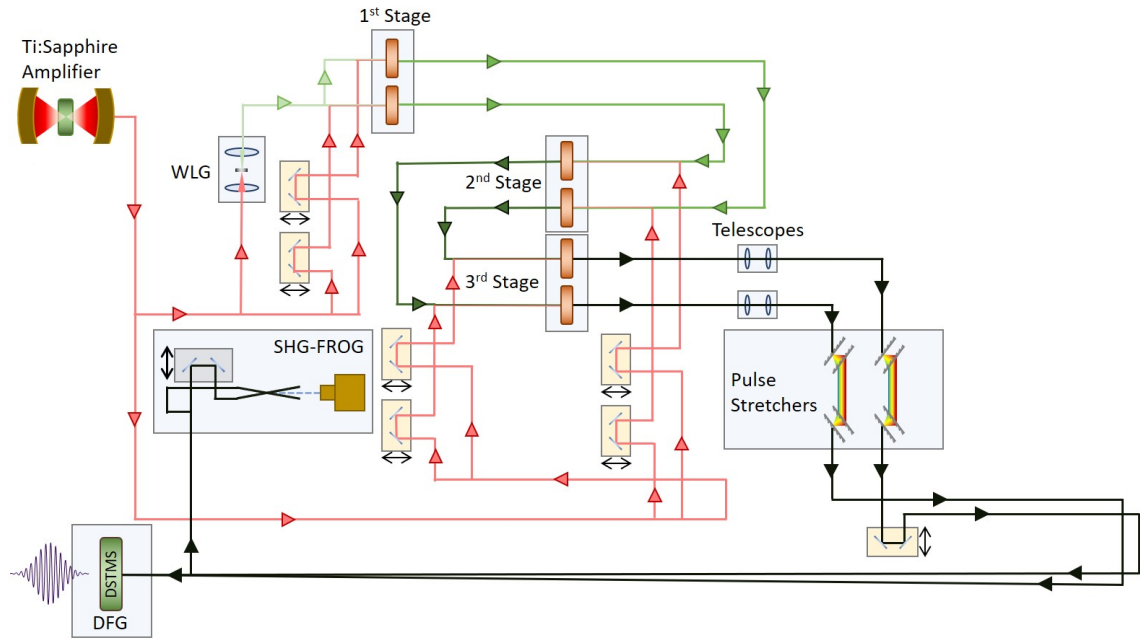


Figure 4.4: Detailed schematic of the chirped pulse-DFG based setup used to generate the excitation pulses. The Ti:Sapphire amplifier delivers 7 mJ pulses with approximate 70 fs duration at a 1 kHz repetition rate. These pulses are then used to drive two identical three-stage OPAs which are seeded by the same white light continuum, such that their mutual phases are locked. Two adjustable telescopes are located at the outputs of the two OPAs, which enable adjustment of the spot sizes on the DFG crystal further downstream. After the telescopes each beam passes through a pulse stretcher which provides continuous control of the pulse durations, which are measured using the SHG-FROG. There is an additional delay stage for controlling the mutual delay of the two pulses, which are combined in the DFG crystal over a very long working distance in order to provide fine control over their mutual angle.

4.2 Preparing K_3C_{60} for Optical Measurements

Special care is needed to prepare the sample for this experiment, as K_3C_{60} is highly-air sensitive and would be immediately destroyed upon exposure to ambient atmospheric conditions. The powder sample used in this experiment was manufactured inside a sealed ampule.

In order to perform optical measurements, we need a sample holder which presents a flat surface of sample and prevents exposure to air. For this purpose we have a copper holder which houses the sample, which must be loaded from the ampule. This preparation procedure is carried out entirely inside an Ar-filled glove box with $<0.2\text{ppm O}_2$ and H_2O . First, an indium disc with thickness 1 mm is inserted into the bottom of the copper holder. Then the ampule of K_3C_{60} is opened and the sample is poured onto the indium disc. Finally, a diamond window with $500\ \mu\text{m}$ thickness is used to press down on the sample from above whilst a specially-prepared 1 mm thick indium ring is used as a gasket to seal the sample environment from the outside atmosphere. The window is held down by a symmetric pattern of six screws which are tightened using a torque wrench to a measured torque of 12 Ncm. The entire sealed sample holder is then transferred out of the glove box and mounted on the end of a cold finger which is inserted into the optical setup.

4.3 Data Acquisition

A detailed schematic of the measurement setup is shown in figure 4.5. The mid-infrared excitation pulse impinges on the sample-diamond interface at normal incidence, whilst the THz probe pulse is focused onto the sample using a 30° off-

axis parabola and the reflection is collected and collimated using another identical parabola. The reflected electric field is then measured via electro-optic sampling by mixing with an 800 nm gating pulse in a second GaP crystal.

The pump-probe delay is fixed by setting the relative delay between the gating pulse and the mid-infrared excitation pulse. The time delay of the THz probe pulse is then scanned relative to both in order to measure the full temporal reflected electric field profile for each pump-probe delay.

All photo-induced changes in the optical properties can be extracted from the ratio of the photo-induced change in the reflected probe electric field (ΔE) to the reflected probe electric field as measured when there is no excitation pulse incident on the sample (E). In this experiment we use a differential chopping scheme to simultaneously measure both ΔE and E . The THz probe pulse and mid-infrared excitation pulses are chopped at frequencies of 500 Hz and 357 Hz respectively, whilst the 800 nm gating pulses are not chopped and so arrive with a repetition rate of 1 kHz. The THz-probe-induced change in the gating pulse is then measured by locking in to the signal at 500 Hz, whilst the mid-infrared induced modulation of this signal can be measured by locking in at 143 Hz (where $143 = 500 - 357$). Here we denote the signals measured at 500 Hz and 143 Hz as $S_{500\text{ Hz}}$ and $S_{143\text{ Hz}}$ respectively. From these signals we can extract the desired electric fields using equations 4.5 and 4.6, where α is a calibration factor which we determine experimentally.

$$\Delta E = \alpha S_{143\text{ Hz}} \quad (4.5)$$

$$E = S_{500\text{ Hz}} - \alpha S_{143\text{ Hz}} \quad (4.6)$$

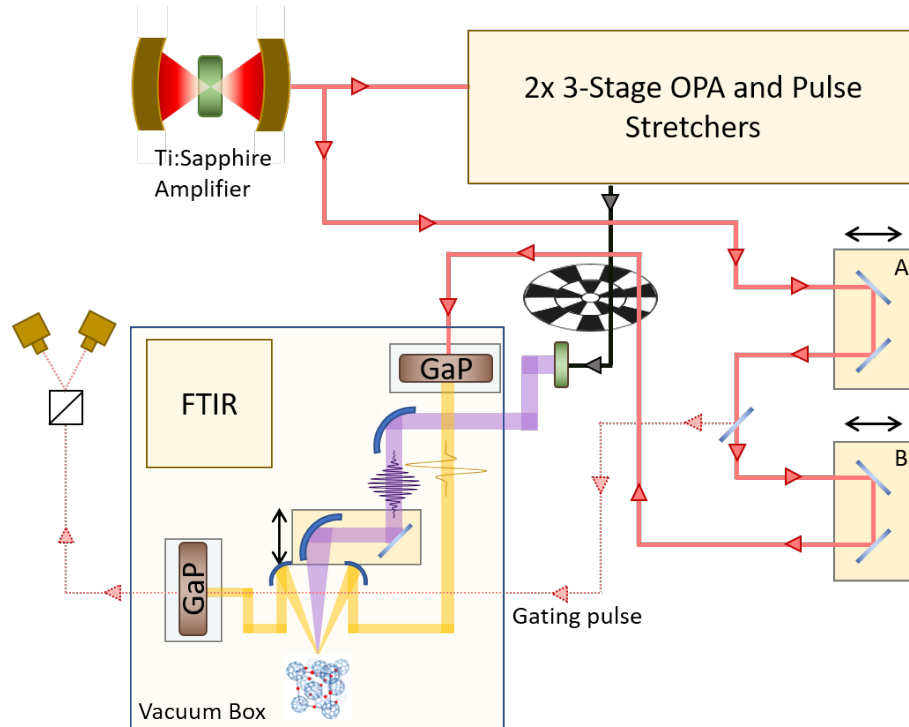


Figure 4.5: Schematic illustrating the measurement part of the setup. The output of the Ti:Sapphire amplifier is split into two arms, one of which enters the twin OPA+pulse stretcher setup (shown in detail in figure 4.4) in order to generate the NIR pulses (black line) which are used for chirped pulse DFG in the DSTMS crystal (green), generating the excitation pulse (purple). The second arm is split into two paths, one of which generates the THz probe pulse via optical rectification in a GaP crystal, and the other is used as the gating pulse in the second GaP crystal for detection of the THz field after reflection from the sample. The pump-probe delay is controlled by moving delay stage A, which adjusts both the gate and THz probe path lengths relative to the excitation pulse, and the reflected electric field for a fixed pump-probe delay is measured by scanning delay stage B which controls the path length of the THz probe relative to the gating pulse. The NIR pulses used to generate the excitation pulse pass through the inner wheel of the double-bladed chopper shown in black, whereas the 800 nm wavelength pulses which are used to generate the THz probe pass through the outer wheel.

The calibration constant α is determined by directly measuring the reflected electric fields when the sample is in the photo-excited state and in equilibrium, here denoted as E_{on} and E_{off} respectively. E_{off} is measured by completely blocking the mid-infrared excitation pulses, such that the sample is always in equilibrium. In this configuration $E_{\text{off}} = S_{500\text{ Hz}}$. Next, the beam block is removed and the mid-infrared is not chopped, such that every pulse impinges on the sample. In this configuration $E_{\text{on}} = S_{500\text{ Hz}}$. By performing this procedure we determined $\alpha = 3$.

4.4 Reconstructing the Optical Properties

The change in complex reflectivity due to photo-excitation (Δr) can be extracted from equation 4.7, where $\Delta E = E_{\text{on}} - E_{\text{off}}$:

$$\frac{\Delta E}{E_{\text{off}}} = \frac{\Delta r}{r_0} \quad (4.7)$$

However, in K_3C_{60} the THz probe field penetrates further into the sample than the mid-infrared excitation pulse, according to their differing equilibrium extinction depths. This means that the probe field senses an inhomogeneously excited sample volume, in which the photo-induced changes diminish with increasing depth. In order to extract the non-equilibrium optical properties at the sample surface (where the excitation is strongest) we model the sample as a multi-layer system, as illustrated in figure 4.6.

Our aim is to form an equation which relates the change in complex refractive index at the surface (here denoted as $\Delta n(z = 0)$), to the measured change in reflectivity Δr . Once $\Delta n(z = 0)$ is obtained, all of the other optical properties can

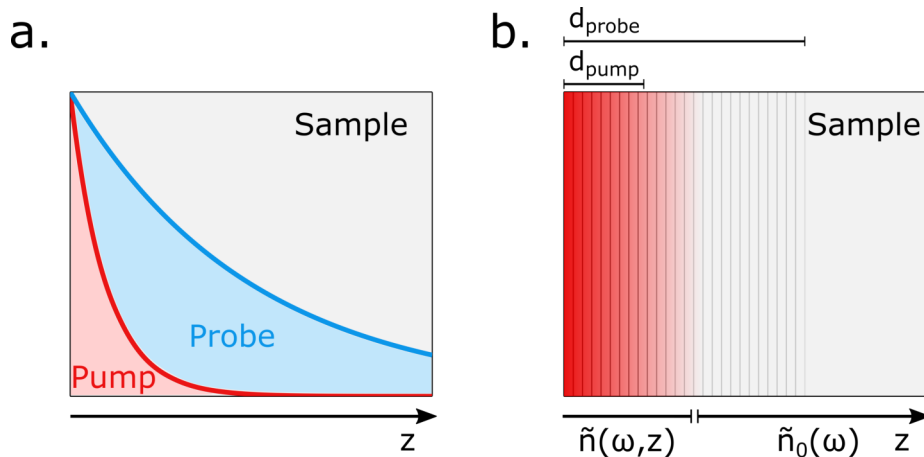


Figure 4.6: Schematic illustrations of the pump-probe penetration depth mismatch and the multilayer model. **a.** The pump and probe both penetrate with exponential intensity profiles into the sample, yet the probe penetrates further than the pump - hence interrogating an inhomogeneously excited volume. **b.** This inhomogeneously-excited volume is modelled as a stack of thin layers. By assuming a functional form for the fluence-dependence of the change in refractive index, we can extract the optical properties of the surface layer. This figure is adapted from [132]

be calculated for $z = 0$ [137]. In general, the measured change in reflectivity is a functional of the change in refractive index as a function of z : $\Delta r\{\Delta n(z)\}$. In order to form an equation that we can solve for $\Delta n(z = 0)$, we need to write $\Delta n(z)$ as a function of only $\Delta n(z = 0)$, which will then enable us to write an expression of the form $\Delta r(\Delta n(z = 0))$. This function can then be substituted into the right hand side of equation 4.7, thus relating the change in refractive index at the surface to the total change in electric field, which we directly measure. To do this we must assume a functional form for $\Delta n(z)$, how the photo-induced change in refractive index scales with depth.

In this work we will consider three approaches to this problem. The first two (here

referred to as ‘exponential models’) involve simply assuming that the pump penetrates exponentially into the sample according to its equilibrium extinction depth (as measured in linear spectroscopy). The third model (proposed by [138]) attempts to account for potential distortions of the photo-induced conductivity profile which could arise if the effect of photoexcitation saturates with fluence by introducing an additional fitting parameter.

4.4.1 Exponential Models

The assumption that the pump penetrates exponentially with its equilibrium penetration depth (d) gives the following equation for the profile of the excitation intensity $I(z)$:

$$I(z) = I_0 e^{-\frac{z}{d}} \quad (4.8)$$

where $I_0 = I|_{z=0}$. In order to arrive at a functional form for $\Delta n(z)$ we now need to supplement this with an additional assumption for the form of the dependence of the changes in the optical properties on excitation intensity. We will analyse the data using two alternative assumptions, and later compare how the chosen assumption affects the reconstructed optical properties of the surface layer:

$$\Delta n \propto I \quad (4.9a)$$

$$\Delta n \propto \sqrt{I} \quad (4.9b)$$

The first choice of assumption (equation 4.9a) is that the change in refractive index scales linearly with the excitation intensity. This assumption was chosen in all previous THz time-domain spectroscopy-based studies of photo-induced superconductivity in K_3C_{60} described in section 3.2, so must be included here in order to

enable comparison.

The second choice of assumption (equation 4.9b) is similar to the first, but with a square root replacing the linear dependence on intensity. This would be the correct assumption if the change in refractive index scales linearly with the electric field of the excitation pulse.

By inserting equation 4.8 into equations 4.9a and 4.9b we obtain the desired expression for the depth-dependent refractive index which depends only on the value $\Delta n(z = 0)$:

$$\Delta n(z) = \Delta n(z = 0)e^{-\frac{z}{d}} \quad (4.10a)$$

$$\Delta n(z) = \Delta n(z = 0)e^{-\frac{z}{2d}} \quad (4.10b)$$

Finally we can enter either expression 4.10a or 4.10b into 4.7, which now effectively takes the following form:

$$\frac{\Delta E}{E_{\text{off}}} = \frac{\Delta r[\Delta n(z = 0)]}{r_0} \quad (4.11)$$

The right hand side of equation 4.11 now only depends on the change in optical properties in the surface layer, with the choice of square-root or linear model effectively amounting to a difference of a factor of 2 in the penetration depth of the pump.

In practice, we numerically solve equation 4.11 by minimizing the following function, where Δr is calculated from the multi-layer model using a transfer matrix method:

$$\left| \frac{\Delta E}{E_{\text{off}}} - \frac{\Delta r[\Delta n(z = 0)]}{r_0} \right| \quad (4.12)$$

This optimization procedure is performed iteratively, with the THz probe penetration depth being recalculated in each iteration.

4.4.2 Saturating Model

An alternative and slightly more complicated approach, proposed in [138], is to experimentally measure and fit the fluence dependence of ΔE . For this model we cast the equations in terms of $\Delta\sigma$ (the change in conductivity), instead of Δn , for the sake of maintaining consistency with [138].

In this model, the fluence dependence is assumed to have the following functional form, where I_{sat} is a parameter which represents the intensity at which the change in conductivity saturates, determined experimentally by fitting the measured fluence-dependent data:

$$\Delta\sigma \propto \frac{I/I_{sat}}{1 + I/I_{sat}} \quad (4.13)$$

This assumption gives the following depth profile for the change in conductivity:

$$\Delta\sigma(z) = \Delta\sigma(z=0) \frac{1 + I(0)/I_{sat}}{I(0)/I_{sat}} \frac{I(z)/I_{sat}}{1 + I(z)/I_{sat}} \quad (4.14)$$

where $I(z)$ is again assumed to decay according to the equilibrium extinction depth, $I(z) = I_0 e^{-\frac{z}{d}}$.

As with the exponential models, we can now obtain the photoexcited optical properties at the surface by iteratively minimizing the function in equation 4.12 (after replacing $\Delta n(z=0)$ with $\Delta\sigma(z=0)$).

4.5 Resonantly Enhanced Photosusceptibility

The effect of photo-excitation with pulses of 41 meV photon energy ($\lambda \approx 30 \mu\text{m}$, $f \approx 10 \text{ THz}$) above T_c was studied. Reconstructing the reflectivity and optical conductivity from the raw changes in the THz probe electric field, measured in this case at a base temperature of 100 K, without attempting to account for the mismatch in penetration depth between the excitation and probe pulses (discussed in section 4.4) results in the spectra shown in figure 4.7. Although this data represents an underestimation of the photo-induced changes at the surface of the sample, the signatures of photo-induced superconductivity are already seen to emerge, with a loss of spectral weight in σ_1 accompanied by a corresponding enhancement in σ_2 . Interestingly, at the earliest time delay, the raw pump-probe signal saturates below the maximum fluence measured here, with the saturation value corresponding to a reflectivity which is almost perfectly 1. Such a saturating fluence regime could not be reached for later time delays.

The results of using the three models described in section 4.4 to estimate the optical properties of the photo-excited state at the sample surface are shown in figure 4.8, both for the same raw data measured at a base temperature of 100 K shown in figure 4.7, and for further measurements which were carried out at room temperature. All three reconstruction models give very similar estimates of the surface layer optical properties, with the main differences being slight quantitative adjustments to the amount of surviving spectral weight in σ_1 , and correspondingly the level of deviation in the reflectivity from a perfect value of 1. In all cases, σ_2 is observed to diverge at low frequencies, as would be expected for a superconductor.

For all the spectra shown in figure 4.8, the excitation fluence was just 0.4 mJcm^{-2} . These spectra are very similar to those reported previously and shown throughout chapter 3.2 for higher-frequency photo-excitation, but are now manifested on metastable time scales and up to room temperature despite an almost two orders of magnitude weaker excitation fluence.

In order to map out the time evolution of the system after photo-excitation we define three figures of merit, extracted from the snapshots of $R(\omega, \tau)$, $\sigma_1(\omega, \tau)$ and $\sigma_2(\omega, \tau)$ for each pump-probe time delay τ . The first two quantities are the frequency-averaged values of the reflectivity and $\sigma_1(\omega)$ from 5-10 meV (from here on referred to as $\langle R \rangle$ and $\langle \sigma_1 \rangle$ respectively), a frequency range which lies below the photo-induced energy gap. A zero-temperature superconductor with infinite lifetime would give values $\langle R \rangle = 1$ and $\langle \sigma_1 \rangle = 0$ respectively. Even in the presence of superconductivity, any remaining un-condensed quasi-particles will result in a Drude-like dissipative contribution to $\sigma_1(\omega)$ and, consequentially, non-perfect reflectivity at low frequencies. For this reason we fit the complex conductivity using the two-fluid model which was introduced in section 2.1.4 and use the extracted fractional super-fluid density as a third figure of merit.

The fitting function used in this procedure is given in equation 4.15, where the first two terms describe the contribution of the superconducting-like carriers, the third term is a Drude contribution arising from the remaining normal carriers and the final term is a sum of two Lorentz oscillators which are required to capture the

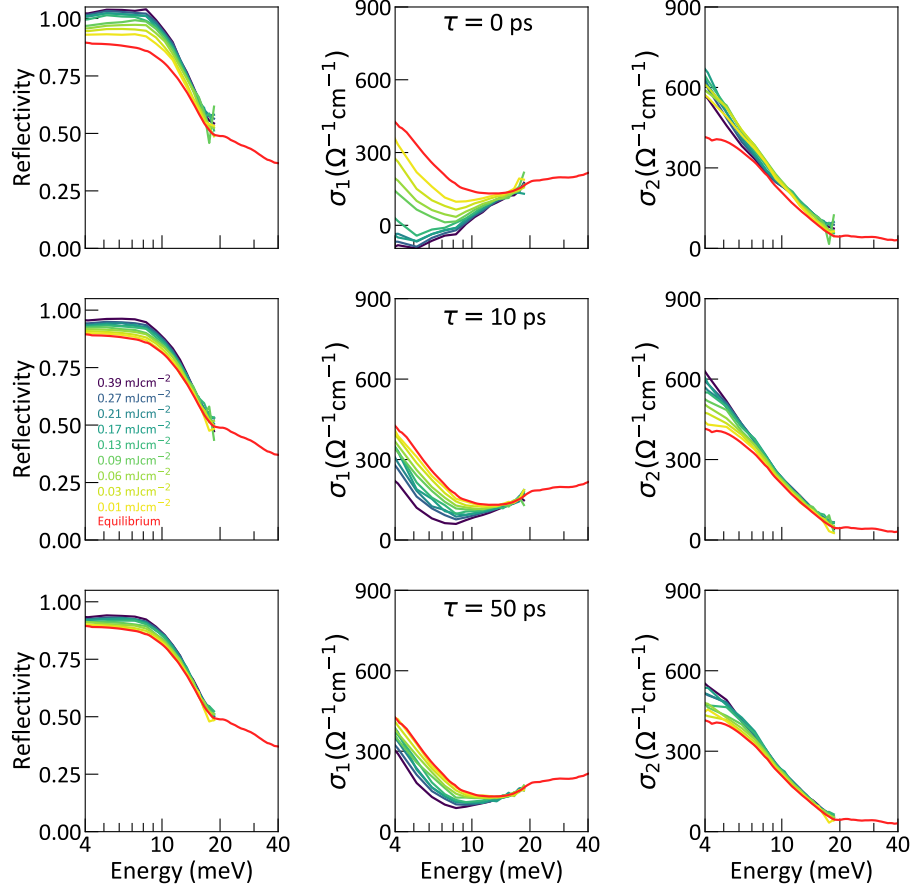


Figure 4.7: Raw changes in the optical properties after photo-excitation by a 10 THz pulse with various fluences as indicated in the figure legend, at three pump-probe time delays denoted by τ for a base temperature of 100 K. This data represents an underestimate of the photo-induced changes in the surface layer of the sample, as no reconstruction procedure attempting to account for the mismatch in penetration depth between the pump and probe pulses has been applied. This data is also reported in [132].

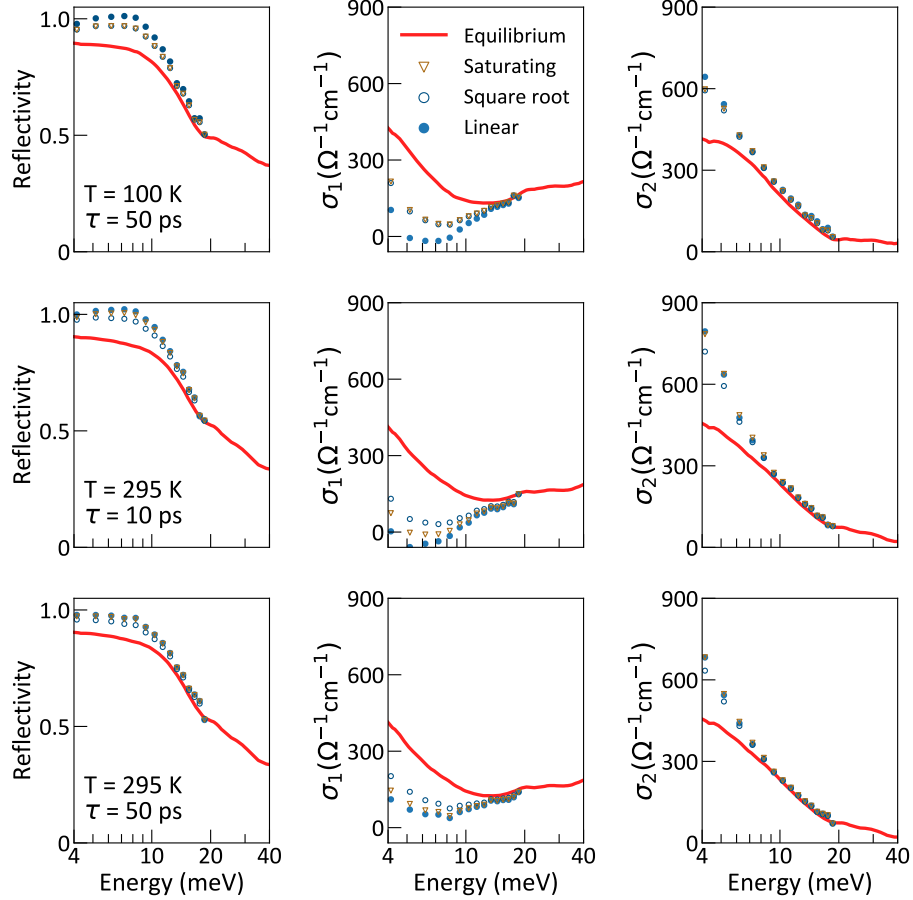


Figure 4.8: Reflectivity and real (σ_1) and imaginary (σ_2) parts of the optical conductivity measured in equilibrium after photo-excitation by a 10 THz pulse with fluence 0.4 mJcm^{-2} at the temperatures T and pump-probe time delays τ indicated in the figure. The post-photoexcitation optical properties have been reconstructed under the assumption of a saturating (brown triangles), square root (open blue circles) and linear (filled blue circles) dependence of the changes in the optical properties on excitation fluence. This data is also reported in [132].

contribution of the broad mid-infrared absorption peak.

$$\begin{aligned} \sigma(\omega, \tau) = & \frac{\pi n_{sc} e^2}{2 m} \delta(\omega = 0) + i \frac{n_{sc} e^2}{m} \frac{1}{\omega} \\ & + \frac{n_n e^2}{m} \frac{1}{\gamma_D - i\omega} \\ & + \sum_{\alpha=1}^2 \frac{B_\alpha \omega}{i(\Omega_\alpha^2 - \omega^2) + \gamma_\alpha \omega} \end{aligned} \quad (4.15)$$

All of the parameters (apart from n_n and n_{sc}) were fixed by fitting the equilibrium optical properties measured at 100 K. Then in order to fit $\sigma(\omega, \tau)$ after photo-excitation only n_n and n_{sc} were allowed to vary as free parameters. Figure 4.9 illustrates the application of this procedure to a single dataset.

By using the three figures of merit defined here, which roughly correspond to the three measured response functions, we plot the time-evolution of the system after resonant photo-excitation at a base temperature of 100 K in figure 4.10.

At early time delays the reflectivity is above 1, indicating amplification of the THz probe light. This directly corresponds to $\sigma_1(\omega)$ becoming negative, a scenario which is impossible in equilibrium due to energy conservation but becomes viable in the non-equilibrium conditions considered here because energy is being supplied via the excitation pulse. This amplification survives for approximately 5 ps, and is followed by relaxation into the superconducting-like state which then persists for much longer times (here measured up to 100 ps).

It is already clear from the presence of enhanced amplification and long-lived superconducting-like properties (despite comparatively low excitation fluence) in figure 4.10 that the

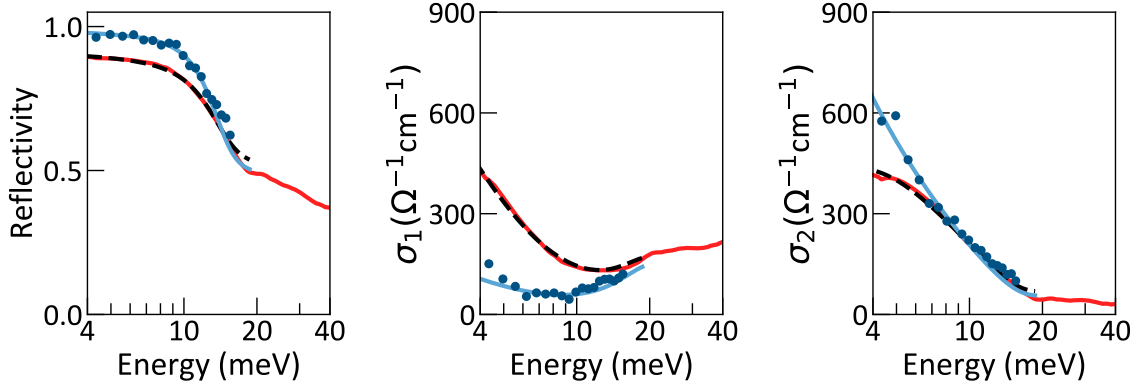


Figure 4.9: Reflectivity and real (σ_1) and imaginary (σ_2) parts of the optical conductivity measured in equilibrium at 100 K (red) and 50 ps after photo-excitation with a fluence of 0.5 mJcm^{-2} at 11 THz, reconstructed under the assumption of a square root scaling of the changes in the optical properties with excitation fluence. The fit to the equilibrium data using the model of equation 4.15 is shown as a dashed black line and gives zero superfluid density. The two-fluid fit to the transient data generated by only allowing n_{sc} and n_n to vary is shown as a solid blue line and gives a superfluid fraction $n_{sc}/n_{tot} = 73\%$. This data is also reported in [132].

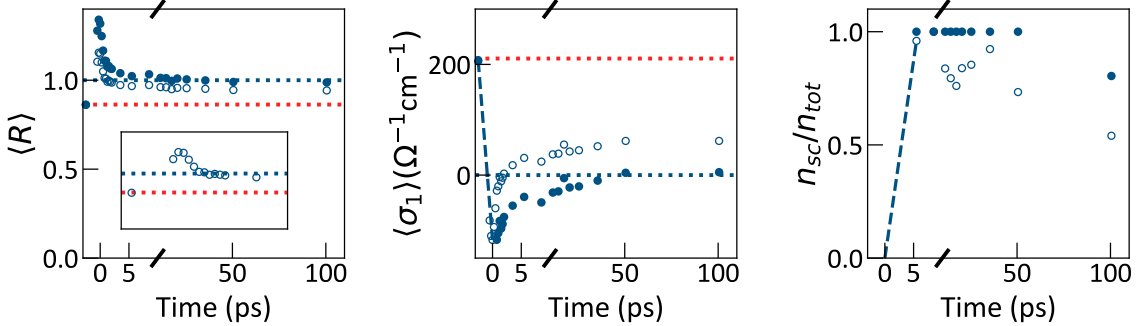


Figure 4.10: Time evolution of the optical properties. From left to right: reflectivity and σ_1 averaged in the energy range from 5-10 meV, and fractional superfluid density as determined by a two-fluid model fit using equation 4.15, following resonant photo-excitation with 0.5 mJcm^{-2} fluence at 45 meV photon energy at a base temperature of 100 K. The filled (open) blue circles show the result of reconstructing the optical properties based on the assumption of linear (square root) scaling of the changes in the optical properties with excitation fluence. This data is also reported in [132].

lower-frequency excitation pulses are much more effective than those used in previous experiments. This is quantified by figure 4.11, where the same three figures of merit which were defined above (averaged reflectivity, σ_1 and extracted superfluid density) are plotted as a function of excitation fluence for a pump-probe time delay of 10 ps for both resonant and off-resonant excitation. In both cases all three figures of merit smoothly approach their equilibrium superconducting-state values as the fluence is increased, however the fluence required is approximately 50 times less for 41 meV (10 THz) compared to 170 meV (41 THz) excitation.

We systematically studied the dependence on excitation photon energy by carrying out similar fluence-dependent measurements whilst tuning the central photon energy of the pump throughout the available range. To enable a fair comparison, the same parameters of 100 K base temperature, 4 meV excitation pulse bandwidth and 600 fs excitation pulse duration were used for all measurements. For all excitation photon energies, the qualitative nature of the photo-induced changes in the optical properties were similar to those shown in figure 4.8, although the size of the response for a given fluence differed dramatically.

In order to make a quantitative comparison between the relative efficacy of different pump photon energies, we define a new figure of merit, from here on referred to as the ‘photosusceptibility’, which can be extracted from a measurement of the fluence dependence of the loss in spectral weight in σ_1 for a given pump photon energy, integrated across the below-gap spectral region from 5 to 10 meV. This procedure is illustrated in figure 4.12 for a single pump photon energy. The fluence dependence

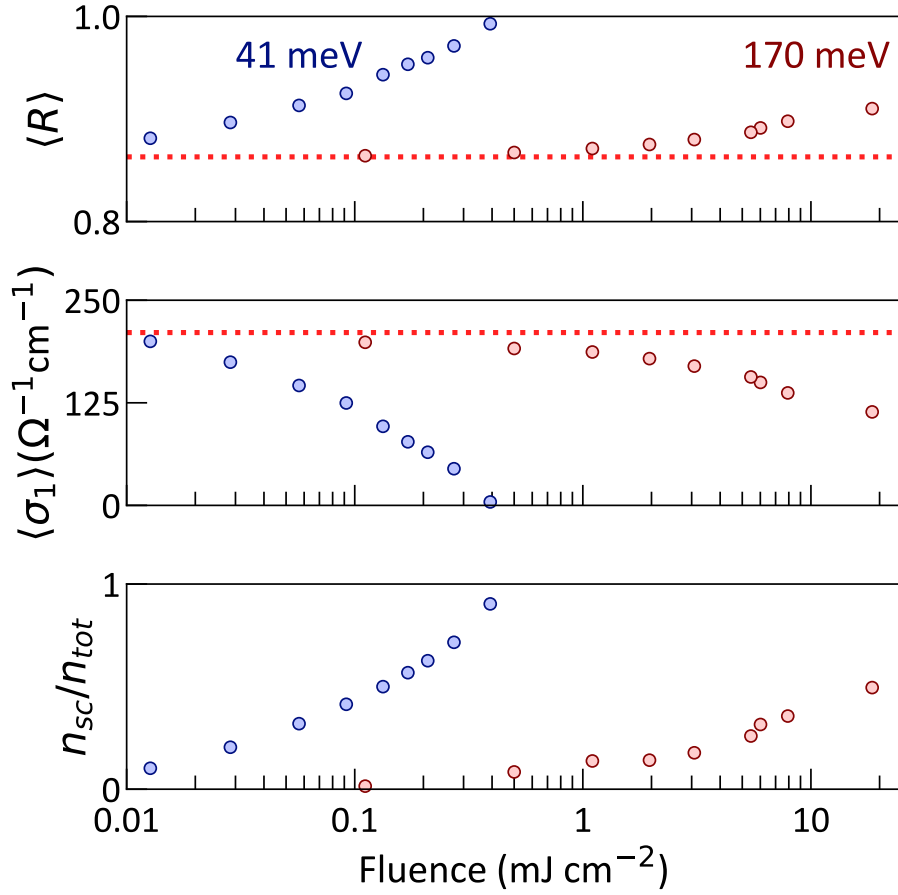


Figure 4.11: Fluence dependence of the three figures of merit for photo-induced superconductivity in K_3C_{60} , measured 10 ps after photo-excitation at a base temperature of 100 K, with excitation photon energies of 41 meV (blue symbols) and 170 meV (red symbols). From top to bottom: average reflectivity, average σ_1 (where the averages have been taken in the energy range from 5-10 meV) and fractional superfluid density as determined by a two-fluid model fit using equation 4.15. The data in this figure was reconstructed under the assumption of a square root scaling of the changes in optical properties with excitation fluence. This data is also reported in [132].

is fitted with equation 4.16:

$$\int_{5 \text{ meV}}^{10 \text{ meV}} (\sigma_1^{\text{eq}}(\omega) - \sigma_1^{\text{photo}}(\omega, F)) d\omega = A \left(\frac{1}{1 + Be^{\frac{4BF}{A}}} - \frac{1}{2} \right) \quad (4.16)$$

Here F denotes the excitation fluence and A and B are free parameters which are optimized to fit the data. The ‘photosusceptibility’ is then given by B , which is the gradient of this function at $F = 0$. This enables a reasonably fair comparison of the effect of different pump photon energies, even if the measurements are carried out in slightly different excitation fluence ranges.

The photosusceptibility is plotted as a function of excitation photon energy in figure 4.13 for both 10 ps and 50 ps pump-probe time delays. A peak centred at 41 meV (10 THz) is observed, with approximately 16 meV FWHM. This represents the empirical identification of the dominant energy scale for the formation of the photo-induced superconducting-like state, providing an important benchmark against which all theoretical hypotheses can be tested. In the section that follows the microscopic details of potentially-relevant excitations which are thought to coincide with this energy scale will be discussed.

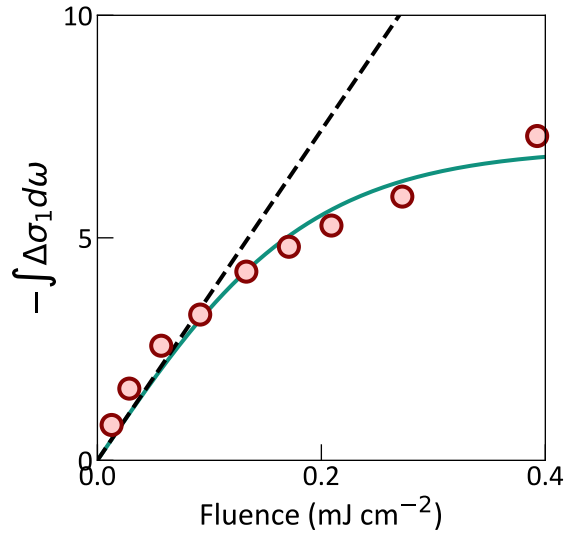


Figure 4.12: Definition of the photosusceptibility, based on the fluence dependence of the integrated loss in spectral weight of σ_1 . The spectral weight loss integrated from 5-10 meV plotted as a function of excitation fluence (red circles). This data was measured 10 ps after photo-excitation with pump photon energy centered at 41 meV at a base temperature of 100 K, and reconstructed under the assumption of a square root scaling of the changes in optical properties with excitation fluence. The green curve shows a fit using equation 4.16. The photosusceptibility is defined as the gradient of the dashed black line, which is a tangent to the fit at zero fluence. This data is also reported in [132].

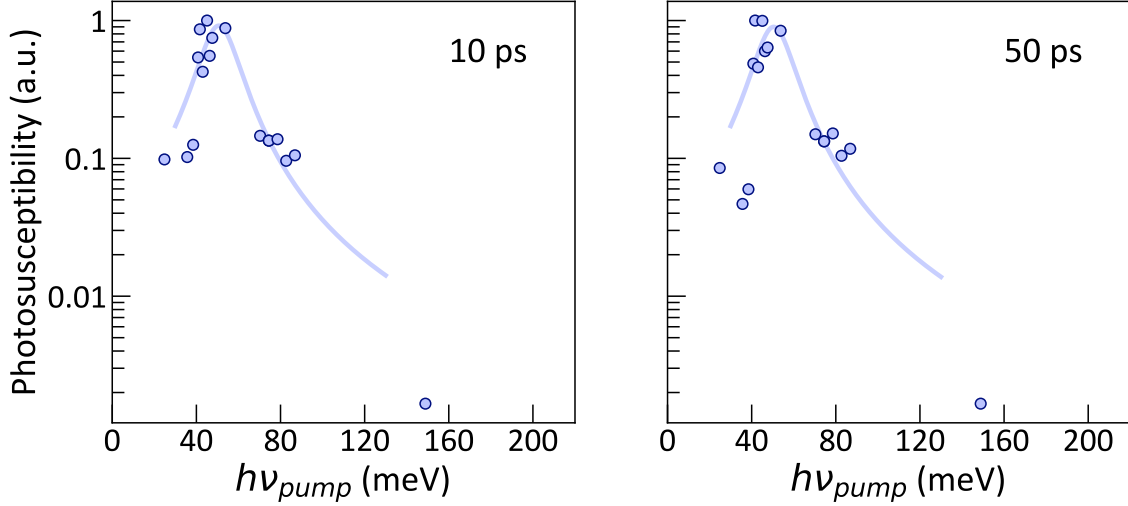


Figure 4.13: Photosusceptibility as a function of pump photon energy. The data extracted from fluence dependence measurements is represented by blue circles, measured at a pump-probe time delay of 10 ps in the left panel, and 50 ps in the right panel at a base temperature of 100 K. The optical properties from which these points were extracted were reconstructed under the assumption of a square root scaling of the photo-induced changes with excitation fluence. For each pump-probe delay, the data has been normalized such that the peak has a value of 1. The solid blue lines are guides to the eye. This data is also reported in [132].

4.6 Theoretical Discussion

Following the experimental identification of a resonance frequency for this effect close to 10 THz, it should be possible to develop more sophisticated hypotheses for the microscopic mechanism behind light-induced superconductivity by considering which excitations coincide with this energy scale, how they may couple to light and finally how driving them could favour superconductivity.

A natural starting point is to return to the evaporative cooling mechanism proposed in [124], as the broad mid-infrared absorption peak in σ_1 , attributed to the

formation of excitons which could provide an entropy sink to cool the remaining quasiparticles, correctly predicted the energy scale of the resonance observed here.

Although this avenue appears promising due to the agreement with the observed resonance frequency, some more subtle problems still need to be addressed. Firstly, if the role of light in this experiment was only to lower the effective temperature, then one would expect a photo-induced superconducting state with identical properties to the equilibrium state below T_c to arise. In practice however, the value of the gap in the light-induced state appears to be larger than that measured in equilibrium. Secondly, photo-excitation at frequencies significantly higher than the resonance should in this picture result in an effective heating of the quasi-particles. However, such an effect has never been observed in experiment despite a relatively large span of drive frequencies having now been investigated. Putting these subtleties aside, it does however seem clear that the excitation identified in [124] could be key to the formation of light-induced superconductivity, so definitely warrants further investigation.

Turning instead to phonon excitations, there is a strong peak visible in the inelastic neutron scattering spectrum (see figure 3.3) which roughly coincides with the energy scale of the resonance. In [99] this peak is assigned T_{2u} and G_u character based on the point group of a C_{60} molecule, suggesting that it is optically silent. However, it has been shown that the cubic crystal environment present in solid forms of C_{60} can result in both splitting and optical activation of such modes, making it conceivable that a mode is being driven resonantly by direct coupling to the electric field of the pump pulses.

This idea has been explored theoretically in [132] by first performing an ab initio calculation of the phonon spectrum of K_3C_{60} , which revealed 24 infra-red active modes with T_{1u} symmetry ranging in energy from 2.2 to 185.3 meV. The eigen-frequencies of these modes are listed in figure 4.14.

Frozen phonon DFT calculations have been performed to determine the effect of

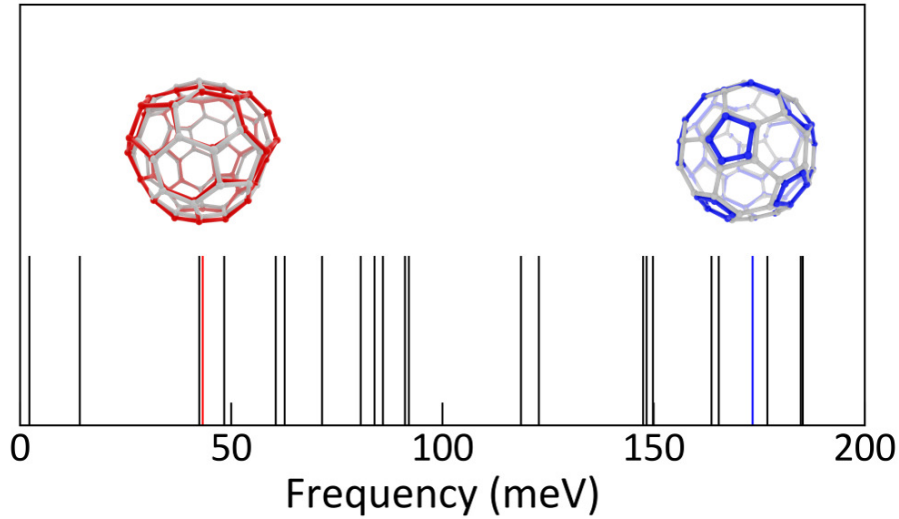


Figure 4.14: List of infrared-active vibrational mode eigen-frequencies in K_3C_{60} , calculated via a finite displacement approach [139] from [132]. Each line indicates the eigen-frequency of a distinct mode. The two inset cartoons illustrate the eigen-displacements of the modes highlighted in red and blue.

displacing these infra-red active phonon modes on the t_{1u} molecular orbitals at the Fermi energy, the results of which are summarized in figure 4.15. It was found that displacing the T_{1u} modes lifts the orbital degeneracy, causing two orbitals to lower in energy relative to the third. Similarly to the dynamical Jahn-Teller distortion which is thought to be critical to equilibrium superconductivity, such a distortion favours the formation of a spin singlet pair on each molecule. As the size of the splitting

is found to scale with the square of the distortion, even a symmetrical oscillation of the modes would lead to non-zero time-averaged splitting. Furthermore, for a given excitation fluence the strength of the induced splitting was found to be maximal when exciting with a photon energy of 43.2 meV, in good agreement with the resonance energy. This results from a combination of the mode effective charge, which determines the strength of the coupling to the excitation pulse, and the relatively low eigenfrequency, which means that for a given energy of oscillation the maximum displacement of the mode coordinate is greater compared to higher frequency modes.

An alternative approach to understanding the observed phenomena is to return to

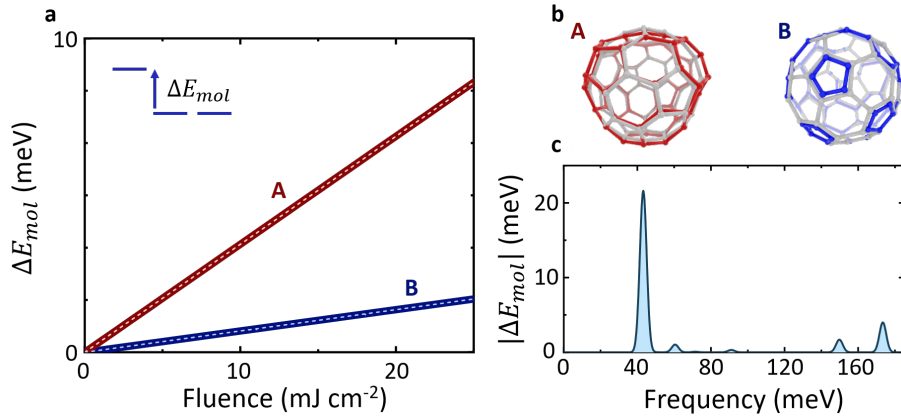


Figure 4.15: Ab initio calculations studying the effect of vibrational distortions on the t_{1u} molecular levels. **a** The induced splitting of the t_{1u} molecular levels as a function of excitation fluence, as defined by the inset. The effect of mode A is shown in red, and mode B in blue, with the eigen-displacements of the two modes shown in panel **b**. **c** The induced splitting as a function of excitation frequency for a fixed fluence, calculated by considering the full spectrum of infrared-active T_{1u} modes shown in figure 4.14. This figure is adapted from [132].

the Hamiltonian of [118–120] introduced in section 3.1 which successfully describes

the alkali-doped fulleride phase diagram in equilibrium, and consider the effect of driving at 10 THz. Here we restrict our considerations to a simplified version of this model which only considers a single molecule in which the three orbitals are occupied by three electrons. With this restriction, we choose the following basis, where the direction of the arrow (up or down) indicates the direction of the electron spin, and the position indicates the orbital which is occupied:

$$\begin{aligned} & \{ |\uparrow, \uparrow\downarrow, 0\rangle, |\uparrow, 0, \uparrow\downarrow\rangle, |\uparrow\downarrow, \uparrow, 0\rangle, |0, \uparrow, \uparrow\downarrow\rangle, |\uparrow\downarrow, 0, \uparrow\rangle, |0, \uparrow\downarrow, \uparrow\rangle, \\ & |\downarrow, \uparrow, \uparrow\rangle, |\uparrow, \downarrow, \uparrow\rangle, |\uparrow, \uparrow, \downarrow\rangle, |\uparrow, \uparrow, \uparrow\rangle \} \end{aligned} \quad (4.17)$$

Note that the equivalent states with all spins reversed have been dropped for simplicity. In this basis, the Hamiltonian illustrated in figure 3.5a can be represented by the following matrix:

$$\hat{H} - (3U_{\text{eff}} + 5J_{\text{eff}})\hat{I} = -J_{\text{eff}} \begin{bmatrix} 0 & -1 & 0 & 0 & 0 & 0 & 0 & 0 & 0 & 0 \\ -1 & 0 & 0 & 0 & 0 & 0 & 0 & 0 & 0 & 0 \\ 0 & 0 & 0 & -1 & 0 & 0 & 0 & 0 & 0 & 0 \\ 0 & 0 & -1 & 0 & 0 & 0 & 0 & 0 & 0 & 0 \\ 0 & 0 & 0 & 0 & 0 & -1 & 0 & 0 & 0 & 0 \\ 0 & 0 & 0 & 0 & -1 & 0 & 0 & 0 & 0 & 0 \\ 0 & 0 & 0 & 0 & 0 & 0 & +2 & -1 & +1 & 0 \\ 0 & 0 & 0 & 0 & 0 & 0 & -1 & +2 & -1 & 0 \\ 0 & 0 & 0 & 0 & 0 & 0 & +1 & -1 & +2 & 0 \\ 0 & 0 & 0 & 0 & 0 & 0 & 0 & 0 & 0 & +4 \end{bmatrix} \quad (4.18)$$

The inverted Hunds rules ensure that the most energetic eigenstate of this Hamiltonian is $|\uparrow, \uparrow, \uparrow\rangle$, as the formation of a spin singlet on a single molecular orbital is

always energetically favourable. In contrast, the ground state $|\psi_{\text{ground}}\rangle$ is given by:

$$|\psi_{\text{ground}}\rangle = |\uparrow\downarrow, 0, \uparrow\rangle + |0, \uparrow\downarrow, \uparrow\rangle \quad (4.19)$$

There are six such states with the same energy, given by placing the single spin, which can point either up or down, in each of the three orbitals whilst the singlet pair is de-localized over the remaining two orbitals.

Intriguingly, the energy gap to the first manifold of excited states (which is given by $2J_{\text{eff}} \approx 37 \text{ meV}$) coincides almost perfectly with the resonance frequency for light-induced superconductivity. Six of these states appear very similar to $|\psi_{\text{ground}}\rangle$, only with a minus sign replacing the plus sign in equation 4.19, as indicated in equation 4.20:

$$|\psi_{\text{excited}}\rangle = |\uparrow\downarrow, 0, \uparrow\rangle - |0, \uparrow\downarrow, \uparrow\rangle \quad (4.20)$$

At the same energy are four further states which do not include any pairs, so presumably cannot contribute to superconductivity - bringing the total degeneracy to ten. This simple observation is far from a well-developed theory of light-induced superconductivity in K_3C_{60} , but given the success of this model in explaining the equilibrium properties of the alkali-doped fullerenes, this direction of thought definitely warrants further investigation.

Among the questions which must be addressed within this framework is that of how exactly light couples into this Hamiltonian. One should also consider an extension of this model to include terms arising from driving inter-site tunneling interactions, which could be close to the same energy scale as the terms considered here due to the

distance between neighboring molecules being comparable to the size of a molecule itself.

To summarize, the identification of the resonance energy for generation of the superconducting-like state provides a key benchmark against which theoretical hypotheses can be tested, and certainly rules out many higher frequency modes which were considered in earlier works [5]. However, due to the co-existence of different excitations at this energy scale, it does not point uniquely to a specific underlying excitation. As well as the three distinct excitations discussed explicitly here (excitonic, IR-phononic and many-body), excitations of raman modes via two-photon processes at twice the drive photon energy should also be considered [140]. In fact, to form a complete theoretical depiction of the formation of the light-induced state it may be necessary to consider some or all of these fundamental excitations acting in conjunction, for example by considering the effect of a coherent T_{1u} phonon on the Hamiltonian of equation 4.18.

Ultimately, definitive progress in attempting to understand the formation of the light-induced superconducting-like state can only be provided by theoretical work in conjunction with further experiments aimed at directly measuring the dynamics which follow photo-excitation, via alternative probing techniques to those which have been carried out to-date.

Summary and Outlook

Historically, light has been used through various forms of spectroscopy to characterize material properties in equilibrium. Recent advances in laser technology which have enabled the generation of very short, intense pulses with extremely high electric fields have served to elevate light from its role as a mere spectator. There is now a concerted effort towards using light to manipulate the properties of materials, potentially enabling control on very fast timescales and even the generation of new exotic non-equilibrium phases. In many cases, studying the dynamics which follow intense photo-excitation can also enable us to disentangle the competing energy scales which dictate the often poorly-understood equilibrium properties of these materials.

During the last decade, a wealth of experiments which appear to show an enhancement of superconductivity upon strong-field photo-excitation have been reported. A selection of such experiments, conducted in various cuprate superconductors as well as the molecular superconductor κ -(BEDT-TTF)₂Cu[N(CN)₂]Br, in which signatures of superconductivity in the THz-frequency optical properties were observed to emerge following photo-excitation at temperatures exceeding T_c , were summarized in chapter 2.

The present work is focused primarily on the case of K_3C_{60} , to which a more comprehensive introduction was devoted in chapter 3. Previous experiments exploring the effect of mid-infrared photo-excitation on K_3C_{60} have found a non-equilibrium state with superconducting-like THz frequency optical properties. Provided that the excitation pulse energy is sufficiently strong, these superconducting-like properties persist on a nanosecond timescale - much longer than the light-induced superconducting-like states observed in other materials. Further experiments investigating the pressure dependence and transport properties of the photo-induced state have also provided evidence consistent with the interpretation of a photo-induced superconducting state far above T_c .

In chapter 4, new data measured on K_3C_{60} was presented, in which the effect of photo-exciting with lower frequencies than were previously accessible was comprehensively studied. The effect of photo-excitation on the THz frequency optical properties was studied for all photo-excitation frequencies between approximately 6 and 36 THz. Throughout this range, photo-excitation results in the emergence of the same non-equilibrium state which was reported in previous experiments. Strikingly though, a resonant enhancement of the photo-excitation efficiency for pump frequencies close to 10 THz was discovered, enabling the same long-lived superconducting-like state to be generated with approximately one hundred-fold less fluence than in the previous experiments. This resonant enhancement also enabled the first room temperature observation of the long-lived superconducting-like state.

The microscopic mechanism responsible for the formation of the superconducting-like state upon photo-excitation has been a topic of intense theoretical debate. Indeed, even the pairing mechanism for equilibrium superconductivity in K_3C_{60} is not univer-

sally agreed upon, so understanding the origin of this exotic non-equilibrium state appears almost intractable. Nevertheless, more extensive characterization of the non-equilibrium response throughout the full phase space of experimental parameters presents a sure path towards progress, with the work presented here representing a significant step forwards in that direction. The identification of 10 THz as the energy scale for excitation provides a quantitative constraint to all future theoretical attempts to model the formation of the non-equilibrium superconducting-like state. This energy scale points towards at least three distinct underlying types of excitation - excitations of the many-body electronic wavefunction, resonant driving of phonon modes and the formation of excitons. The implications of each of these candidates, and combinations thereof, should be the subject of future theoretical investigation.

Future experimental investigation into the non-equilibrium superconducting-like state of K_3C_{60} should progress in two directions. The first direction is to implement new probing techniques in order to better characterize the light-induced state, and understand the dynamical processes which lead to its formation. A template for this line of research is provided by the library of experiments which have been carried out in relation to light-induced superconductivity in $\text{YBa}_2\text{Cu}_3\text{O}_{6+x}$. In those samples, the initial THz-probing observations of superconducting-like optical properties have been followed by various measurements sensitive to the microscopic dynamics which follow photo-excitation, utilizing both x-ray and near-infrared probing on short timescales. In that case, the results have led to new insights not only in relation to the light-induced superconducting-like state, but also regarding the equilibrium properties of the poorly understood above- T_c phase. Such a measurement campaign would surely prove fruitful if carried out in K_3C_{60} .

The second direction for future research is to work towards functionalizing the exotic properties of this state. The existing work incorporating thin films of K_3C_{60} , which can be photo-excited, into electronic chips presents an intriguing path towards the use of the non-equilibrium state in electronic devices. The extension of the non-equilibrium state to room temperature and with significantly lower excitation fluences, presented in chapter 4, drastically increases the feasibility of using such devices for real applications in the future. Additionally, the low excitation fluence, combined with the long lifetime of the non-equilibrium state, could enable future experiments in which trains of pulses delivered at GHz repetition rates further extend the lifetime of the non-equilibrium state.

List of Publications

The work presented in chapter 4 of this thesis is based on the following publication:

- **E. Rowe**, B. Yuan, M. Buzzi, G. Jotzu, Y. Zhu, M. Fechner, M. Först, B. Liu, D. Pontiroli, M. Riccò, and A. Cavalleri, “Resonant enhancement of photo-induced superconductivity in K_3C_{60} ”, *Nature Physics* **19**, 1821–1826 (2023).

I also worked on projects not central to the main narrative of this thesis, resulting in the following publications:

- A. von Hoegen, M. Fechner, M. Först, N. Taherian, **E. Rowe**, A. Ribak, J. Porras, B. Keimer, M. Michael, E. Demler, and A. Cavalleri “Amplification of superconducting fluctuations in driven $YBa_2Cu_3O_{6+x}$ ” *Physical Review X* **12**, 031008 (2022);
- M. Henstridge, M. Först, **E. Rowe**, M. Fechner, A. Cavalleri “Nonlocal non-linear phononics”, *Nature Physics* **18**, 457-461 (2022)
- N. Taherian, M. Först, A. Liu, M. Fechner, D. Pavicevic, A. von Hoegen, **E. Rowe**, Y. Liu, S. Nakata, B. Keimer, E. Demler, M. H. Michael, A. Cavalleri “Squeezed Josephson plasmons in driven $YBa_2Cu_3O_{6+x}$ ” *ArXiv* 2401.01115 (2024)

Bibliography

- ¹D. Fausti, R. I. Tobey, N. Dean, S. Kaiser, A. Dienst, M. C. Hoffmann, S. Pyon, T. Takayama, H. Takagi, and A. Cavalleri, “Light-induced superconductivity in a stripe-ordered cuprate”, *Science* **331**, 189–191 (2011).
- ²D. Nicoletti, E. Casandruc, Y. Laplace, V. Khanna, C. R. Hunt, S. Kaiser, S. S. Dhesi, G. D. Gu, J. P. Hill, and A. Cavalleri, “Optically induced superconductivity in striped $\text{La}_{2-x}\text{Ba}_x\text{CuO}_4$ by polarization-selective excitation in the near infrared”, *Physical Review B* **90**, 100503 (2014).
- ³S. Kaiser, C. R. Hunt, D. Nicoletti, W. Hu, I. Gierz, H. Y. Liu, M. Le Tacon, T. Loew, D. Haug, B. Keimer, and A. Cavalleri, “Optically induced coherent transport far above T_c in underdoped $\text{YBa}_2\text{Cu}_3\text{O}_{6+\delta}$ ”, *Physical Review B* **89**, 184516 (2014).
- ⁴W. Hu, S. Kaiser, D. Nicoletti, C. R. Hunt, I. Gierz, M. C. Hoffmann, M. Le Tacon, T. Loew, B. Keimer, and A. Cavalleri, “Optically enhanced coherent transport in $\text{YBa}_2\text{Cu}_3\text{O}_{6.5}$ by ultrafast redistribution of interlayer coupling”, *Nature Materials* **13**, 705–711 (2014).
- ⁵M. Mitrano, A. Cantaluppi, D. Nicoletti, S. Kaiser, A. Perucchi, S. Lupi, P. Di Pietro, D. Pontiroli, M. Riccò, S. R. Clark, D. Jaksch, and A. Cavalleri, “Possible

- light-induced superconductivity in K_3C_{60} at high temperature”, *Nature* **530**, 461–464 (2016).
- ⁶M. Buzzi, D. Nicoletti, M. Fechner, N. Tancogne-Dejean, M. A. Sentef, A. Georges, T. Biesner, E. Uykur, M. Dressel, A. Henderson, T. Siegrist, J. A. Schlueter, K. Miyagawa, K. Kanoda, M.-S. Nam, A. Ardavan, J. Coulthard, J. Tindall, F. Schlawin, D. Jaksch, and A. Cavalleri, “Photomolecular high-temperature superconductivity”, *Physical Review X* **10**, 031028 (2020).
- ⁷K. Isoyama, N. Yoshikawa, K. Katsumi, J. Wong, N. Shikama, Y. Sakishita, F. Nabeshima, A. Maeda, and R. Shimano, “Light-induced enhancement of superconductivity in iron-based superconductor $FeSe_{0.5}Te_{0.5}$ ”, *Communications Physics* **4**, 1–9 (2021).
- ⁸T. Suzuki, T. Someya, T. Hashimoto, S. Michimae, M. Watanabe, M. Fujisawa, T. Kanai, N. Ishii, J. Itatani, S. Kasahara, Y. Matsuda, T. Shibauchi, K. Okazaki, and S. Shin, “Photoinduced possible superconducting state with long-lived disproportionate band filling in $FeSe$ ”, *Communications Physics* **2**, 1–7 (2019).
- ⁹A. Kogar, A. Zong, P. E. Dolgirev, X. Shen, J. Straquadine, Y.-Q. Bie, X. Wang, T. Rohwer, I.-C. Tung, Y. Yang, R. Li, J. Yang, S. Weathersby, S. Park, M. E. Kozina, E. J. Sie, H. Wen, P. Jarillo-Herrero, I. R. Fisher, X. Wang, and N. Gedik, “Light-induced charge density wave in $LaTe_3$ ”, *Nature Physics* **16**, 159–163 (2020).
- ¹⁰S. Wandel, F. Boschini, E. H. da Silva Neto, L. Shen, M. X. Na, S. Zohar, Y. Wang, S. B. Welch, M. H. Seaberg, J. D. Koralek, G. L. Dakovski, W. Hettel, M.-F. Lin, S. P. Moeller, W. F. Schlotter, A. H. Reid, M. P. Minitti, T. Boyle, F. He, R. Sutarto, R. Liang, D. Bonn, W. Hardy, R. A. Kaindl, D. G. Hawthorn, J.-S. Lee, A. F. Kemper, A. Damascelli, C. Giannetti, J. J. Turner, and G. Coslovich,

- “Enhanced charge density wave coherence in a light-quenched, high-temperature superconductor”, *Science* **376**, 860–864 (2022).
- ¹¹A. S. Disa, M. Fechner, T. F. Nova, B. Liu, M. Först, D. Prabhakaran, P. G. Radaelli, and A. Cavalleri, “Polarizing an antiferromagnet by optical engineering of the crystal field”, *Nature Physics* **16**, 937–941 (2020).
- ¹²X. Wang, C. Xiao, H. Park, J. Zhu, C. Wang, T. Taniguchi, K. Watanabe, J. Yan, D. Xiao, D. R. Gamelin, W. Yao, and X. Xu, “Light-induced ferromagnetism in moiré superlattices”, *Nature* **604**, 468–473 (2022).
- ¹³I. Radu, K. Vahaplar, C. Stamm, T. Kachel, N. Pontius, H. A. Dürr, T. A. Ostler, J. Barker, R. F. L. Evans, R. W. Chantrell, A. Tsukamoto, A. Itoh, A. Kirilyuk, T. Rasing, and A. V. Kimel, “Transient ferromagnetic-like state mediating ultrafast reversal of antiferromagnetically coupled spins”, *Nature* **472**, 205–208 (2011).
- ¹⁴Y. H. Wang, H. Steinberg, P. Jarillo-Herrero, and N. Gedik, “Observation of floquet-Bloch states on the surface of a topological insulator”, *Science* **342**, 453–457 (2013).
- ¹⁵J. W. McIver, B. Schulte, F.-U. Stein, T. Matsuyama, G. Jotzu, G. Meier, and A. Cavalleri, “Light-induced anomalous Hall effect in graphene”, *Nature Physics* **16**, 38–41 (2020).
- ¹⁶A. S. Disa, T. F. Nova, and A. Cavalleri, “Engineering crystal structures with light”, *Nature Physics* **17**, 1087–1092 (2021).
- ¹⁷A. de la Torre, D. M. Kennes, M. Claassen, S. Gerber, J. W. McIver, and M. A. Sentef, “Colloquium: Nonthermal pathways to ultrafast control in quantum materials”, *Reviews of Modern Physics* **93**, 041002 (2021).

- ¹⁸R. F. Wallis and A. A. Maradudin, “Ionic Raman effect. II. The first-order ionic Raman effect”, *Physical Review B* **3**, 2063–2075 (1971).
- ¹⁹T. P. Martin and L. Genzel, “Ionic Raman scattering and ionic frequency mixing”, *physica status solidi (b)* **61**, 493–502 (1974).
- ²⁰D. L. Mills, “Ionic contributions to the Raman tensor of insulators”, *Physical Review B* **35**, 9278–9283 (1987).
- ²¹M. Först, C. Manzoni, S. Kaiser, Y. Tomioka, Y. Tokura, R. Merlin, and A. Cavalleri, “Nonlinear phononics as an ultrafast route to lattice control”, *Nature Physics* **7**, 854–856 (2011).
- ²²A. S. Disa, J. Curtis, M. Fechner, A. Liu, A. von Hoegen, M. Först, T. F. Nova, P. Narang, A. Maljuk, A. V. Boris, B. Keimer, and A. Cavalleri, “Photo-induced high-temperature ferromagnetism in YTiO_3 ”, *Nature* **617**, 73–78 (2023).
- ²³M. Mochizuki and M. Imada, “Orbital physics in the perovskite Ti oxides”, *New Journal of Physics* **6**, 154 (2004).
- ²⁴M. Tsubota, F. Iga, T. Takabatake, N. Kikugawa, T. Suzuki, I. Oguro, H. Kawanaka, and H. Bando, “Low-field magnetic anisotropy in Mott-insulating ferromagnet $\text{Y}_{1-x}\text{Ca}_x\text{TiO}_3$ ($x \leq 0.1$)”, *Physica B: Condensed Matter* **281-282**, 622–624 (2000).
- ²⁵G. Khaliullin and S. Okamoto, “Theory of orbital state and spin interactions in ferromagnetic titanates”, *Physical Review B* **68**, 205109 (2003).
- ²⁶C. Ulrich, G. Khaliullin, S. Okamoto, M. Reehuis, A. Ivanov, H. He, Y. Taguchi, Y. Tokura, and B. Keimer, “Magnetic order and dynamics in an orbitally degenerate ferromagnetic insulator”, *Physical Review Letters* **89**, 167202 (2002).
- ²⁷C. Yao and Y. Ma, “Superconducting materials: Challenges and opportunities for large-scale applications”, *iScience* **24**, 102541 (2021).

- ²⁸H.-L. Huang, D. Wu, D. Fan, and X. Zhu, “Superconducting quantum computing: a review”, *Science China Information Sciences* **63**, 180501 (2020).
- ²⁹J. G. Bednorz and K. A. Müller, “Possible high- T_c superconductivity in the Ba-La-Cu-O system”, *Zeitschrift für Physik B Condensed Matter* **64**, 189–193 (1986).
- ³⁰A. F. G. Wyatt, V. M. Dmitriev, W. S. Moore, and F. W. Sheard, “Microwave-enhanced critical supercurrents in constricted tin films”, *Physical Review Letters* **16**, 1166–1169 (1966).
- ³¹A. H. Dayem and J. J. Wiegand, “Behavior of thin-film superconducting bridges in a microwave field”, *Physical Review* **155**, 419–428 (1967).
- ³²T. M. Klapwijk and J. E. Mooij, “Microwave-enhanced superconductivity in aluminium films”, *Physica B+C* **81**, 132–136 (1976).
- ³³G. M. Eliashberg, “Film superconductivity stimulated by a high-frequency field”, *JETP Lett.* **11** (1970).
- ³⁴G. Yu, A. J. Heeger, G. Stucky, N. Herron, and E. M. McCarron, “Transient photoinduced conductivity in semiconducting single crystals of $\text{YBa}_2\text{Cu}_3\text{O}_{6.3}$: Search for photoinduced metallic state and for photoinduced superconductivity”, *Solid State Communications* **72**, 345–349 (1989).
- ³⁵G. Yu, C. H. Lee, A. J. Heeger, N. Herron, E. M. McCarron, L. Cong, G. C. Spalding, C. A. Nordman, and A. M. Goldman, “Phase separation of photogenerated carriers and photoinduced superconductivity in high- T_c materials”, *Physical Review B* **45**, 4964–4977 (1992).
- ³⁶G. Nieva, E. Osquiguil, J. Guimpel, M. Maenhoudt, B. Wuyts, Y. Bruynseraede, M. B. Maple, and I. K. Schuller, “Photoinduced enhancement of superconductivity”, *Applied Physics Letters* **60**, 2159–2161 (1992).

- ³⁷D. Lederman, E. Osquiguil, G. Nieva, J. Guimpel, J. Hasen, Y. Bruynseraede, and I. K. Schuller, “Photoinduced enhancement of superconductivity”, *Journal of Superconductivity* **7**, 127–130 (1994).
- ³⁸M. K. Wu, J. R. Ashburn, C. J. Torng, P. H. Hor, R. L. Meng, L. Gao, Z. J. Huang, Y. Q. Wang, and C. W. Chu, “Superconductivity at 93 K in a new mixed-phase Y-Ba-Cu-O compound system at ambient pressure”, *Physical Review Letters* **58**, 908–910 (1987).
- ³⁹J. Bardeen, L. N. Cooper, and J. R. Schrieffer, “Theory of superconductivity”, *Physical Review* **108**, 1175–1204 (1957).
- ⁴⁰M. Tinkham, *Introduction to superconductivity* (Dover Publications, 2004).
- ⁴¹H. Fröhlich, “Theory of the superconducting state. I. The ground state at the absolute zero of temperature”, *Physical Review* **79**, 845–856 (1950).
- ⁴²W. L. McMillan, “Transition temperature of strong-coupled superconductors”, *Physical Review* **167**, 331–344 (1968).
- ⁴³V. L. Ginzburg and L. D. Landau, “On the theory of superconductivity”, *Zh. Eksperim. i. Teor. Fiz.*, 1064 (1950).
- ⁴⁴R. Shimano and N. Tsuji, “Higgs Mode in Superconductors”, *Annual Review of Condensed Matter Physics* **11**, 103–124 (2020).
- ⁴⁵V. J. Emery and S. A. Kivelson, “Importance of phase fluctuations in superconductors with small superfluid density”, *Nature* **374**, 434–437 (1995).
- ⁴⁶Y. J. Uemura, “Dynamic superconductivity responses in photoexcited optical conductivity and Nernst effect”, *Physical Review Materials* **3**, 104801 (2019).
- ⁴⁷D. C. Mattis and J. Bardeen, “Theory of the anomalous skin effect in normal and superconducting metals”, *Physical Review* **111**, 412–417 (1958).

- ⁴⁸R. E. Glover and M. Tinkham, “Conductivity of superconducting films for photon energies between 0.3 and $40kT_c$ ”, *Physical Review* **108**, 243–256 (1957).
- ⁴⁹R. Boyd, *Nonlinear Optics* (Academic Press, 2008).
- ⁵⁰J. Muller, “A15-type superconductors”, *Reports on Progress in Physics* **43**, 641 (1980).
- ⁵¹P. Dai, B. C. Chakoumakos, G. F. Sun, K. W. Wong, Y. Xin, and D. F. Lu, “Synthesis and neutron powder diffraction study of the superconductor $\text{HgBa}_2\text{Ca}_2\text{Cu}_3\text{O}_{8+\delta}$ by Tl substitution”, *Physica C: Superconductivity* **243**, 201–206 (1995).
- ⁵²N. Plakida, *High-Temperature Cuprate Superconductors* (Springer, 2010).
- ⁵³B. D. Josephson, “Possible new effects in superconductive tunnelling”, *Physics Letters* **1**, 251–253 (1962).
- ⁵⁴B. Josephson, “Supercurrents through barriers”, *Advances in Physics* **14**, 419–451 (1965).
- ⁵⁵R. Kleiner and P. Müller, “Intrinsic Josephson effects in high- T_c superconductors”, *Physical Review B* **49**, 1327–1341 (1994).
- ⁵⁶C. R. Hunt, D. Nicoletti, S. Kaiser, T. Takayama, H. Takagi, and A. Cavalleri, “Two distinct kinetic regimes for the relaxation of light-induced superconductivity in $\text{La}_{1.675}\text{Eu}_{0.2}\text{Sr}_{0.125}\text{CuO}_4$ ”, *Physical Review B* **91**, 020505 (2015).
- ⁵⁷M. Först, R. I. Tobey, H. Bromberger, S. B. Wilkins, V. Khanna, A. D. Caviglia, Y.-D. Chuang, W. S. Lee, W. F. Schlotter, J. J. Turner, M. P. Minitti, O. Krupin, Z. J. Xu, J. S. Wen, G. D. Gu, S. S. Dhesi, A. Cavalleri, and J. P. Hill, “Melting of charge stripes in vibrationally driven $\text{La}_{1.875}\text{Ba}_{0.125}\text{CuO}_4$: Assessing the respective roles of electronic and lattice order in frustrated superconductors”, *Physical Review Letters* **112**, 157002 (2014).

- ⁵⁸K. A. Cremin, J. Zhang, C. C. Homes, G. D. Gu, Z. Sun, M. M. Fogler, A. J. Millis, D. N. Basov, and R. D. Averitt, “Photoenhanced metastable c-axis electro-dynamics in stripe-ordered cuprate $\text{La}_{1.885}\text{Ba}_{0.115}\text{CuO}_4$ ”, Proceedings of the National Academy of Sciences **116**, 19875–19879 (2019).
- ⁵⁹S. Rajasekaran, J. Okamoto, L. Mathey, M. Fechner, V. Thampy, G. D. Gu, and A. Cavalleri, “Probing optically silent superfluid stripes in cuprates”, Science **359**, 575–579 (2018).
- ⁶⁰A. Simon, K. Trübenbach, and H. Borrmann, “Single crystal x-ray structure analysis of $\text{YBa}_2\text{Cu}_3\text{O}_{6.5}$ ”, Journal of Solid State Chemistry **106**, 128–133 (1993).
- ⁶¹A. Williams, G. H. Kwei, R. B. Von Dreele, I. D. Raistrick, and D. L. Bish, “Joint x-ray and neutron refinement of the structure of superconducting $\text{YBa}_2\text{Cu}_3\text{O}_{7-x}$: Precision structure, anisotropic thermal parameters, strain, and cation disorder”, Physical Review B **37**, 7960–7962 (1988).
- ⁶²O. Cyr-Choinière, R. Daou, F. Laliberté, C. Collignon, S. Badoux, D. LeBoeuf, J. Chang, B. J. Ramshaw, D. A. Bonn, W. N. Hardy, R. Liang, J.-Q. Yan, J.-G. Cheng, J.-S. Zhou, J. B. Goodenough, S. Pyon, T. Takayama, H. Takagi, N. Doiron-Leyraud, and L. Taillefer, “Pseudogap temperature T^* of cuprate superconductors from the Nernst effect”, Physical Review B **97**, 064502 (2018).
- ⁶³J. H. Brewer, E. J. Ansaldo, J. F. Carolan, A. C. D. Chaklader, W. N. Hardy, D. R. Harshman, M. E. Hayden, M. Ishikawa, N. Kaplan, R. Keitel, J. Kempton, R. F. Kiefl, W. J. Kossler, S. R. Kreitzman, A. Kulpa, Y. Kuno, G. M. Luke, H. Miyatake, K. Nagamine, Y. Nakazawa, N. Nishida, K. Nishiyama, S. Ohkuma, T. M. Riseman, G. Roehmer, P. Schleger, D. Shimada, C. E. Stronach, T. Takabatake, Y. J. Uemura, Y. Watanabe, D. L. Williams, T. Yamazaki, and B. Yang, “Anti-

- ferromagnetism and superconductivity in oxygen-deficient $\text{YBa}_2\text{Cu}_3\text{O}_x$ ”, *Physical Review Letters* **60**, 1073–1076 (1988).
- ⁶⁴M. Hücker, N. B. Christensen, A. T. Holmes, E. Blackburn, E. M. Forgan, R. Liang, D. A. Bonn, W. N. Hardy, O. Gutowski, M. v. Zimmermann, S. M. Hayden, and J. Chang, “Competing charge, spin, and superconducting orders in underdoped $\text{YBa}_2\text{Cu}_3\text{O}_y$ ”, *Physical Review B* **90**, 054514 (2014).
- ⁶⁵S. Blanco-Canosa, A. Frano, E. Schierle, J. Porras, T. Loew, M. Minola, M. Bluschke, E. Weschke, B. Keimer, and M. Le Tacon, “Resonant x-ray scattering study of charge-density wave correlations in $\text{YBa}_2\text{Cu}_3\text{O}_{6+x}$ ”, *Physical Review B* **90**, 054513 (2014).
- ⁶⁶R. Liang, D. A. Bonn, and W. N. Hardy, “Evaluation of CuO_2 plane hole doping in $\text{YBa}_2\text{Cu}_3\text{O}_{6+x}$ single crystals”, *Physical Review B* **73**, 180505 (2006).
- ⁶⁷Y. Ando, S. Komiya, K. Segawa, S. Ono, and Y. Kurita, “Electronic phase diagram of high- T_c cuprate superconductors from a mapping of the in-plane resistivity curvature”, *Physical Review Letters* **93**, 267001 (2004).
- ⁶⁸C. R. Hunt, D. Nicoletti, S. Kaiser, D. Präpper, T. Loew, J. Porras, B. Keimer, and A. Cavalleri, “Dynamical decoherence of the light induced interlayer coupling in $\text{YBa}_2\text{Cu}_3\text{O}_{6+\delta}$ ”, *Physical Review B* **94**, 224303 (2016).
- ⁶⁹B. Liu, M. Först, M. Fechner, D. Nicoletti, J. Porras, T. Loew, B. Keimer, and A. Cavalleri, “Pump frequency resonances for light-induced incipient superconductivity in $\text{YBa}_2\text{Cu}_3\text{O}_{6.5}$ ”, *Physical Review X* **10**, 011053 (2020).
- ⁷⁰B. Liu, H. Bromberger, A. Cartella, T. Gebert, M. Först, and A. Cavalleri, “Generation of narrowband, high-intensity, carrier-envelope phase-stable pulses tunable between 4 and 18 THz”, *Optics Letters* **42**, 129–131 (2017).

- ⁷¹R. Mankowsky, M. Först, T. Loew, J. Porras, B. Keimer, and A. Cavalleri, “Coherent modulation of the $\text{YBa}_2\text{Cu}_3\text{O}_{6+x}$ atomic structure by dispersive stimulated ionic Raman scattering”, *Physical Review B* **91**, 094308 (2015).
- ⁷²R. Mankowsky, A. Subedi, M. Först, S. O. Mariager, M. Chollet, H. T. Lemke, J. S. Robinson, J. M. Glowia, M. P. Minitti, A. Frano, M. Fechner, N. A. Spaldin, T. Loew, B. Keimer, A. Georges, and A. Cavalleri, “Nonlinear lattice dynamics as a basis for enhanced superconductivity in $\text{YBa}_2\text{Cu}_3\text{O}_{6.5}$ ”, *Nature* **516**, 71–73 (2014).
- ⁷³R. Mankowsky, M. Fechner, M. Först, A. von Hoegen, J. Porras, T. Loew, G. L. Dakovski, M. Seaberg, S. Möller, G. Coslovich, B. Keimer, S. S. Dhesi, and A. Cavalleri, “Optically induced lattice deformations, electronic structure changes, and enhanced superconductivity in $\text{YBa}_2\text{Cu}_3\text{O}_{6.48}$ ”, *Structural Dynamics* **4**, 044007 (2017).
- ⁷⁴M. Först, A. Frano, S. Kaiser, R. Mankowsky, C. R. Hunt, J. J. Turner, G. L. Dakovski, M. P. Minitti, J. Robinson, T. Loew, M. Le Tacon, B. Keimer, J. P. Hill, A. Cavalleri, and S. S. Dhesi, “Femtosecond x rays link melting of charge-density wave correlations and light-enhanced coherent transport in $\text{YBa}_2\text{Cu}_3\text{O}_{6.6}$ ”, *Physical Review B* **90**, 184514 (2014).
- ⁷⁵A. von Hoegen, M. Fechner, M. Först, N. Taherian, E. Rowe, A. Ribak, J. Porras, B. Keimer, M. Michael, E. Demler, and A. Cavalleri, “Amplification of superconducting fluctuations in driven $\text{YBa}_2\text{Cu}_3\text{O}_{6+x}$ ”, *Physical Review X* **12**, 031008 (2022).
- ⁷⁶N. Taherian, M. Först, A. Liu, M. Fechner, D. Pavicevic, A. von Hoegen, E. Rowe, Y. Liu, S. Nakata, B. Keimer, E. Demler, M. H. Michael, and A. Caval-

- leri, “Squeezed Josephson plasmons in driven $\text{YBa}_2\text{Cu}_3\text{O}_{6+x}$ ”, arXiv:2401.01115 (2024).
- ⁷⁷H. Vogt, “Coherent and hyper-raman techniques”, in *Light Scattering in Solids II: Basic Concepts and Instrumentation*, Topics in Applied Physics (Springer, Berlin, Heidelberg, 1982), pp. 207–244.
- ⁷⁸M. H. Michael, A. von Hoegen, M. Fechner, M. Först, A. Cavalleri, and E. Demler, “Parametric resonance of Josephson plasma waves: A theory for optically amplified interlayer superconductivity in $\text{YBa}_2\text{Cu}_3\text{O}_{6+x}$ ”, *Physical Review B* **102**, 174505 (2020).
- ⁷⁹M. H. Michael, M. Först, D. Nicoletti, S. R. U. Haque, Y. Zhang, A. Cavalleri, R. D. Averitt, D. Podolsky, and E. Demler, “Generalized Fresnel-Floquet equations for driven quantum materials”, *Physical Review B* **105**, 174301 (2022).
- ⁸⁰R. Singla, G. Cotugno, S. Kaiser, M. Först, M. Mitrano, H. Y. Liu, A. Cartella, C. Manzoni, H. Okamoto, T. Hasegawa, S. R. Clark, D. Jaksch, and A. Cavalleri, “THz-frequency modulation of the Hubbard U in an organic mott insulator”, *Physical Review Letters* **115**, 187401 (2015).
- ⁸¹S. Kaiser, S. R. Clark, D. Nicoletti, G. Cotugno, R. I. Tobey, N. Dean, S. Lupi, H. Okamoto, T. Hasegawa, D. Jaksch, and A. Cavalleri, “Optical properties of a vibrationally modulated solid state mott insulator”, *Scientific Reports* **4**, 3823 (2014).
- ⁸²J. Tindall, F. Schlawin, M. Buzzi, D. Nicoletti, J. R. Coulthard, H. Gao, A. Cavalleri, M. A. Sentef, and D. Jaksch, “Dynamical order and superconductivity in a frustrated many-body system”, *Physical Review Letters* **125**, 137001 (2020).

- ⁸³M.-S. Nam, A. Ardavan, S. J. Blundell, and J. A. Schlueter, “Fluctuating superconductivity in organic molecular metals close to the Mott transition”, *Nature* **449**, 584–587 (2007).
- ⁸⁴M. Buzzi, D. Nicoletti, S. Fava, G. Jotzu, K. Miyagawa, K. Kanoda, A. Henderson, T. Siegrist, J. A. Schlueter, M.-S. Nam, A. Ardavan, and A. Cavalleri, “Phase diagram for light-induced superconductivity in κ -(ET)₂-X”, *Physical Review Letters* **127**, 197002 (2021).
- ⁸⁵A. F. Hebard, M. J. Rosseinsky, R. C. Haddon, D. W. Murphy, S. H. Glarum, T. T. M. Palstra, A. P. Ramirez, and A. R. Kortan, “Superconductivity at 18 K in potassium-doped C₆₀”, *Nature* **350**, 600–601 (1991).
- ⁸⁶T. T. M. Palstra, O. Zhou, Y. Iwasa, P. E. Sulewski, R. M. Fleming, and B. R. Zegarski, “Superconductivity at 40 K in cesium doped C₆₀”, *Solid State Communications* **93**, 327–330 (1995).
- ⁸⁷O. Gunnarsson, “Superconductivity in fullerenes”, *Reviews of Modern Physics* **69**, 575–606 (1997).
- ⁸⁸A. Cantaluppi, M. Buzzi, G. Jotzu, D. Nicoletti, M. Mitranò, D. Pontiroli, M. Riccò, A. Perucchi, P. Di Pietro, and A. Cavalleri, “Pressure tuning of light-induced superconductivity in K₃C₆₀”, *Nature Physics* **14**, 837–841 (2018).
- ⁸⁹M. Budden, T. Gebert, M. Buzzi, G. Jotzu, E. Wang, T. Matsuyama, G. Meier, Y. Laplace, D. Pontiroli, M. Riccò, F. Schlawin, D. Jaksch, and A. Cavalleri, “Evidence for metastable photo-induced superconductivity in K₃C₆₀”, *Nature Physics* **17**, 611–618 (2021).

- ⁹⁰E. Wang, J. D. Adelinia, M. Chavez-Cervantes, T. Matsuyama, M. Fechner, M. Buzzi, G. Meier, and A. Cavalleri, “Superconducting nonlinear transport in optically driven high-temperature K_3C_{60} ”, *Nature Communications* **14**, 7233 (2023).
- ⁹¹M. Buzzi, G. Jotzu, A. Cavalleri, J. I. Cirac, E. A. Demler, B. I. Halperin, M. D. Lukin, T. Shi, Y. Wang, and D. Podolsky, “Higgs-mediated optical amplification in a nonequilibrium superconductor”, *Physical Review X* **11**, 011055 (2021).
- ⁹²R. H. Zadik, Y. Takabayashi, G. Klupp, R. H. Colman, A. Y. Ganin, A. Potočník, P. Jeglič, D. Arčon, P. Matus, K. Kamarás, Y. Kasahara, Y. Iwasa, A. N. Fitch, Y. Ohishi, G. Garbarino, K. Kato, M. J. Rosseinsky, and K. Prassides, “Optimized unconventional superconductivity in a molecular Jahn-Teller metal”, *Science Advances* **1**, e1500059 (2015).
- ⁹³M. Budden, *Metastable light-induced superconductivity in K_3C_{60}* (Hamburg, 2020).
- ⁹⁴P. W. Stephens, L. Mihaly, P. L. Lee, R. L. Whetten, S.-M. Huang, R. Kaner, F. Deiderich, and K. Holczer, “Structure of single-phase superconducting K_3C_{60} ”, *Nature* **351**, 632–634 (1991).
- ⁹⁵A. Y. Ganin, Y. Takabayashi, Y. Z. Khimyak, S. Margadonna, A. Tamai, M. J. Rosseinsky, and K. Prassides, “Bulk superconductivity at 38 K in a molecular system”, *Nature Materials* **7**, 367–371 (2008).
- ⁹⁶Y. Takabayashi, A. Y. Ganin, P. Jeglič, D. Arčon, T. Takano, Y. Iwasa, Y. Ohishi, M. Takata, N. Takeshita, K. Prassides, and M. J. Rosseinsky, “The disorder-free non-BCS superconductor Cs_3C_{60} emerges from an antiferromagnetic insulator parent state”, *Science* **323**, 1585–1590 (2009).

- ⁹⁷Y. Ihara, H. Alloul, P. Wzietek, D. Pontiroli, M. Mazzani, and M. Riccò, “Spin dynamics at the Mott transition and in the metallic state of the Cs_3C_{60} superconducting phases”, *Europhysics Letters* **94**, 37007 (2011).
- ⁹⁸S. C. Erwin and W. E. Pickett, “Theoretical fermi-surface properties and superconducting parameters for K_3C_{60} ”, *Science* **254**, 842–845 (1991).
- ⁹⁹K. Prassides, J. Tomkinson, C. Christides, M. J. Rosseinsky, D. W. Murphy, and R. C. Haddon, “Vibrational spectroscopy of superconducting K_3C_{60} by inelastic neutron scattering”, *Nature* **354**, 462–463 (1991).
- ¹⁰⁰R.-S. Wang, D. Peng, L.-N. Zong, Z.-W. Zhu, and X.-J. Chen, “Full set of superconducting parameters of K_3C_{60} ”, *Carbon* **202**, 325–335 (2023).
- ¹⁰¹L. Degiorgi, G. Briceno, M. S. Fuhrer, A. Zettl, and P. Wachter, “Optical measurements of the superconducting gap in single-crystal K_3C_{60} and Rb_3C_{60} ”, *Nature* **369**, 541–543 (1994).
- ¹⁰²R. Hesper, L. H. Tjeng, A. Heeres, and G. A. Sawatzky, “BCS-like density of states in superconducting A_3C_{60} surfaces”, *Physical Review Letters* **85**, 1970–1973 (2000).
- ¹⁰³R. Tycko, G. Dabbagh, M. J. Rosseinsky, D. W. Murphy, A. P. Ramirez, and R. M. Fleming, “Electronic properties of normal and superconducting alkali fullerenes probed by ^{13}C nuclear magnetic resonance”, *Physical Review Letters* **68**, 1912–1915 (1992).
- ¹⁰⁴Z. Zhang, C.-C. Chen, and C. M. Lieber, “Tunneling spectroscopy of M_3C_{60} superconductors: the energy gap, strong coupling, and superconductivity”, *Science* **254**, 1619–1621 (1991).

- ¹⁰⁵M.-Q. Ren, S. Han, S.-Z. Wang, J.-Q. Fan, C.-L. Song, X.-C. Ma, and Q.-K. Xue, “Direct observation of full-gap superconductivity and pseudogap in two-dimensional fullerides”, *Physical Review Letters* **124**, 187001 (2020).
- ¹⁰⁶S. Sasaki, A. Matsuda, and C. Chu, “Fermi-liquid behavior and BCS s-wave pairing of K_3C_{60} observed by ^{13}C -NMR”, *Journal of the Physical Society of Japan* **63**, 1670–1673 (1994).
- ¹⁰⁷C. M. Varma, J. Zaanen, and K. Raghavachari, “Superconductivity in the Fullerenes”, *Science* **254**, 989–992 (1991).
- ¹⁰⁸A. Potočnik, A. Krajnc, P. Jeglič, Y. Takabayashi, A. Y. Ganin, K. Prassides, M. J. Rosseinsky, and D. Arčon, “Size and symmetry of the superconducting gap in the f.c.c. Cs_3C_{60} polymorph close to the metal-Mott insulator boundary”, *Scientific Reports* **4**, 4265 (2014).
- ¹⁰⁹C. C. Chen and C. M. Lieber, “Synthesis of pure $^{13}C_{60}$ and determination of the isotope effect for fullerene superconductors”, *Journal of the American Chemical Society* **114**, 3141–3142 (1992).
- ¹¹⁰M. Riccò, F. Gianferrari, D. Pontiroli, M. Belli, C. Bucci, and T. Shiroka, “Unconventional isotope effects in superconducting fullerides”, *Europhysics Letters* **81**, 57002 (2008).
- ¹¹¹A. A. Zakhidov, K. Imaeda, D. M. Petty, K. Yakushi, H. Inokuchi, K. Kikuchi, I. Ikemoto, S. Suzuki, and Y. Achiba, “Enhanced isotope effect in ^{13}C -rich superconducting M_xC_{60} ($M=K, Rb$): support for vibronic pairing”, *Physics Letters A* **164**, 355–361 (1992).

- ¹¹²P. Auban-Senzier, G. Quirion, D. Jerome, P. Bernier, S. Della-Negra, C. Fabre, and A. Rassat, “Isotope effect on 82% ^{13}C substituted K_3C_{60} ”, *Synthetic Metals* **56**, 3027–3032 (1993).
- ¹¹³B. Burk, V. H. Crespi, A. Zettl, and M. L. Cohen, “Rubidium isotope effect in superconducting Rb_3C_{60} ”, *Physical Review Letters* **72**, 3706–3709 (1994).
- ¹¹⁴T. W. Ebbesen, J. S. Tsai, K. Tanigaki, H. Hiura, Y. Shimakawa, Y. Kubo, I. Hirose, and J. Mizuki, “Dopant isotope effect on superconductivity in Rb_3C_{60} ”, *Physica C: Superconductivity* **203**, 163–166 (1992).
- ¹¹⁵M. Lannoo, G. A. Baraff, M. Schlüter, and D. Tomanek, “Jahn-teller effect for the negatively charged C_{60} molecule: analogy with the silicon vacancy”, *Physical Review B* **44**, 12106–12108 (1991).
- ¹¹⁶P. Zhou, K.-A. Wang, A. M. Rao, P. C. Eklund, G. Dresselhaus, and M. S. Dresselhaus, “Raman-scattering studies of homogeneous K_3C_{60} films”, *Physical Review B* **45**, 10838–10840 (1992).
- ¹¹⁷J. Winter and H. Kuzmany, “Landau damping and lifting of vibrational degeneracy in metallic potassium fulleride”, *Physical Review B* **53**, 655–661 (1996).
- ¹¹⁸M. Capone, M. Fabrizio, C. Castellani, and E. Tosatti, “Strongly Correlated Superconductivity”, *Science* **296**, 2364–2366 (2002).
- ¹¹⁹Y. Nomura, S. Sakai, M. Capone, and R. Arita, “Unified understanding of superconductivity and Mott transition in alkali-doped fullerenes from first principles”, *Science Advances* **1**, e1500568 (2015).
- ¹²⁰Y. Nomura, S. Sakai, M. Capone, and R. Arita, “Exotic s-wave superconductivity in alkali-doped fullerenes”, *Journal of Physics: Condensed Matter* **28**, 153001 (2016).

- ¹²¹L. Degiorgi, E. J. Nicol, O. Klein, G. Grüner, P. Wachter, S.-M. Huang, J. Wiley, and R. B. Kaner, “Optical properties of the alkali-metal-doped superconducting fullerenes: K_3C_{60} and Rb_3C_{60} ”, *Physical Review B* **49**, 7012–7025 (1994).
- ¹²²G. Jotzu, G. Meier, A. Cantaluppi, A. Cavalleri, D. Pontiroli, M. Riccò, A. Arda-
van, and M.-S. Nam, “Superconducting fluctuations observed far above T_c in the
isotropic superconductor K_3C_{60} ”, *Physical Review X* **13**, 021008 (2023).
- ¹²³M. Budden, T. Gebert, and A. Cavalleri, “Hybrid CO_2 -Ti:sapphire laser with tun-
able pulse duration for mid-infrared-pump terahertz-probe spectroscopy”, *Optics*
Express **29**, 3575–3583 (2021).
- ¹²⁴A. Nava, C. Giannetti, A. Georges, E. Tosatti, and M. Fabrizio, “Cooling quasi-
particles in A_3C_{60} fullerides by excitonic mid-infrared absorption”, *Nature Physics*
14, 154–159 (2018).
- ¹²⁵M. Kim, Y. Nomura, M. Ferrero, P. Seth, O. Parcollet, and A. Georges, “Enhancing
superconductivity in A_3C_{60} fullerides”, *Physical Review B* **94**, 155152 (2016).
- ¹²⁶M. A. Sentef, A. F. Kemper, A. Georges, and C. Kollath, “Theory of light-
enhanced phonon-mediated superconductivity”, *Physical Review B* **93**, 144506
(2016).
- ¹²⁷M. A. Sentef, “Light-enhanced electron-phonon coupling from nonlinear electron-
phonon coupling”, *Physical Review B* **95**, 205111 (2017).
- ¹²⁸Z. Dai and P. A. Lee, “Superconductinglike response in a driven gapped bosonic
system”, *Physical Review B* **104**, 054512 (2021).
- ¹²⁹A. Komnik and M. Thorwart, “BCS theory of driven superconductivity”, *The*
European Physical Journal B **89**, 244 (2016).

- ¹³⁰M. Knap, M. Babadi, G. Refael, I. Martin, and E. Demler, “Dynamical Cooper pairing in nonequilibrium electron-phonon systems”, *Physical Review B* **94**, 214504 (2016).
- ¹³¹J. R. Coulthard, S. R. Clark, S. Al-Assam, A. Cavalleri, and D. Jaksch, “Enhancement of superexchange pairing in the periodically driven Hubbard model”, *Physical Review B* **96**, 085104 (2017).
- ¹³²E. Rowe, B. Yuan, M. Buzzi, G. Jotzu, Y. Zhu, M. Fechner, M. Först, B. Liu, D. Pontiroli, M. Riccò, and A. Cavalleri, “Resonant enhancement of photo-induced superconductivity in K_3C_{60} ”, *Nature Physics* **19**, 1821–1826 (2023).
- ¹³³A. Sell, A. Leitenstorfer, and R. Huber, “Phase-locked generation and field-resolved detection of widely tunable terahertz pulses with amplitudes exceeding 100 MV/cm”, *Optics Letters* **33**, 2767–2769 (2008).
- ¹³⁴A. Cartella, T. F. Nova, A. Oriana, G. Cerullo, M. Först, C. Manzoni, and A. Cavalleri, “Narrowband carrier-envelope phase stable mid-infrared pulses at wavelengths beyond 10 μm by chirped-pulse difference frequency generation”, *Optics Letters* **42**, 663–666 (2017).
- ¹³⁵M. Jazbinsek, U. Puc, A. Abina, and A. Zidansek, “Organic crystals for THz photonics”, *Applied Sciences* **9**, 882 (2019).
- ¹³⁶N. B. Singh, D. R. Suhre, V. Balakrishna, M. Marable, R. Meyer, N. Fernelius, F. K. Hopkins, and D. Zelmon, “Far-infrared conversion materials: Gallium selenide for far-infrared conversion applications”, *Progress in Crystal Growth and Characterization of Materials* **37**, 47–102 (1998).
- ¹³⁷M. Dressel and G. Grüner, *Electrodynamics of Solids* (Cambridge University Press, 2002).

- ¹³⁸J. S. Dodge, L. Lopez, and D. G. Sahota, “Optical saturation produces spurious evidence for photoinduced superconductivity in K_3C_{60} ”, *Physical Review Letters* **130**, 146002 (2023).
- ¹³⁹A. Togo and I. Tanaka, “First principles phonon calculations in materials science”, *Scripta Materialia* **108**, 1–5 (2015).
- ¹⁴⁰S. Chattopadhyay, C. J. Eckhardt, D. M. Kennes, M. A. Sentef, D. Shin, A. Rubio, A. Cavalleri, E. A. Demler, and M. H. Michael, “Mechanisms for long-lived, photo-induced superconductivity”, *arXiv.2303.15355* (2023).